國立臺灣大學電機資訊學院光電工程學研究所

博士論文

Graduate Institute of Photonics and Optoelectronics
College of Electrical Engineering and Computer Science
National Taiwan University

Doctoral Dissertation

利用親水性質發展之自組式微透鏡與以離子導電高分子金屬複合物製備之低致動電壓可形變面鏡

Self-assembly microlens by hydrophilic effect and low actuation-voltage deformable mirror by ionic polymer metallic composite

魏祥鈞

Hsiang-Chun Wei

指導教授：蘇國棟 博士

Advisor: Guo-Dung John Su, Ph.D.

中華民國 100 年 12 月

Dec, 2011

誌謝

在博士班的生涯中，我要感謝許多人給予我的協助，不管是研究、課業、生活或是精神上的指導或支持，都仰賴於你們的幫忙，我才有辦法完成這篇論文。因此，我很感謝這段時間曾經給我幫助的人以及不斷鼓勵我的人。

首先要感謝這幾年來不斷用心給予指導及鼓勵的指導教授蘇國棟博士，當實驗遇到瓶頸時教授提供的許多建議、支持我在實驗上的各種嘗試，讓我學習到對研究的應有的態度與方法。感謝教授在學生投稿時不厭其煩地幫我修改內容，讓文章可以順利地刊載在期刊上。除此之外，也很感謝教授在生活上給予的關心，學生特別感到貼心。還有諸位口試委員們，林晃巖博士、趙基揚博士、馮國華博士、許巍耀博士，你們提供的寶貴意見，讓我受益良多。此外，我也要感謝元亨、竟偉、孟萱在光學系統設計上，還有美妏在微透鏡陣列及波前感測器的努力。研究團隊中的煜達、晉亨、鄭維、豐德(Te)、適安，感謝你們耐心地和我一起做實驗，一次又一次的討論之中，我也有許多寶貴的收穫，同時也感謝你們幫忙把相關的技術傳承下去。另外也感謝台大機械所學弟丞家對於化學電鍍的指導。

感謝已畢業的怡文、哲瑜、美妏、以樵，在無數個熬夜生活中，你們的相伴讓我不是一人孤軍奮戰。也要感謝實驗室的成員，包含學長紹軒、欣達，以及現在一起在實驗室的璿閔、聖原、旌寶、建綸、鄭維、晉亨、豐德(Te)、裕閎、佳勳、柏宇、沐豪、柏彰、宇翔 、威志、適安、建任、以晨、惠凱、舜齡、怡瑄、緯詳、偉廷。還有許多已經畢業的成員及其他實驗室的朋友們、光電所所辦小姐和所學會的夥伴，雖然無法列舉，你的幫助我會銘記在心，也因為有你，讓我在學校的生活增添了許多風味。

本論文獻給我最要感謝的最親愛的父母還有姐姐，多年來給我經濟還有精神上的支持，在我求學的過程中不斷的鼓勵我、安慰我，無論我多沮喪都陪伴在我身邊。還有女友孟潔多年的相伴、包容、關懷。若將來我能有所成就，將會是你們的功勞。

魏祥鈞 2011 年 12 月

中文摘要

在本篇論文中，我們的研究涵蓋了兩大主題，分別為微透鏡陣列(microlens array)以及可形變面鏡(deformable mirror)。經由整合此二元件與一般光學元件後，發展光學系統於不同的應用。

自組式微透鏡陣列(self-assemble microlens array)，利用了紫外線臭氧清潔機將 SU-8 負型光阻表面改質，產生週期性排列的親水性區域，再利用表面張力將稀釋過後的 SU-8 光阻自行聚集在此親水性區域之中，進而形成球面的液態平凸透鏡，最後經由紫外光的固化後成了固體的微透鏡陣列。SU-8 光阻具有良好的化學穩定性及機械強度，其光學吸收率非常低，加上基板使用的是透明玻璃，所以製作出來的微透鏡陣列是穿透式的，不須要再另外經過翻模的方式來製作，大幅簡化了製作的流程及減少製程時間。此方法具有低成本、低溫、省時之特點。另外，SU-8 光阻本身是極性材料，藉由外加的電場可以增加表面的曲率，藉此進一步可以產生更短焦距的微透鏡，同時也使表面的粗糙度降低，提高其光學性質。同時，使用這種方法，我們可以精準地將微透鏡製作在發光二極體(LED)上，提高提取效率並增加發散角。另外，藉由實驗室發展的雙層熱回流式長焦長微透鏡陣列，我們發展了更為靈敏、動態範圍更廣的薛克-哈特曼波前感測器(Shack-Hartmann wavefront sensor)，同時針對長焦距及短焦距的影響與商用的感測器做比較。

我們利用了實驗室發展的微機電有機可形變面鏡 (micro electro mechanical systems organic deformable mirror)，配合光學鏡頭元件設計了可變對焦平面的光學模組，搭配 Tenengrad 影像處理方法及百分率降幅方法(percentage drop method)組成的自動對焦演算方法，成功地完成自動對焦光學模組。由於微機電有機可形變

面鏡的驅動電壓較高(約 150 伏特)，所以我們進而採用了高分子致動器-離子導電高分子金屬複合物(ionic-conductive polymer metal composite, IPMC)，其具有低致動電壓與大位移量的特性。我們藉由發展此材料的灰盒子理論，搭配 ANSYS 有限元素分析軟體，設計了齒輪狀的離子導電高分子金屬複合物可形變面鏡(gear shaped IPMC DM)，其特點為低致動電壓及較廣的焦距變化。同時由於其可雙向致動的特性，可製作出同時具有聚焦及散焦能力的可形變面鏡。

最後，我們希望此篇論文可以啟發相關的研究，並對後續的發展有些許貢獻。

關鍵字: 微透鏡、SU-8 光阻、親水性、波前感測器、可形變面鏡、離子導電高分子金屬複合物。

ABSTRACT

In this dissertation, there are two major topics of microlens array (MLA) and deformable mirror (DM). By integrating these two components and ordinary optical component, we developed different optics system in different applications.

Self-assembled microlens array was fabricated by hydrophilic effect using Ultraviolet (UV)/ozone modification on glass substrate. The modification on SU-8 photoresist produced periodic array of hydrophilic areas on the surface by the use of shadow mask. Afterwards, the substrate was dipped in and out of diluted SU-8 photoresist. Therefore, the liquid self-assembled MLA was formed. Finally, the solid MLA was cured by UV light. SU-8 photoresist has good chemical and mechanical strength, so it is suitable for MLA. Besides, the fabricated MLA is transparent so that there has no need for etch transferring. It decreases the process complexity a lot. Meanwhile, because of the polar molecular of SU-8 photoresist, the curvature of the microlens can be enlarged by applying external electric field. The surface roughness could be improved as well. This method provides a low cost, low time consumption, no etch transfer, low temperature, and no photo lithography method to fabricate MLA. We applied this method to fabricated microlens on a light emitting diode (LED) chip with precisely alignment. That improved the extraction efficiency and increased the viewing angle. Besides, we developed a more sensitive and larger dynamic ranged Shack-Hartmann wavefront sensor by using the developed long focal length MLA using double layer thermal reflow method. We also compared it with the commercial product.

We developed a thin autofocus camera module by using the developed micro electro mechanical systems (MEMS) organic deformable mirror (DM). It included a focus-varying optical system, and autofocus algorithm using Tenengrad image

sharpness function and percentage-drop method. Besides, because of the high actuation voltage (~150 V), we adopt an ionic-conductive polymer composite to fabricate DM. IPMC is a polymer actuator with the advantage of low actuation voltage and large displacement. We built a simplified grey box model and simulate the deformation shape by using finite element method software, ANSYS® . A gear shaped IPMC DM was designed and demonstrated. It had the advantage of low actuation voltage and large optical power. Meanwhile, because of the bi-directional deformation ability, the DM with both positive and negative optical power was achieved.

Finally, we believe these research topics could inspire the related researchers and might have some benefit to the human.

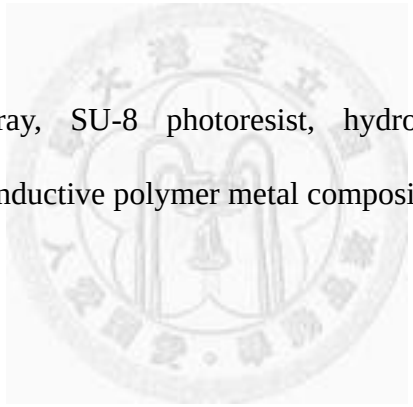

Keywords: microlens array, SU-8 photoresist, hydrophilic, wavefront sensor, deformable mirror, ionic-conductive polymer metal composite.

CONTENTS

論文口試委員審定書

誌謝 I

中文摘要 II

ABSTRACT IV

CONTENTS VI

LIST OF FIGURES X

LIST OF TABLES XVIII

Chapter 1 Dissertation Organization & Introduction 1

1.1 Dissertation organization 1

1.2 General introduction 2

1.2.1 Review of microlens array fabrication technologies 2

1.2.2 Review of Shack-Hartmann wavefront sensor 6

1.2.3 Review of method to achieve auto-focus function 9

References 13

PART I MICROLENS ARRAY 14

Chapter 2 Using Hydrophilic Effect to Fabricate Self-Assembled Microlens Array by UV/ozone Modification 15

2.1 Introduction 16

2.2 Fabrication Process 17

2.3 Experimental Results and Discussions 19

2.4 Conclusions 27

References 28

Chapter 3 Fabrication of Transparent and Self-Assembled Microlens Array Using

Hydrophilic Effect and Electric Fielding Pulling 30

3.1 Introduction 31

3.2 The working mechanism 32

3.3 Fabrication processes 35

3.3.1 SU-8 photoresist base layer 36

3.3.2 UV/ozone treatment 37

3.3.3 Dipping in and out of diluted SU-8 photoresist 37

3.3.4 Applying electric field and UV curing 38

3.4 Experimental results and discussions 39

3.5 Conclusions 48

References 49

Chapter 4 Self-assembled microlens on top of light emitting diodes using hydrophilic effect for improving extraction efficiency and increasing viewing angle 51

4.1 Introduction 52

4.2 The working mechanism 53

4.3 Fabrication process 56

4.4 LED encapsulation 56

4.4.1 SU-8 photoresist base layer 57

4.4.2 UV/ozone treatment 57

4.4.3 Dipping in and out of diluted SU-8 photoresist & UV curing 58

4.5 Optical System Simulation and experimental results 59

4.6 Conclusions 68

References 69

Chapter 5 An Optical Wavefront Sensor Based on a Double Layer Microlens Array 71

5.1 Introduction 72

5.2 Design of Double Layer Microlens Array 73

5.3 Fabrication Processes and Results 75

5.4 Wavefront Sensor Computing Algorithm and Measurement Results79

5.5 Conclusions.....88

References 90

PART II DEFORMABLE MIRROR.....91

Chapter 6 Controlling a MEMS Deformable Mirror in a Miniature Auto-Focusing Imaging System.....92

6.1 Introduction.....93

6.2 Deformable Mirror and Optical System Design 94

6.3 Tenengrad Method and Percentage-Drop Searching Algorithm.....101

6.4 Experiment Results and Discussion 105

6.5 SUMMARY 109

References 111

Chapter 7 Thin autofocus camera module by a large-stroke micromachined deformable mirror.....113

7.1 Introduction.....114

7.2 Optical System Design with Autofocus Function 115

7.3 Device Fabrication and Experimental Results.....118

7.4 Conclusion 127

References 128

Chapter 8 A Low Voltage Deformable Mirror using Ionic-conductive Polymer Metal Composite 129

8.1 Introduction.....130

8.2 Principle of IPMC.....132

8.3 FEM simulation model of cantilever beam.....133

8.4 Simulation model and experimental verification.....137

8.5 Gear shaped IPMC and experimental result.....139

8.6 SUMMARY 144

References 146

Chapter 9 Conclusions and Future Work.....147

9.1 Dissertation conclusions 147

9.1.1 Microlens arrays 147

9.1.2 Deformable mirrors 148

9.2 Suggestions for future work 149

9.2.1 The focus microlens on LED by using thicker PDMS. 149

9.2.2 The microlens application on concentrated solar cell.....150

9.2.3 The improvement of surface roughness for IPMC DM by the use of PDMS buffered layer.....151

Publication List.....153

LIST OF FIGURES

Figure 1-1 The microlens fabrication techniques and their development timeline [1].....4

Figure 1-2 The different fabrication process steps for refractive reflow photoresist microlenses: (a) patterning of the photoresist layer; (b) development of the exposed regions; (c) melting of the cylindrical islands. [1].....5

Figure 1-3 Basic fabrication process for arrays of spherical microlenses with deep lithography with protons: irradiating the PMMA layer through a mask and applying a vapour on one surface of the irradiated sample are the basic processing steps for the fabrication of 2D arrays of stable and uniform spherical microlenses. [1] 5

Figure 1-4 Principle of laser ablation. [1].....6

Figure 1-5 Schematic of the droplet-on-demand microjet system 6

Figure 1-6 (a) Scheiner's disk produces double retinal images of a single object if the eye is ametropic. (b) Scheiner's disk was used by Smirnov to create a subjective aberrometer. [8] 7

Figure 1-7 A Scheiner's disk with multiple holes is called a Hartmann screen and may be used to construct an objective aberrometer. [8] 8

Figure 1-8 An aberrated wavefront is incident on a lenslet array. Each spot is shifted from its on-axis position, shown in blue, by an amount proportional to the average phase gradient across its lenslet [10].....8

Figure 1-9 The schematic drawing of auto-focus system with a moving component.....9

Figure 1-10 The scheme of auto-focus system without moving component.....10

Figure 1-11 Lens like phase retardation when applying voltage on LC cell. [14] (a) No voltage apply. (b) result a positive optical power lens like phase retardation.

(c) result a negative optical power lens like phase retardation. 11
Figure 1-12 Structure of liquid lens developed by Varioptic. [17] 12
Figure 1-13 The disadvantage of liquid lens is that coma aberration may occur due to gravitational pull. [16] 12
Figure 2-1 The fabrication process of SU-8 photoresist MLA using hydrophilic effect under UV/ozone treatment. 18
Figure 2-2 The experimental results of contact angles between a non-UV-exposed diluted SU-8 photoresist droplet (~10 μL) and an SU-8 photoresist base layer. 21
Figure 2-3 Atomic force microscope (AFM) (OBJ-204C, ITRI, Taiwan) images of the SU-8 base layer (a) before and (b) after four minutes UV/ozone treatment. All images were taken at a scan size of 1x1 μm^2 with 128 x 128 $pixel^2$. 21
Figure 2-4 The contact angles for different UV/ozone treatment time and different shadow mask openings. The shadow mask openings were 50 μm, 100 μm, and 200 μm in diameters. 22
Figure 2-5 Focal length versus UV/ozone treatment time. 22
Figure 2-6 The MLAs fabricated using 100-μm diameter shadow mask. (a) Optical microscopy and (b) the corresponding focus points with (c) intensity profile for four minutes UV/ozone treatment time. (d) Zoomed image of the optical intensity profile. 24
Figure 2-7 The SEM of (a) microlenses of 100 μm diameter under one minute UV/ozone treatment time. (b) the cross section profile of one minute treated microlens. 25
Figure 2-8 The interferogram of the wavefront surface measurement. (a) 50 μm (b) 100 μm (c) 200 μm. 25

Figure 3-1 The schematic of the presented fabrication of the SU-8 MLA.(a) UV/ozone treatment (b) Hydrophilic zones is presented (c) Dip out from the diluted SU-8 photoresist solution (d) Apply the external voltage. 35

Figure 3-2 The fabrication process. (a) An SU-8 base layer on the ITO glass (b) Contact shadow mask (c) UV/ozone treatment (d) remove shadow mask (e) Hydrophilic zones presented (f) Dip out from diluted SU-8 photoresist solution (g) Apply the external voltage. 39

Figure 3-3 SEM images of 4 minutes UV/ozone treated MLA of 100 μm diameter (a) without and (b) with external electric field of 3.4 V/μm. (c) The cross section profile of an SU-8 microlens. 41

Figure 3-4Surface profile of microlens via different electric fields. 41

Figure 3-5 Lens profile and the corresponding best fit sphere of the fabricated microlens (a) without applied electric field, (b) with 1.7 V/μm, and (c) 3.4 V/μm measured by probe-type surface analyzer. The circles show measure points and solid red lines are best fit spheres. 42

Figure 3-6 The experimental results of UV/ozone treatment time versus contact angle. The black solid squares are the experimental results of contact angles between a non-UV-exposed diluted SU-8 photoresist droplet and an SU-8 photoresist base layer. 44

Figure 3-7 MLAs of 100 μm diameter with 4 minutes UV/ozone treatment time via electric fields of (a) 0 V/μm, (b) 1.7 V/μm, and (c) 3.4 V/μm and the corresponding focus beam spots. 47

Figure 4-1 The schematic of the presented fabrication of the SU-8 MLA. (a) Encapsulating the LED chips by PDMS. (b) UV/ozone treatment through the shadow mask. (c) Removing the shadow mask. (d) Dipping out from the

diluted SU-8 solution. (e) UV curing. 55

Figure 4-2 The fabrication process. (a) The bared LED chip. (b) Wire bonding and PDMS encapsulation. (c) PDMS hardening. (d) A layer of SU-8 base layer. (e) UV/ozone treatment through shadow mask. (f) Removing the shadow mask. (g) Dipping out from diluted SU-8 solution. (h) UV curing. 59

Figure 4-3 The optical system of microlens on LED. 60

Figure 4-4 The simulation result of luminance map (30 mm x 30 mm). (a) Without microlens (b) With microlens. 61

Figure 4-5 (a) The experimental results of contact angles between a non-UV-exposed diluted SU-8 photoresist droplet and an SU-8 photoresist base layer. (b) The experiment setup of Sessile Drop method. 62

Figure 4-6 (a) The SEM photograph of 200-μm diameter MLA under three minutes UV/ozone treatment time. (b) The cross section profile of an SU-8 microlens. 63

Figure 4-7 The optical microscope image of fabrication result. (a) The LED chip with aluminum (Al) wire bonding. (b) The 200-μm diameter microlens on LED. (c) The clear stereo microscope image on both LED chip and microlens. (d) The tile view of the stereo microscope image of the microlens on LED. 65

Figure 4-8 The measurement setup of the angular light field distribution. 66

Figure 4-9 The normalized angular distribution of light intensity (from -90 to 90 degree). It improved the extraction efficiency of 15 % and 28% in maximum and total accordingly, and increased the viewing angle of 17 degree ($\theta_{1/2}$). 67

Figure 4-10 The experimental illumination map. (a) Without microlens and (b) With microlens. 68

Figure 5-1 Light propagation in a microlens by (a) traditional thermal method (dashed

lines) and (b) our new method (solid lines). 74
Figure 5-3 Fabrication steps of long-focal length MLA. (a)PR cylinders (b)Thermal reflow (c)PDMS molding (d)Release PDMS mold (e)Drop UV-resin & attach glass(f)UV curing. 76
Figure 5-6 SEM image of the UV-resin MLA (a) without and (b) with the second layer of PDMS. 77
Figure 5-7 The focused spot images (above) and their intensity distribution (below) of **(a)** circular lens quadratic grid MLA, **(b)** circular lens hexagonal grid MLA, **(c)** hexagonal lens MLA, and **(d)** square lens MLA. 78
Figure 5-8 The experiment setup for measuring a wavefront aberration of testing lens (PAL) by using our fabricated MLA and SHWS. 82
Figure 5-9 (a) Focal spots image of the reference wavefront, (b) focal spots image of the aberrated wavefront, and (c) detection picture of image spots for reference beam and distorted beams. 83
Figure 5-10 Wavefront measurement results of (a) PAL and (b) PCX by our SHWS (above) and commercial SHWS (below). 84
Figure 5-11 Wavefront measurement results of defocus by using (a) long focal length (UV-resin) and (b) shorter focal length (SU-8) MLA as our SHWS lenslet component. 88
Figure 6-1 Structure of MEMS deformable mirror [(a) Top electrode plate; (b) Bottom electrode plate; (c) Encapsulation]. 96
Figure 6-2 Deformable Mirror [(a) Without an applied voltage; (b) With an applied voltage] 97
Figure 6-3 Relation between the optical power of the deformable mirror and the applied voltage difference. 98

Figure 6-4 Optical system layout of the reflective auto-focusing camera module.....99
Figure 6-5 Picture of the actual optical camera module.....99
Figure 6-6 Modulation transfer function (MTF) of the optical system.....101
Figure 6-7 Focus value vs. applied voltage at different object distances.....104
Figure 6-8 Percentage-drop searching algorithm.....105
Figure 6-9 Setup of the auto-focusing camera system.....107
Figure 6-10 Images taken at different object distances and with optimized applied voltages.....108
Figure 6-11 Experimental results of percentage-drop Searching. The standard deviations are 0.31 and 0.02 when the object distances were 200 mm and 50 mm respectively.....109
Figure 7-1 (a) Optical system design in reflective form, and (b) its modulation transfer function (MTF) when a MEMS deformable mirror is flat for far objects..116
Figure 7-2 (a) Image simulation results of Lady Lenna, and (b) its modulation transfer function (MTF) when a MEMS deformable mirror is actuated for near objects.....117
Figure 7-3 Device fabrication processes for a top polymer membrane and a bottom electrode.....120
Figure 7-4 Schematic drawings and photos of a fabricated MEMS deformable mirror device.....121
Figure 7-5 Diopter changes versus applied voltage of the polymer MEMS DM.....122
Figure 7-6 Assembly 3D drawings of an autofocus module.....124
Figure 7-7 (a) Cover with a freeform mirror, (b) base with polymer MEMS DM and (c)final Assembly module.....125
Figure 7-8 Pictures of near and far objects.....127

Figure 8-1 The schematics of the IPMC network and (b) the molecular formula of Nafion. 133
Figure 8-2 The simplified model with constant stress field which would be implied to the FEM model. 134
Figure 8-3 ANSYS® structure model of IPMC 135
Figure 8-4 ANSYS® element model of IPMC.....135
Figure 8-5 FEM simulation which varied the length (L) and width (w) of IPMC and the half thickness (h) of Nafion with constant surface force (P = 100 Pa).....137
Figure 8-6 Deformation shape of double side confinement. (a) simulation (b) experiment. (These figures show IPMC with and without applied voltage)138
Figure 8-7 The black dots are experimental results of tip displacement vs. applied voltage. And the solid line is simulation result by curve fitting, where C2 is 60000 (Pa*m/V). 139
Figure 8-8 The gear shaped IPMC design. 141
Figure 8-9 The IPMC process flow.(a) ion exchange polymer formation and pre-process; (b) initial compositing; (c) surface electrode growing;(d) shape cutting. ..141
Figure 8-10 (a) The Picture of experimental demonstration of the new deformable mirror. (b) The deformation simulated by ANSYS® 143
Figure 8-11 The intensity profile of the laser beam spot with non-actuated IPMC (non-focused) and actuated IPMC (focused).....143
Figure 8-12 The surface profile using white light interferometer. 144
Figure 9-1 The principle of the LED light beam manipulation by using PDMS thickness.150
Figure 9-2 The small lens array with triangular prism model 151
Figure 9-3 IPMC DM with PDMS buffered layer. 151
Figure 9-4 Fabrication principle of IPMC DM with PDMS buffered layer. (a) IPMC

sheet(b) clamped by frames (c) spin PDMS and coat copper reflector (d) laser cutting (e) the section of PDMS modified gear shaped IPMC DM. ..152

LIST OF TABLES

Table 2-1 The footprint diameters of MLAs.....23

Table 2-2 The summarized results of fabricated MLAs. 26

Table 3-1 The focal length, sag height, and radius of curvature of fabricated MLA by different UV/ozone treatment time without external electric field enhancement. 45

Table 3-2 The summarized results of the fabricated MLA.....48

Table 5-1 Lens arrangement versus fill factor for 20 m of lens gap.....78

Table 5-2 Methods for increasing the focal length of MLA.....79

Table 5-3 The comparison of wavefront measurement by our SHWS and commercial SHWS. 86

Table 8-1 Physical parameters of different materials 136

Table 8-2 The comparison of different technologies.....144

Chapter 1 Dissertation Organization & Introduction

1.1 Dissertation organization

The dissertation consists of two parts. From chapter 2 to chapter 5 are described to the microlens. From chapter 6 to chapter 8 are described to the deformable mirror. Chapter 9 is the conclusion and future works. Each chapter is a research topic. Meanwhile, some topics were published in journals.

In chapter 2, we presented a self-assembled microlens array (MLA) fabricated by use of the hydrophilic effect under ultra-violet (UV)/ozone treatment. This method provides a fast, simple, and low cost process. It does not require lithography or etch-transfer processes. *(This work was published in Photonics Technology Letters, IEEE, vol. PP, pp. 1-1, 2011).*

In chapter 3, we present a variable and self-assembled spherical microlens array (MLA) fabricated by the use of the hydrophilic effect under ultra-violet (UV)/ozone treatment. The optical power and surface roughness of MLA was further enhanced by applying external electric field. *(This work was accepted in Journal of Micromechanics and Microengineering at 2011. 11. 25).*

In chapter 4, we propose a self-assembled microlens arrays (MLAs) on top of light emitting diodes (LEDs) based on hydrophilic effect under ultraviolet (UV)/ozone treatment to improve extraction efficiency and to increase viewing angle. *(This work was submitted to Journal of Display Technology 2011.12.16).*

In chapter 5, we present the design and fabrication of long focal length MLA based on a double layer structure for optical wavefront sensing applications. A longer focal length MLA could provide high sensitivity and spatial resolution of a wavefront sensor. *(This work was published in Sensors, vol. 11, pp. 10293-10307, 2011).*

In chapter 6, we discussed a new auto-focusing camera system, which features a reflective optics design based on a polymer MEMS deformable mirror and a control program. *(This work was published in IEEE Transactions on Control Systems Technology, vol. PP, pp. 1-5, 2011).*

In chapter 7, we propose a second generation of thin autofocus system using a large stroke MEMS (micro-electro-mechanical systems) deformable mirror which has the potential to downscale the size and to minimize chromatic aberration. *(This work was published in Optics Express, vol. 18, pp. 11097-11104, 2010).*

In chapter 8, we design the gear shaped IPMC type deformable mirror that is simulated by finite element method and then demonstrate its focus-varying function. It requires less than 5 volts to achieve 20 diopters.

In chapter 9, we draw conclusions of previous chapters and show the suggestions to the future work.

1.2 General introduction

1.2.1 Review of microlens array fabrication technologies

Over the last 20 years several research groups and industrial research laboratories have therefore been focusing their attention on the development of fabrication techniques for refractive microlenses and microlens arrays [1]. In the 17th century, Robert Hooke and Antonie van Leeuwenhoek both developed techniques to make small glass lenses for use with their microscopes. Hooke melted small filaments of Venetian glass and allowed the surface tension in the molten glass to form the smooth spherical surfaces required for lenses, then mounting and grinding the lenses using conventional methods. The principle has been repeated by performing photolithography

into materials such as photoresist or UV curable epoxy and melting the polymer to form arrays of multiple lenses [2][3].

A wide variety of applications of very small lenses grows interest in the study of arrays. In 1908, Gabriel Lippmann proposed numerous applications for small lens arrays including the recording of three dimensional pictures by taking photographs through biconvex arrays. A variety of manufacturing techniques have been proposed and studied. However, one of the simplest and most elegant techniques was described by Popovic *et al* (1988). He fabricated cylindrical islands of photoresist using by photolithography and then melted them so that surface tension caused PR to adopt hemispherical form.

Fabrication of MLAs prototype is very important as it defines all characteristics of MLAs. It has been long known that fabrication methods of MLAs can be achieved by thermal reflow [2], laser beam written microlenses [4], DLP (deep lithography with protons) [5], laser ablation [6], microjet printing [7], and reactive ion etching which are shown in Figure 1-1.

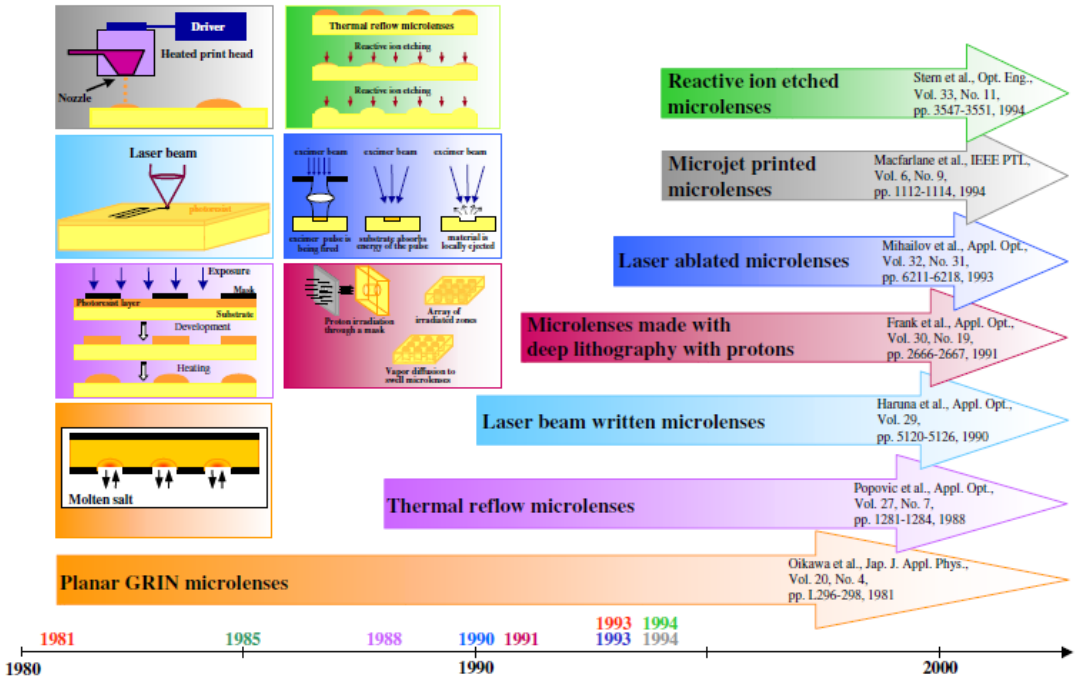

Figure 1-1 The microlens fabrication techniques and their development timeline [1].

Figure 1-2 to Figure 1-5 shows the process flow of the microlens fabrication techniques [1]. Some methods are relatively inexpensive and are based on existing technologies while others require dedicated processing tools and/or new materials with special properties. Most of these microlens fabrication methods yield MLAs that satisfy many of the optical quality requirements. They differ however in that some fabrication methods are more suitable either for rapid prototyping, for mass fabrication or for monolithic integration than others.

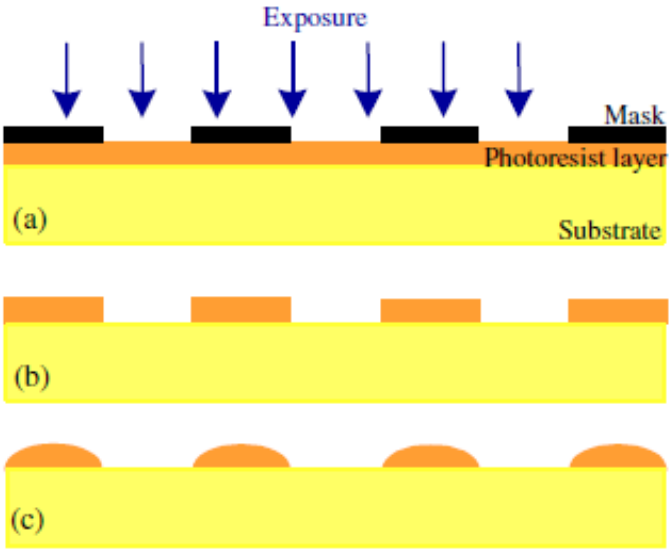

Figure 1-2 The different fabrication process steps for refractive reflow photoresist microlenses: (a) patterning of the photoresist layer; (b) development of the exposed regions; (c) melting of the cylindrical islands. [1]

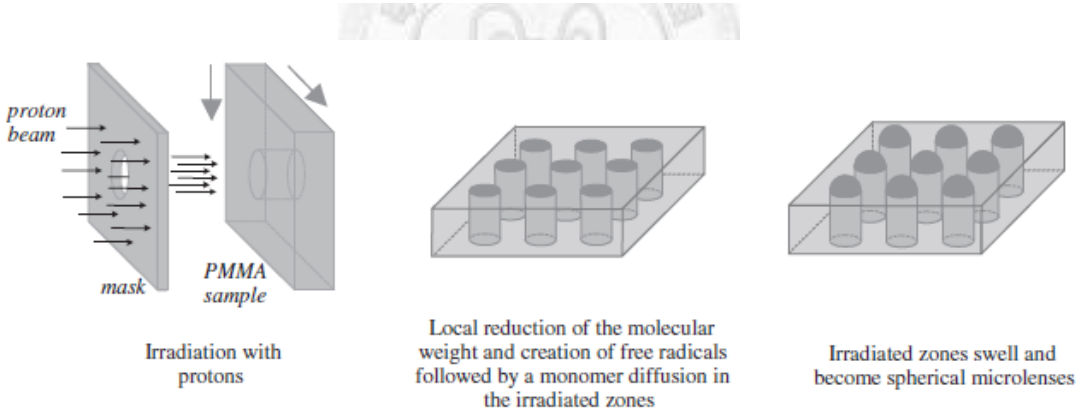

Figure 1-3 Basic fabrication process for arrays of spherical microlenses with deep lithography with protons: irradiating the PMMA layer through a mask and applying a vapour on one surface of the irradiated sample are the basic processing steps for the fabrication of 2D arrays of stable and uniform spherical microlenses. [1]

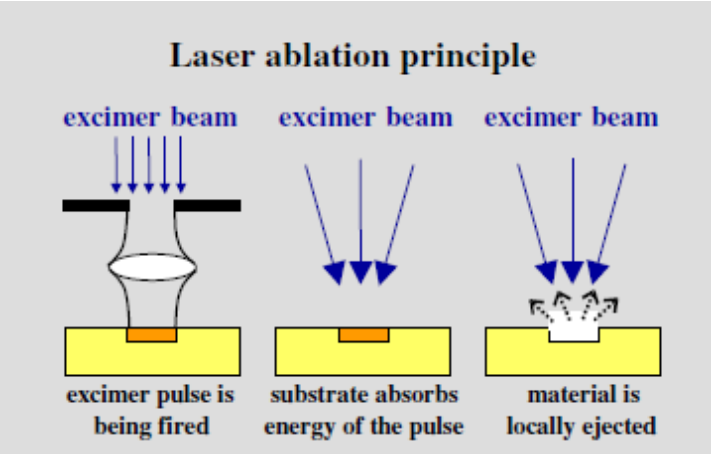

Figure 1-4 Principle of laser ablation. [1]

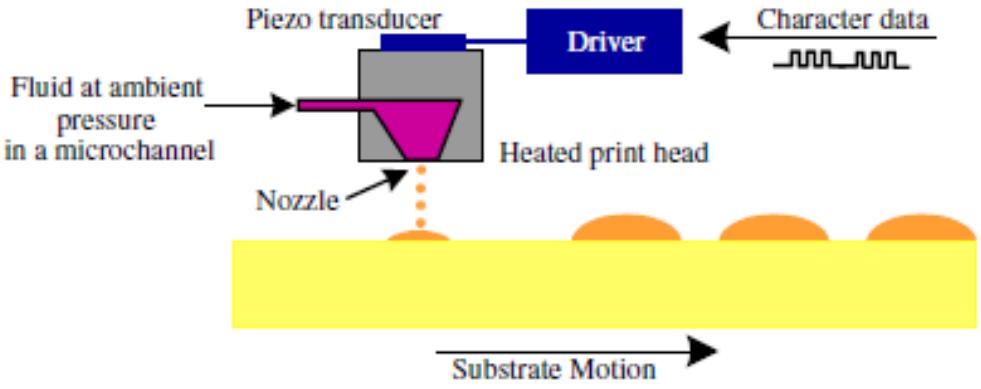

Figure 1-5 Schematic of the droplet-on-demand microjet system used to fabricate refractive microlenses. [1]

1.2.2 Review of Shack-Hartmann wavefront sensor

Nearly 400 years ago, Christopher Scheiner, a professor at the University of Ingolstadt, used a simple device known as the Scheiner Disk to demonstrate the focusing ability of the human eye [8]. Scheiner's experiments applied a single point of light through an opaque disk perforated with two pinholes and showed that two retinal images will be formed by imperfect eyes as showed in Figure 1-6(a) [8]. An achievement by using a fixed light source for the central, reference pinhole and a

moveable light source for the outer pinhole as illustrated in Figure 1-6(b) [8] and adjusting the moveable source horizontally and vertically until the light intersects at the retina and the patient reports seeing a single point of light. The ray aberration of the eye at the given pupil point is measured from the displacement distances having made by this adjustment. This subjective aberrometer was first introduced by Smirnov and has been used in visual optics research the past 50 years.

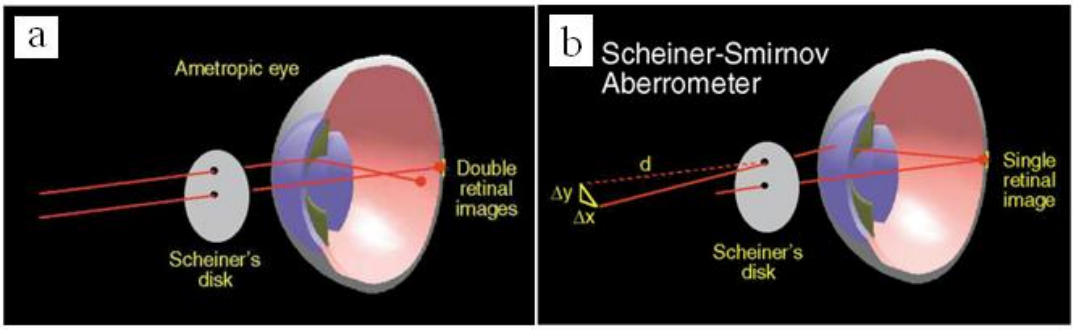

Figure 1-6 (a) Scheiner's disk produces double retinal images of a single object if the eye is ametropic. (b) Scheiner's disk was used by Smirnov to create a subjective aberrometer. [8]

Johannes Hartmann, a professor in Potsdam, at the beginning of the 20th century developed his famous Hartmann screen. Additional holes are constructed in Scheiner's disk to convert the Scheiner-Smirnov subjective technique into an objective aberrometer. On the contrary, the direction of the light propagation is reversed by placing a spot of light on the retina. This spot then becomes a point source which radiates back out of the eye as illustrated in Figure 1-7. Each aperture in the Hartmann screen isolates rays emerging from the eye through the different part of the pupil. These emerging rays intersect a sensor to detect the horizontal and vertical displacement of each ray from the corresponding, non-aberrated, reference position.

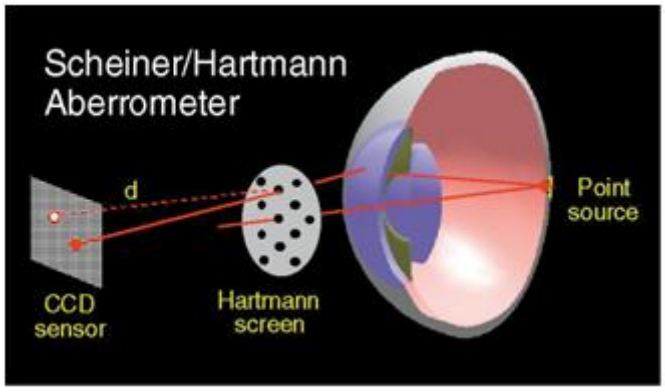

Figure 1-7 A Scheiner's disk with multiple holes is called a Hartmann screen and may be used to construct an objective aberrometer. [8]

Eighty years later, Dr. Roland Shack replaced the holes in Hartmann screen by lenses. By adding lenses, the light passing through the apertures will be broken into many individual beams and concentrated to focal spots which are shown in Figure 1-8, and detected by the image sensor. The derivative of the wavefront optical path difference (OPD) map produces wavefront slopes, the integration of wavefront slopes produces wavefront OPD maps [9].

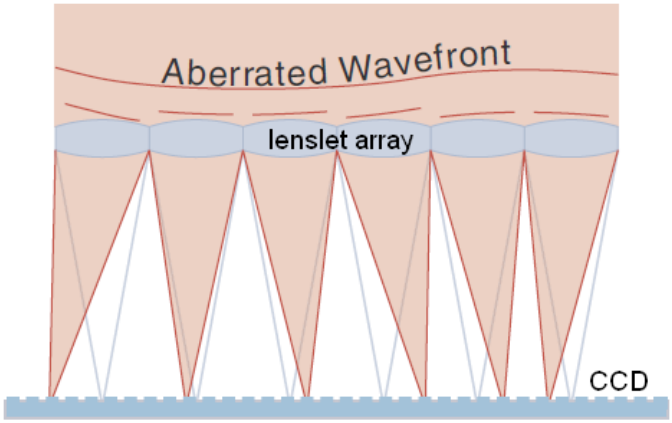

Figure 1-8 An aberrated wavefront is incident on a lenslet array. Each spot is shifted from its on-axis position, shown in blue, by an amount proportional to the average phase gradient across its lenslet [10].

1.2.3 Review of method to achieve auto-focus function

There are several ways to vary effective focus length of image system to achieve auto-focus function. They can roughly be classified to two groups, system with moving components and system without moving components. These techniques will be introduced in this section

System with moving components is characteristic with that it has moving components to move lens or lens group back and forth to vary effective focal length. Therefore, the system can focus on object located at difference distance from lenses module, as shown in Figure 1-9.

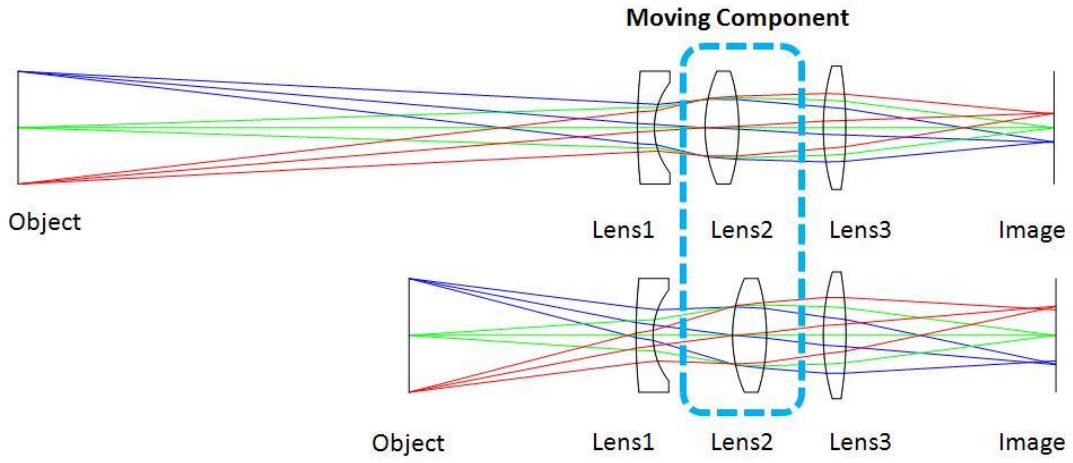

Figure 1-9 The schematic drawing of auto-focus system with a moving component.

The principle can be illustrated by this equation [11]:

$$\frac{1}{f} = \frac{1}{f_1} + \frac{1}{f_2} - \frac{d}{f_1 \times f_2} \tag{1.1}$$

which states the effective focal length, f, of a system combined with two lenses at a distance of d and whose focal length are f_1 and f_2 individually. According to equation (1.1), it is obvious to know that vary the distance between lenses can vary effective focal length.

Motor has been used for camera with auto-focus or zoom function for a long time, but with the trend to downscale of camera built-in portable device, especially the thin thickness, miniaturizing camera module becomes important. Therefore, small motor design has appeared, for instance, miniature stepping motor, piezoelectric motor, and voice and coil motor.

To downscale purpose, more and more techniques are proposed to achieve auto-focus function without any moving components. The advantage of system without moving components is that the total track length has the potential to become shorter than system with moving components since there need no space for moving component to move forth and back. The system design will become more flexible and it is easier to save space for designer. The concept of system without moving components is that tuning optical power of one or more optical elements to change system's effective focal length. Figure 1-10 is a simple schematic of system to achieve auto-focus function without moving components. Lens 1 and Lens 3 are the fixed optical power element, and Lens 2 is tunable optical power element. Tuning optical power of Lens 2 can change effective focal length of system.

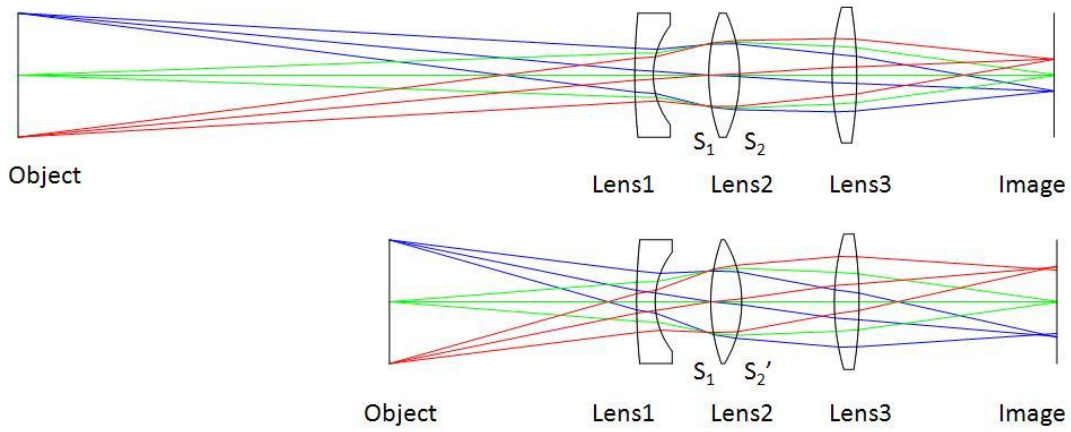

Figure 1-10 The scheme of auto-focus system without moving component.

Liquid crystals (LCs) have applications for light spatial modulators, waveguides, phase modulators, liquid crystal switches, light detectors, and displays. In recent years, it has been reported that LCs has the capability of auto focus function for lenses application. Akita University has developed a technique which is a liquid crystal lens with focal length variable from negative to positive [12-14]. The lens like phase retardation profile from positive to negative lens can be obtained by varying the two voltages appropriately, as show as Figure 1-11. Therefore, the LC cell acts as a lens whose focal length can be control by the voltages.

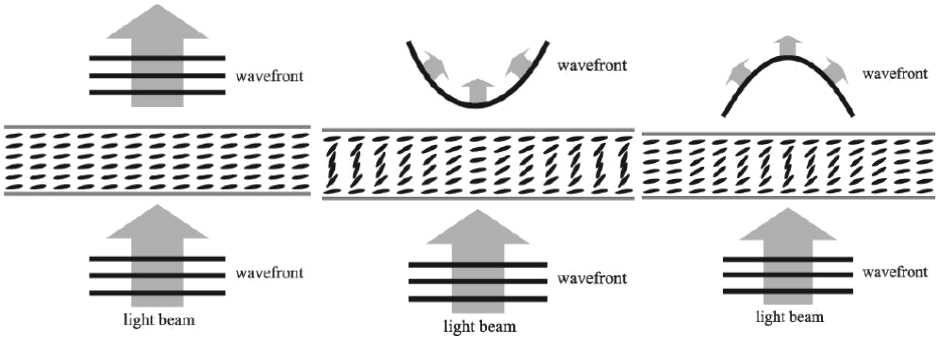

(a) (b) (c)

Figure 1-11 Lens like phase retardation when applying voltage on LC cell. [14] (a) No voltage apply. (b) result a positive optical power lens like phase retardation. (c) result a negative optical power lens like phase retardation.

Another element has used to achieve auto-focus function without moving component is liquid lens. Liquid lenses developed by Varioptic [15-17]. The mechanism is based on the phenomenon of electro-wetting. Figure 1-12 is the schematic of the design of Varioptic. Two immiscible liquids, water and oil, one is used as conducting layer and the other is used as insulating layer, are contained in the two transparent substrates. The contact angle between water and substrate vary with the applied voltage and the shape of interface used as the lens. The interface between water and

oil, is determined by the balance of the surface tension produced by the two liquids. On the other words, the focal length of the liquid lens is controlled by varying applied voltage. However, its disadvantage is that coma aberration may occur due to gravitational pull, as shown in Figure 1-13

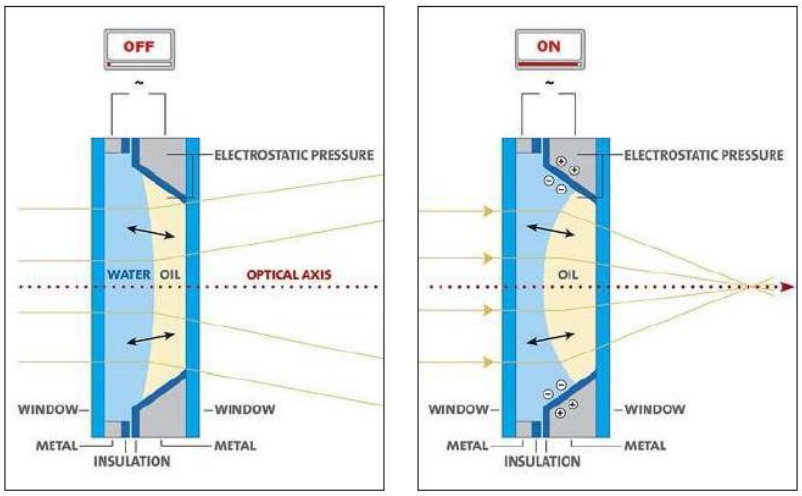

Figure 1-12 Structure of liquid lens developed by Varioptic. [17]

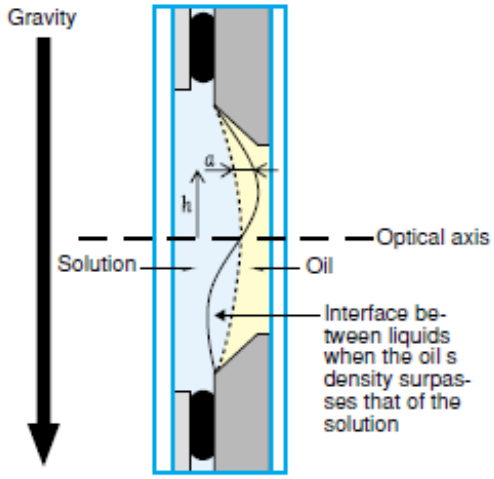

Figure 1-13 The disadvantage of liquid lens is that coma aberration may occur due to gravitational pull. [16]

References

[1] H. Ottevaere, R. Cox, H. P. Herzig, T. Miyashita, K. Naessens, M. Taghizadeh, R. Volkel, H. J. Woo, and H. Thienpont, "Comparing Glass and Plastic Refractive Microlenses Fabricated with Different Technologies," *J. Opt. A: Pure Appl. Opt.*, vol. 8, pp. 407-429. (2006)

[2] Z. D. Popovic, R. A. Sprague, and G. A. Neville Connell, "Technique for Monolithic Fabrication of Microlens Arrays," *Applied Optics*, vol. 27, no. 7, pp. 1281-1284. (1988)

[3] D. Daly, R. F. Stevens, M. C. Hutley, and N. Davies, "The Manufacture of Microlenses by Melting Photoresist," *Meas. Sci. Technol*, vol. 1, pp. 759-766. (1990)

[4] T. R. Jay *et al*, "Preshaping Photoresist for Refractive Microlens Fabrication," *Opt. Eng.*, vol. 33, pp. 3552-3555. (1994)

[5] H. Ottevaere, B. Volckaerts, J. Lamprecht, A. Hermanne, I. Veretennicoff, and H. Thienpont, "2D Plastic Microlens Arrays by Deep Lithography with Protons: Fabrication and Characterization," *J. Opt. A: Pure Appl. Opt.*, vol. 4, pp. 22-28. (2002)

[6] K. Naessens, H. Ottevaere, R. Baets, P. Van Daele, and H. Thienpont, "Direct Writing of Microlenses in Polycarbonate with Excimer Laser Ablation," *Appl. Opt.*, vol. 42, pp. 6349-6359. (2003)

[7] D. L. MacFarlane, V. Narayan, W. R. Cox, T. Chen, and D. J. Hayes, "Microjet Fabrication of Microlens Arrays," *IEEE PTL*, vol. 6, pp. 1112-4. (1994)

[8] L. N. Thibos, "Principles of Hartmann-Shack Aberrometry," *Journal of Refractive Surgery*, vol. 16, pp. 563-565. (2000)

[9] B. Platt, R. Shack, "History and Principles of Shack-Hartmann Wavefront Sensing," *Journal of Refractive Surgery*, vol. 17, pp. 573-577. (2001)

[10] J. E. Greivenkamp, D. G. Smith, "Graphical Approach to Shack-Hartmann Lenslet Array Design," *Proceedings of SPIE*, vol. 47(6), pp. 063601-1 – 063601-4. (2008)

[11] World Forum for Harmonization of Vehicle Regulations (WP.29) [cited; Available from : http://www.unece.org/trans/main/wp29/wp29regs.html

[12] Kelley, Charles R., Ketchel, James M. and Strudwick, Peter H., "Experimental Evaluation of Head-Up Display High Brightness Requirements", Nov. 1965.

[13] Robert D. Brown, David H. Modro, Michael R. Greer, "High resolution LCD projection based color head-up display", Cockpit Displays VIII: Displays for Defense Applications, Proceedings of SPIE Vol. 4362, 2001

[14] Privacy glass. [cited; Availabel from: http://www.polytronix.com/privacyglass_specs.htm

[15] Smart film. [cited; Available from: http://www.polytron.com.tw/

[16] Freeman; Glenn E., PPG Industries Ohio, Inc., *"Windshield for head-up display system"* United States Patent No. US 6636370 B2, Field: August 21, 1998, Date of patent: October 21, 2003.

[17] Weber; Michael F., Ouderkirk; Andrew J., Wheatley; John A., Brodd; Jonathan, 3M Innovative Properties Company, "Head-up display with narrow band reflective polarizer", United States Patent No. US 7123418 B2

PART I MICROLENS ARRAY

Chapter 2 Using Hydrophilic Effect to Fabricate Self-Assembled Microlens Array by UV/ozone Modification

In this chapter, we presented a self-assembled microlens array (MLA) fabricated by use of the hydrophilic effect under ultra-violet (UV)/ozone treatment. This method provides a fast, simple, and low cost process. It does not require lithography or etch-transfer processes. The MLA was made of negative photoresist SU-8 (n = 1.63 @ 530 nm) on a glass substrate. Microlenses from 50 μm to 200 μm diameters were successfully fabricated by using this method. A 10-μm thick shadow mask was used to define the UV/ozone treatment area to create more hydrophilic surfaces on an SU-8 photoresist base layer on a glass substrate. After hydrophilic zones were created, the glass substrate was immersed into a diluted SU-8 photoresist solution and was removed out the solution. Finally, the MLA was formed after UV curing process. The relationships between the focal length of the MLAs and UV/ozone treatment time were systematically investigated.

2.1 Introduction

Micro-lens array (MLA) is an important component and is used widely in many applications, such as increasing the light extraction efficiency [1], beam shaping for illumination or light gathering [2], wavefront sensor [3], and information displays [4]. There have been many techniques to fabricate micro-lens array [5, 6], including thermal reflow, laser ablation, direct laser writing, direct e-beam writing, deep lithography with protons, ink-jet printing, and gray-scale mask methods. However, there are still some drawbacks of these techniques. Thermal reflow method requires high temperature and the need for an etch-transfer process. The limited numerical aperture is also concerned. In the laser ablation, the problems are high facility cost and high energy consumption. For the ink-jet printing, the lens size and alignment accuracy are limited. It is difficult to fit the shape precisely and to distinguish the gray levels in a sharp edge by gray-scale mask method. Therefore, a fast, cost effective, stable, and focal length controllable method is desirable to fabricate MLAs.

There is another approach to fabricate MLAs using hydrophobic effect [7, 8]. This approach offers an attractive alternative because it allows accurate and direct fabrication of polymer microlenses without heating or post etching of the substrate. The approach is based on patterning hydrophobic molecules on a substrate and self-assembly of a liquid pre-polymer. It was affected by different surface energy on the hydrophilic domains. The techniques to create patterns include micro-contact printing (μCP) of self-assembled mono layers (SAMs) [7] and adhesive lithography [8]. It provided a simpler method to fabricate MLAs using the hydrophobic effect. However, it still needs either an etch-transfer process of μCP stamp or lithography for an adhesive substrate. That increases the cost and process complexity.

SU-8 photoresist (MicroChem, MA) has high optical transmittance from visible to near-infrared wavelength and high refractive index (~1.63) [9]. Furthermore, it has better chemical resistance and mechanical strength than other common polymers such as polycarbonate or PMMA. As a result, SU-8 photoresist is ideal for microlens array fabrication [10]. In this work, a transparent and self-assembled MLA fabricated by the hydrophilic effect through ultra-violet (UV)/ozone treatment is presented. A base layer of SU-8 photoresist can be surface modified to become more hydrophilic using UV/ozone cleaner (model UV-1,Samco) [11]. Contact angles on the modified surface were ranged from 27˚ to 15˚ depending on the processing time, UV power and ozone concentration. The light source of UV/ozone cleaner is 110W with primary process wavelength of 254 and 182 nm. The oxygen flow rate is 0.5 L/min. The MLA was made of diluted SU-8 photoresist, which has refractive index mismatch from a glass substrate. This method provides a fast, low cost, no etch-transfer, no lithography fabrication processes. The focal length of MLA is controllable based on UV/ozone treatment. In the following sections, the fabrication process is discussed. The microlenses of different treatments were systematically investigated.

2.2 Fabrication Process

The SU-8 photoresist MLA was fabricated on a glass substrate with a 5-μm SU-8 photoresist base layer. SU-8 is a well-known photoresist which has good mechanical strength and UV curable property. The surface can be modified to be more hydrophilic by using UV/ozone treatment. Figure 2-1 illustrates schematically the fabrication process of SU-8 photoresist MLA by use of the hydrophilic effect through UV/ozone treatment. A 10-μm thick SU-8 photoresist shadow mask with circular openings was used to define the UV/ozone treatment areas on the SU-8 photoresist base layer, as

Figure 2-1(b). The exposed zones were more hydrophilic than the obstructed zones after UV/ozone treatment. According to the surface modification, more treatment time resulted in more hydrophilic surfaces. In other words, a smaller contact angle was formed under longer UV/ozone treatment. After the more hydrophilic zones were created and the SU-8 photoresist mask was removed, the substrate was dipped in and out of the diluted SU-8 photoresist solution with a slow and constant velocity (~ 0.3 mm/sec). The volume ratio of diluted SU-8 photoresist solution was 1: 6 mixture of SU-8 3035 with its thinner, SU-8 thinner 2000. Finally, SU-8 photoresist MLA was formed on the glass substrate after UV curing process, as in Figure 2-1(g).

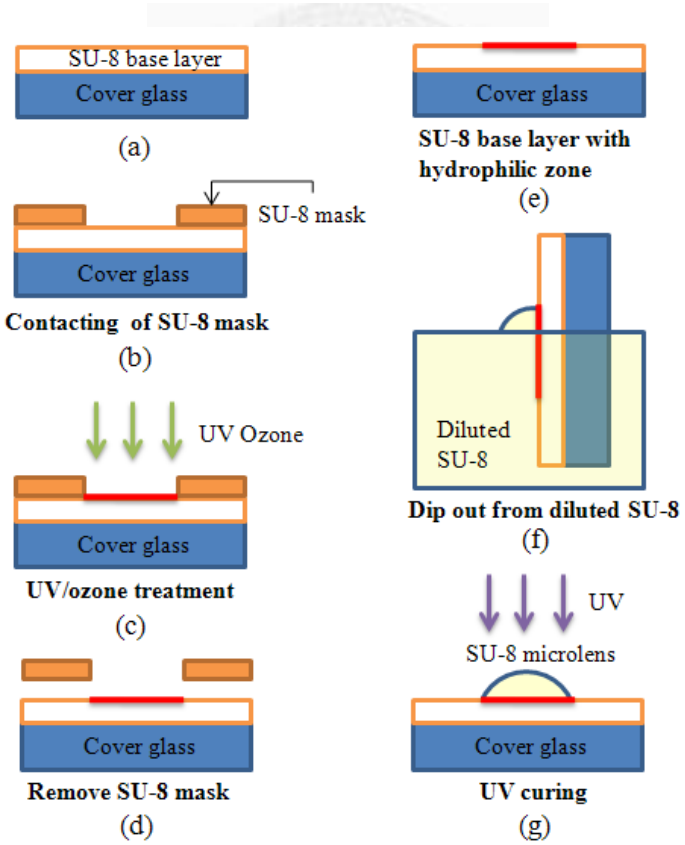

Figure 2-1 The fabrication process of SU-8 photoresist MLA using hydrophilic effect under UV/ozone treatment.

2.3 Experimental Results and Discussions

As mentioned above, the contact angle became smaller with longer UV/ozone treatment time. Figure 2-2 shows the experimental result of contact angles of diluted SU-8 photoresist droplet (~10 μL) with zero, one, two, three, and four minutes UV/ozone treatment time on an SU-8 PR base layer. The measurement system was based on the Sessile Drop Method [12], which was set up by a backlight, a camera, and software programmed by LabVIEW®. The program detected the two endpoints of the footprint and the spherical centroid of the droplet's profile, where the profile was assumed to be spherical because the drop was small so that the gravity can be neglected. Thereafter, the contact angle was derived by the three points. In Figure 2-2, a droplet (~10 μL) was deposited on the sample surface. At least three samples were measured for each treatment time to obtain meaningful data. The contact angles reached its minimum value when UV/ozone treatment time was longer than 3 minute. We used the atomic force microscope (OBJ-204C, ITRI, Taiwan) to measure the surface roughness of the SU-8 base layer before and after four minutes UV/ozone treatment. The average height decreased by 40 nm, and the average surface roughness were both approximately 2 nm as shown in Figure 2-3. It reveals that the UV/ozone treatment did not increase the surface roughness effectively after four minutes UV/ozone treatment.

MLAs were fabricated by use of the 50 μm, 100 μm, and 200 μm openings of the shadow masks under one, two, three, and four minutes UV/ozone treatment time. The gaps between microlenses were 50 μm. The MLAs were finally cured by 2.4 J/cm^2 of UV light (wavelength in 405 μm). The corresponding focal length was measured by optical microscopy. The depth of focus of the microscopy was approximately 2 μm for the object lens whose numerical aperture (NA) was 0.3. Figure 2-4 shows the contact

angles of fabricated microlenses with different opening diameters of shadow mask under different UV/ozone treatment time. It was calculated from the measurement using surface profiler (Alpha Step 500, TENCOR). The longer treatment time resulted in a smaller contact angle. The contact angle of MLA was somehow smaller than those shown at Figure 2-2. This was mainly due to the evaporation of the solvent in the diluted SU-8 photoresist solution after UV curing. From Figure 2-4, the larger opening of the shadow mask also made smaller contact angles, which means the UV/ozone treatment was more effective. UV/ozone treatment longer than three minutes did not make any significant change. But, openings larger than 100 μm did not make any distinguishable difference with the same treatment time. According to the surface profiler measurement, the footprint of the fabricated microlens was smaller than the shadow mask opening. The sizes of MLA were closer to shadow mask openings under longer UV/ozone treatment time. The measured diameters of MLAs which were corresponded to the shadow masks of 50, 100, and 200 μm with one, two, three, and four minutes UV/ozone treatment are listed in Table 2-1. We could see that microlenses are closer to mask size under longer UV/ozone treatment. Focal length measurement of 100-μm diameter microlenses for one, two, three, and four minutes UV/ozone treatment is shown in Figure 2-5. Among the fabricated MLAs, the NAs approximately varied from 0.06 to 0.19 and the focal lengths were from 0.06 mm to 2.78 mm. We verified that longer UV/ozone treatment time results in longer focal length. This agrees well with contact angle and footprint diameter measurement results. In other words, longer UV/ozone treatment results in less curved microlens.

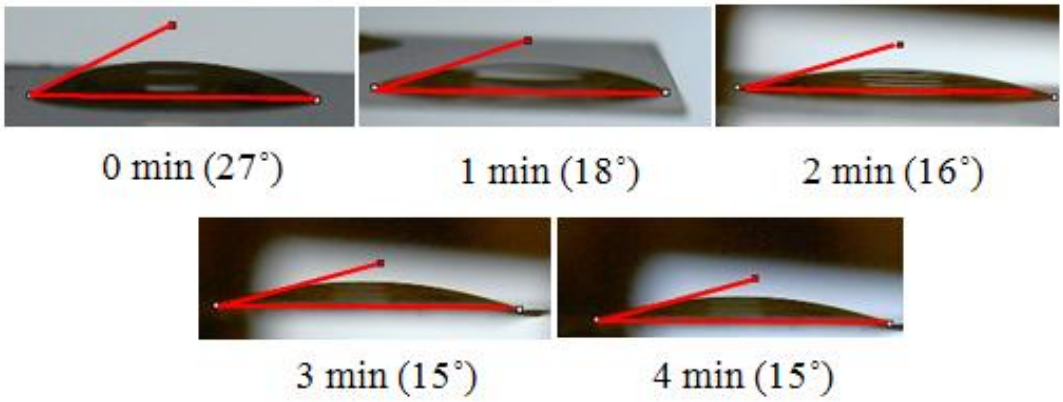

Figure 2-2 The experimental results of contact angles between a non-UV-exposed diluted SU-8 photoresist droplet (~10 μL) and an SU-8 photoresist base layer.

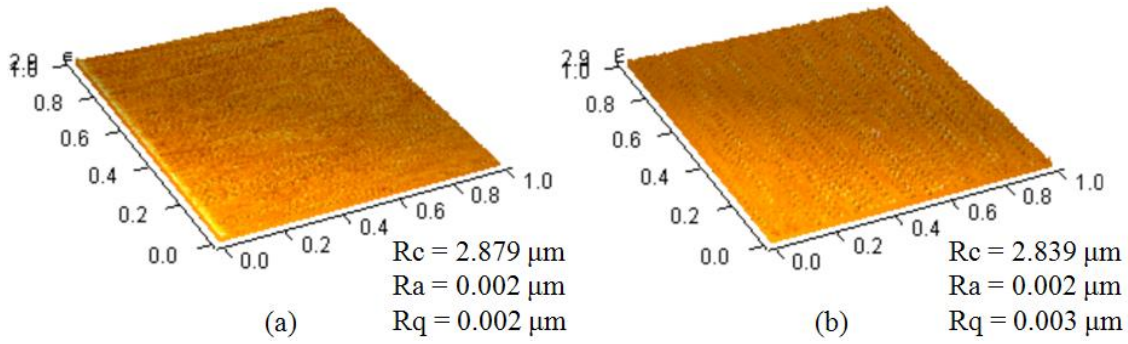

Figure 2-3 Atomic force microscope (AFM) (OBJ-204C, ITRI, Taiwan) images of the SU-8 base layer (a) before and (b) after four minutes UV/ozone treatment. All images were taken at a scan size of 1x1 μm^2 with 128 x 128 $pixel^2$.

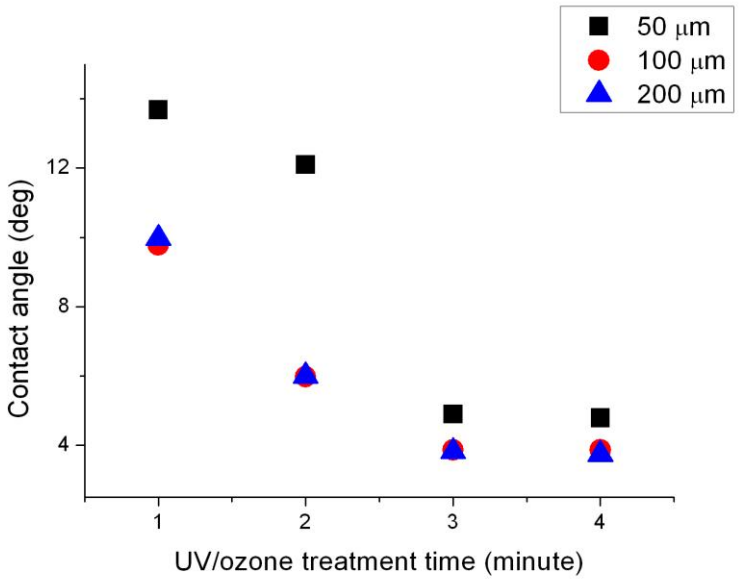

Figure 2-4 The contact angles for different UV/ozone treatment time and different shadow mask openings. The shadow mask openings were 50 μm, 100 μm, and 200 μm in diameters.

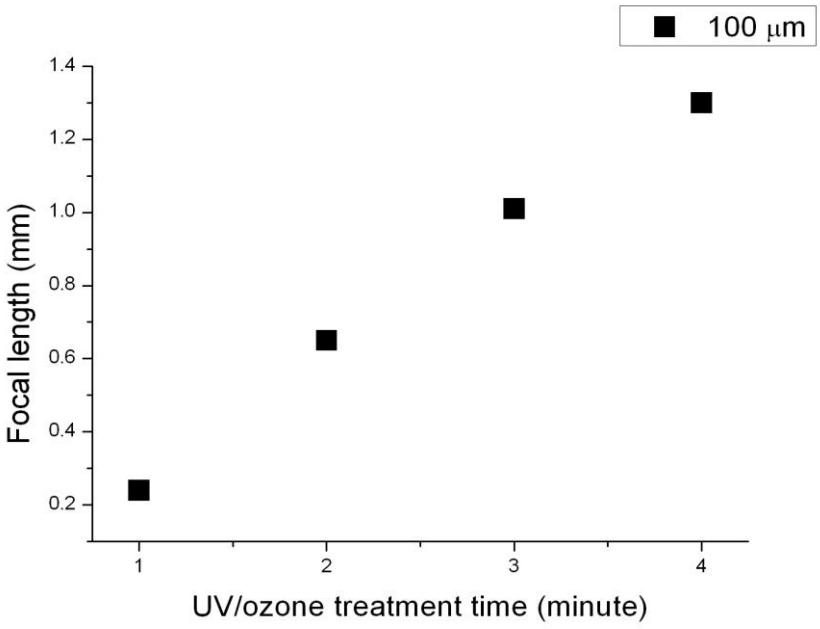

Figure 2-5 Focal length versus UV/ozone treatment time.

Table 2-1 The footprint diameters of MLAs.

Diameter of shadow mask (μm)	UV/ozone treatment time (minute)			
	one	two	three	four
50	20 μm	30 μm	41.3 μm	41.6 μm
100	52 μm	80 μm	86 μm	95.5 μm
200	95 μm	164 μm	182 μm	192 μm

We took the pictures of the MLAs fabricated using 100-μm diameter shadow mask and measured the focus beam spot sizes by optical microscopy in Figure 2-6. It shows the uniform distribution of the intensity profile. Among the fabricated MLAs the average beam spot sizes were from 2.6 μm to 33.8 μm with variation less than 12%. The yield rate was higher than 96 %. We believe this can be further optimized in future. Figure 6 shows the scanning electronic microscopy (SEM) photograph of the microlenses using 100-μm diameter shadow mask under one minute UV/ozone treatment time. The cross section profile in Figure 2-7(e) indicates three layers, which are a glass substrate, a 5-μm thick SU-8 photoresist base layer, and an SU-8 photoresist microlens on the treated area. Two dimensional profiles of MLAs measured by surface profiler showed that the lenses had good surface smoothness. The surface roughness was less than 0.07 μm. This is a typical value for microlenses without going through etching process. We made the curve fitting of the microlens profile by using the SAG equation,

$$z = \frac{cx^2}{1+\sqrt{1-(1+k)c^2x^2}} \tag{1.2}$$

where SAG (z) is the surface at any point x , c is the curvature, and k is the conic

constant. From the fitting result, the conic constant was between -0.005 and 0.00036, which means the surface curvature of MLA fabricated by this method was spherical. We measured the wavefront information by using the commercial Shack-Hartmann wavefront sensor (UI2210-m, UEye, NL) to evaluate the optical quality. The corresponding peak-to-valley (PV) and root-mean-square (RMS) values were lower than 0.949 λ and 0.143 λ as shown in Figure 2-8. The experimental results were summarized in the Table 2-2 below. The yield rates were obtained by average of each 5 samples using the beam spot images. We believe this can be further optimized in future.

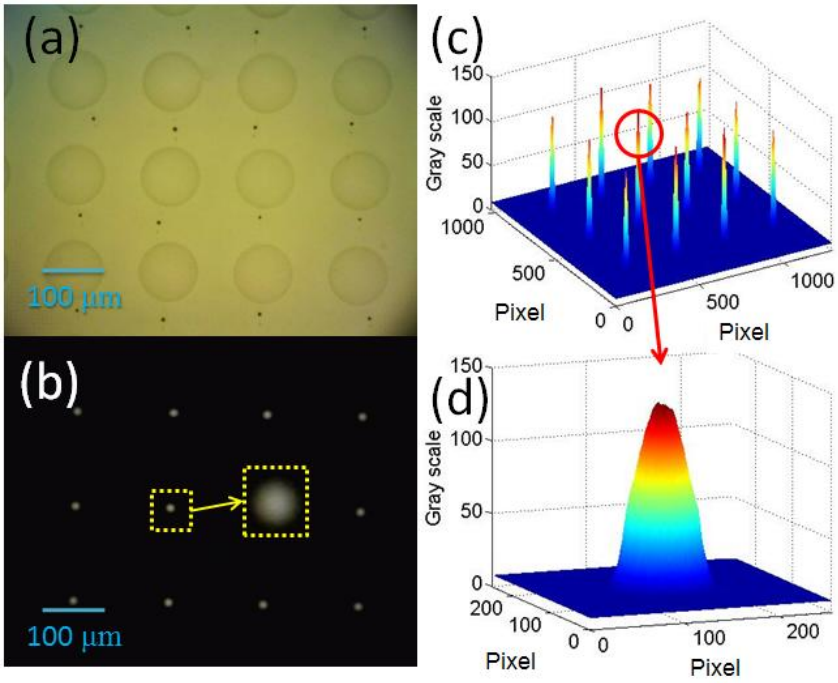

Figure 2-6 The MLAs fabricated using 100-μm diameter shadow mask. (a) Optical microscopy and (b) the corresponding focus points with (c) intensity profile for four minutes UV/ozone treatment time. (d) Zoomed image of the optical intensity profile.

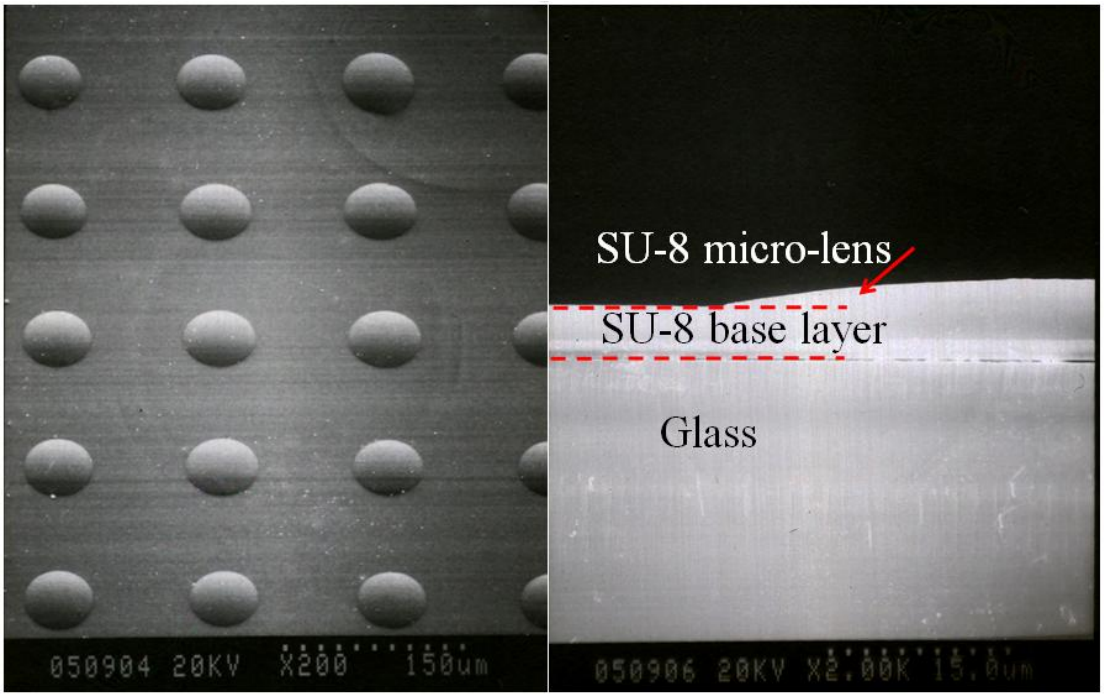

Figure 2-7 The SEM of (a) microlenses of 100 μm diameter under one minute UV/ozone treatment time. (b) the cross section profile of one minute treated microlens.

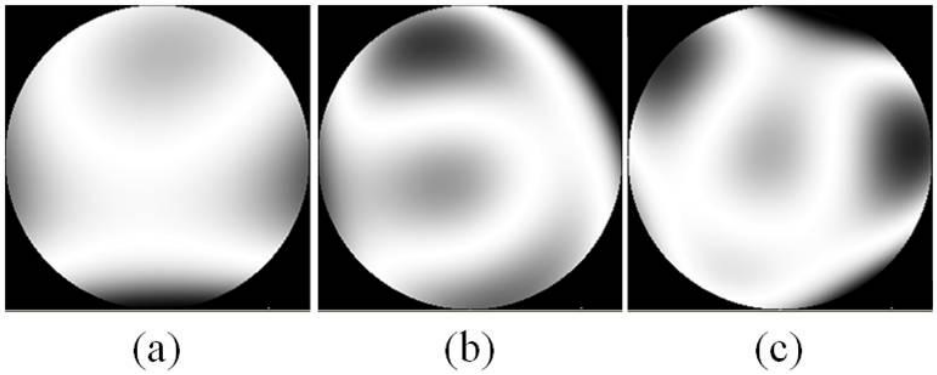

Figure 2-8 The interferogram of the wavefront surface measurement. (a) 50 μm (b) 100 μm (c) 200 μm.

Table 2-2 The summarized results of fabricated MLAs.

Diameter (μm)	UV/ozone time (minute)	Focal length (mm)	Beam Spot Size (μm)	Variation	Yield Rate (%)
50	one	0.06	2.6	< 12%	96.5
	two	0.11	4.7	< 11%	97.1
	three	0.38	7.1	< 4%	98.7
	four	0.39	7.1	< 4%	98.8
100	one	0.24	6.7	< 11%	96.7
	two	0.65	8.9	< 9%	96.9
	three	1.01	9.8	< 4%	97.1
	four	1.35	10.78	< 3%	97.3
200	one	0.44	7.3	< 10%	96.9
	two	1.24	10.2	< 10%	97.8
	three	2.17	32.1	< 5%	97.5
	four	2.78	33.8	< 2%	98.8

2.4 Conclusions

A transparent and self-assembled MLAs fabricated by use of the hydrophilic effect under UV/ozone treatment was presented and demonstrated experimentally. This method provides a fast, low cost, no etch-transfer, no lithography fabrication processes. The MLA was made of negative photoresist SU-8 (n=1.63 @ 530 nm) on a glass substrate. The focal length of MLA is controllable by changing UV/ozone treatment time. A larger shadow mask opening and a longer UV/ozone treatment time produced MLA with longer focal length. MLAs of 50 μm, 100 μm, 200 μm diameters for one, two, three, and four minutes UV/ozone treatment time has been fabricated successfully. The numerical apertures of microlens were from 0.06 to 0.19. The focal lengths were from 0.06 mm to 2.78 mm. The surface roughness was less than 0.07 μm and the shape was nearly spherical. The yield rate was higher than 96 %. The corresponding PV and RMS values of wavefront were lower than 0.949 λ and 0.143 λ.

References

[1] H. Peng, Y. L. Ho, X.-J. Yu, M. Wong, and H.-S. Kwok, "Coupling efficiency enhancement in organic light-emitting devices using microlens array - Theory and experiment," *IEEE/OSA Journal of Display Technology,* vol. 1, pp. 278-282, 2005.

[2] J.-W. Pan, C.-M. Wang, H.-C. Lan, W.-S. Sun, and J.-Y. Chang, "Homogenized LED-illumination using microlens arrays for a pocket-sized projector," *Optics Express,* vol. 15, pp. 10483-10491, 2007.

[3] G. Y. Yoon, T. Jitsuno, M. Nakatsuka, and S. Nakai, "Shack Hartmann wave-front measurement with a large F-number plastic microlens array," *Applied Optics,* vol. 35, pp. 188-188, 1996.

[4] N. A. Davies, M. McCormick, and M. Brewin, "Design and analysis of an image transfer system using microlens arrays," *Optical Engineering,* vol. 33, pp. 3624-3633, 1994.

[5] S. Sinzinger and J. Jahns, *Microoptics*: Wiley-VCH, 1999.

[6] H. Ottevaere, R. Cox, H. P. Herzig, T. Miyashita, K. Naessens, M. Taghizadeh, R. Volkel, H. Woo, and H. Thienpont, "Comparing glass and plastic refractive microlenses fabricated with different technologies," *Journal of Optics A: Pure and Applied Optics,* vol. 8, p. S407, 2006.

[7] H. A. Biebuyck and G. M. Whitesides, "Self-organization of organic liquids on patterned self-assembled monolayers of alkanethiolates on gold," *Langmuir,* vol. 10, pp. 2790-2793, 1994.

[8] D. M. Hartmann, O. Kibar, and S. G. Esener, "Characterization of a polymer microlens fabricated by use of the hydrophobic effect," *Optics Letters,* vol. 25, pp. 975-977, 2000.

[9] O. P. Parida and N. Bhat, "Characterization of optical properties of SU-8 and fabrication of optical components," in *Int. Conf. on Optics and Photonics*, CSIO, Chandigarh, India, 2009.

[10] S.-M. Kuo and C.-H. Lin, "Fabrication of aspherical SU-8 microlens array utilizing novel stamping process and electro-static pulling method," *Opt. Express*, vol. 18, pp. 19114-19119, 2010.

[11] C.-J. Chang, C.-S. Yang, L.-H. Lan, P.-C. Wang, and F.-G. Tseng, "Fabrication of a SU-8-based polymer-enclosed channel with a penetrating UV/ozone-modified interior surface for electrokinetic separation of proteins," *Journal of Micromechanics and Microengineering*, vol. 20, 2010.

[12] K. Oura, *Surface science: an introduction*: Springer, 2003.

Chapter 3 Fabrication of Transparent and Self-Assembled Microlens Array Using Hydrophilic Effect and Electric Fielding Pulling

In this work, we present a variable and self-assembled spherical microlens array (MLA) fabricated by the use of the hydrophilic effect under ultra-violet (UV)/ozone treatment. The optical power and surface roughness of MLA was further enhanced by applying external electric field. This method provides a fast, simple, and low cost process, because it does not require heating, or etch-transfer processes. The MLA was made of negative photoresist SU-8 (n = 1.63) on a glass substrate. Microlenses from 50 μm to 200 μm diameters with one, two, three, and four minutes UV/ozone treatment time were successfully fabricated. The optical focusing power of 100-μm diameter MLA was also improved by using electric field of 1.7 V/μm, and 3.4 V/μm. A 10-μm thick shadow mask was used to define the UV/ozone treatment area to create more hydrophilic surfaces on an SU-8 photoresist base layer on a glass substrate. After hydrophilic zones were created, the glass substrate was immersed into a diluted SU-8 photoresist solution and then removed. Finally, the MLA was formed after applying parallel electric field followed by UV curing process. The MLA was kept in spherical shape while the radius of curvature was changed. The focal length from 0.09 mm to 2.91 mm of spherical MLA were experimentally demonstrated and investigated.

3.1 Introduction

Micro-lens array (MLA) is an important component which is used widely in many applications, such as increasing the light extraction efficiency [1], Shack Hartmann wavefront sensor [2], beam shaping for illumination [3], light gathering for solar collectors [4], and information displays [5]. There have been many techniques to fabricate micro-lens array, including thermal reflow [6], UV resin stamping [7], laser ablation [8], ink-jet printing [9], direct laser writing [10], and gray-scale mask photolithography [11] methods. Most of these mentioned methods have the drawbacks of high facility cost, time consumption, alignment inaccuracy, or high temperature process. The main problem of the high temperature process in some of these methods is inducing device defects in several applications, such as backlight module of liquid crystal display (LCD) and the encapsulation of light emitting diode (LED). There is another approach to fabricate MLAs by the use of hydrophobic effect [12, 13]. This approach allows accurate and direct fabrication of polymer microlens array without heating. Thus, using the hydrophobic effect to fabricate MLAs is a simpler way. However, it still requires either an etch-transfer process or lithography to define hydrophobic boundaries, which increases the cost and process complexity. Therefore, a cost effective and low temperature process is still desirable to fabricate MLAs.

SU-8 photoresist (MicroChem, MA) has high optical transmittance from visible to near-infrared wavelength and high refractive index (~1.63) [14]. Furthermore, it has better chemical resistance and mechanical strength than other popular polymers, such as polycarbonate or poly-methyl-methacrylate (PMMA). As a result, SU-8 photoresist is an ideal material for microlens array fabrication [7]. The polar molecules of SU-8 photoresist enable them to be easily deformed via an external electric field [15]. The

footprint of SU-8 photoresist liquid droplet was fixed on a substrate and the center part, or sag height, was pulled up. This made a higher sag height and a corresponding larger optical power [16].

In this work, a transparent and self-assembled MLA in spherical shape was fabricated by the use of hydrophilic effect and external electric field pulling. A base layer of SU-8 photoresist can be surface modified to become more hydrophilic using ultra-violet (UV)/ozone cleaner [17]. The MLA was made of diluted SU-8 photoresist on the SU-8 photoresist base layer. It was self-assembled by the balance of surface tension energy on the SU-8 photoresist base layer of more-hydrophilic circular zones. In some applications, a larger optical power MLA is desirable. Therefore, an external electric field was applied to increase the optical power and to smooth the surface roughness before UV curing of SU-8 photoresist. The presented method provides a fast, low cost, and no etch-transfer process. The entire fabrication was done in room temperature to prevent it from thermal residual stress and material issues. The radius of curvature of the microlens can be easily controlled by the design of shadow mask opening, the UV/ozone treatment time, and the external electric field. In the following sections, the working principle and fabrication process are discussed. This work investigates the focal length of MLA under different lens diameters, the UV/ozone treatment time and the electric field strength. Experimental results of optical microscopy images, focus spot diagrams, lens profiles, surface roughness, and scanning electric microscope (SEM) images of the fabricated MLA were presented in this work.

3.2 The working mechanism

The SU-8 photoresist MLA was fabricated on an ITO (Indium Tin Oxide) glass

substrate with an SU-8 photoresist base layer. SU-8 is a well-known photoresist which has good mechanical strength and UV curable property. The surface can be modified to be more hydrophilic by using UV/ozone treatment. It generates O−H on the phenol group, C=O and O−C=O hydrophilic function on SU-8 photoresist surfaces. This contributes to the hydrophilic surface of SU-8 polymer. The contact angle on the modified surface depends on the processing time, UV power and ozone concentration. The polar molecules enable SU-8 photoresist structures to be easily deformed by an external applied electric field. The larger electric field results in a higher sag height of the microlens. The SU-8 photoresist base layer keeps the microlens as a spherical profile via an external electric field. The base layer is served as a dielectric middle layer between SU-8 microlens and ITO conductive layer. Figure 3-1 illustrates schematically the working principle of SU-8 photoresist MLA by the use of the hydrophilic effect through UV/ozone treatment and the external electric field pulling. A 10-μm thick SU-8 photoresist shadow mask with circular openings was used to define the UV/ozone treatment areas on the SU-8 photoresist base layer, as in Figure 3-1(a). The exposed zones became more hydrophilic than the obstructed zones after UV/ozone treatment, as in Figure 3-1(b). According to the surface modification, more treatment time results more hydrophilic surfaces. In other words, a smaller contact angle was formed under longer UV/ozone treatment time. After the more hydrophilic zones were created and the SU-8 photoresist mask was removed, the substrate was dipped in and out of the diluted SU-8 photoresist solution with a slow and constant velocity (approximately 0.3 mm/sec), as in Figure 3-1(c). Finally, SU-8 photoresist MLA was formed on the substrate after applying an external electrical field and UV curing process, as in Figure 3-1(d).

The presented self-assembled technique utilizes the crosslink between SU-8 microlens and SU-8 base layer. It is very strong and not easy to be broken. The

concentration of diluted SU-8 photoresist must be diluted to automatically stay on the areas with more hydrophilic property. Because of the evaporation of the solvent after UV curing process, the volume of the diluted SU-8 photoresist liquid microlens shrank. Therefore, the contact angle was smaller compared with the default one and the footprint area was smaller than the shadow mask opening. In general, a higher surface energy of SU-8 base layer results in a larger footprint area. In the other words, longer UV/ozone treatment time and larger shadow mask opening result in higher surface energy. On the other hand, the external electric field reduces the surface energy of SU-8 base layer. It increases the contact angles of SU-8 microlens, which decreases the radius of curvature and keeps the spherical profile. In these regards, the shape and the size can be manipulated by controlling the UV/ozone treatment time, the shadow mask opening, and the external applied voltage for this process.

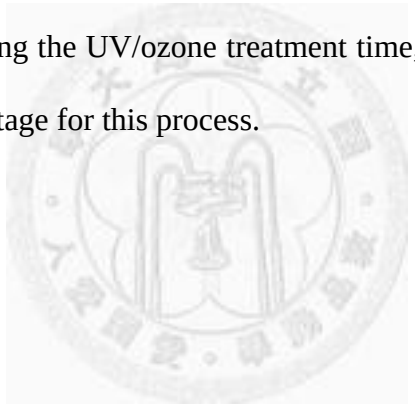

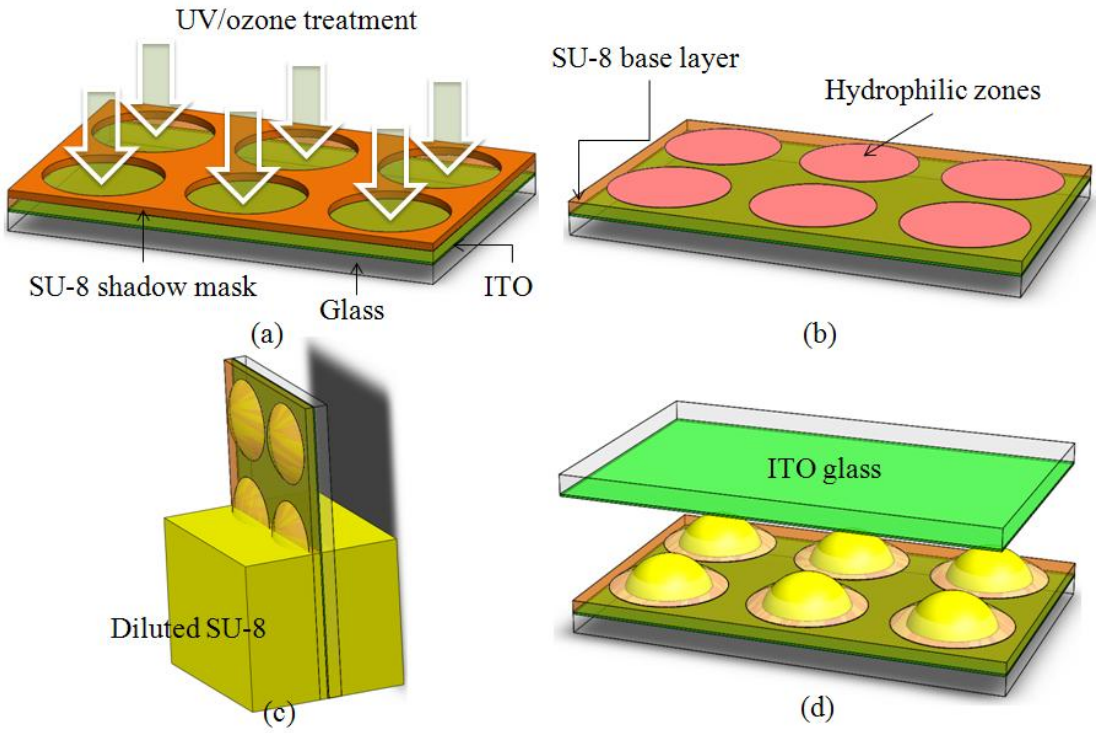

Figure 3-1 The schematic of the presented fabrication of the SU-8 MLA.(a) UV/ozone treatment (b) Hydrophilic zones is presented (c) Dip out from the diluted SU-8 photoresist solution (d) Apply the external voltage.

3.3 Fabrication processes

In order to define the hydrophilic zones, we fabricated an SU-8 photoresist shadow mask at first. The SU-8 photoresist shadow mask has good mechanical strength and chemical resistance; therefore, it is removable and reusable. It was fabricated by micromachining processes. First, the SU-8 photoresist was spun on the glass substrate with the speed of 500 rpm for 5 sec and 1000 rpm for 30 sec. Then, it was soft baked at 95 ℃ for 3 min followed by 3.2 J/cm^2 exposure in the wavelength of 405 μm with optical masks of 50 μm, 100 μm, and 200 μm diameters. The post exposure baking was 65 ℃ for 2 min and 95 ℃ for 1 min. The hard backing was 150 ℃ for 3 min. Finally,

The SU-8 photoresist shadow mask with circular openings was released by isotropic etching in buffered oxide etcher (BOE). The thickness of shadow mask was approximately 10 μm.

In this study, ITO glass (LT-G001, Lumtek Corp., Taiwan) with 1.1 mm of glass thickness and 1600 Å of ITO thickness was cut into pieces with a dimension of 25 mm and 25 mm. It was used as the substrate. The ITO resistance was 15 Ω/sq and the transparency of ITO was larger than 84% at wavelength of 550 nm. A commercially available SU-8 3035 negative photoresist, an SU-8 2000 thinner, and an SU-8 developer were used in this fabrication (MicroChem Corp., MA, USA). For cleaning the substrate, the ITO glass was first cleaned with acetone, isopropanol alcohol (IPA) and deionized (DI) water, and then dehydrated on a hot plate with a temperature of 100 ℃ for 10 min. Figure 3-2 shows schematic drawings of the fabrication process of the presented method. The detailed fabrication processes are described below.

3.3.1 SU-8 photoresist base layer

In this work, we chose ITO glass as a substrate because its hydrophilic surface produces a flatter coating of SU-8 photoresist and the ITO was served as a conductive layer. We employed the spin coating method (NMC-W-1102, Laurell Technologies Corp., USA) to coat SU-8 photoresist on the ITO glass. The spin speed was 500 rpm for 5 sec and 4000 rpm for 30 sec. In order to produce a thinner SU-8 photoresist layer, the weight ratio of it was a 10:8 mixture of SU-8 3035 and SU-8 2000 thinner. The baking process was skipped in order to control the process at room temperature. It was finally exposed to 9.6 J/cm^2 of UV curing. An SU-8 photoresist base layer with 5 μm thickness was formed, as shown in Figure 3-2(a).

3.3.2 UV/ozone treatment

As described before, the surface of SU-8 photoresist was more hydrophilic via UV/ozone treatment. It depends on the processing time, UV power and ozone concentration. The light source of UV/ozone cleaner (model UV-1, Samco) is 110 W at wavelength between 254 nm and 182 nm. The oxygen flow rate is 0.5 L/min. In order to define the microlens footprint areas, the SU-8 shadow masks with 50 μm, 100 μm, and 200 μm diameter openings were applied on the SU-8 photoresist base layer as shown in Figure 3-2(b). Afterwards, UV/ozone treatment was applied within one, two, three, and four minutes on different size of shadow masks as shown in Figure 3-2(c). After the UV/ozone treatment, the SU-8 photoresist shadow mask could be removed easily and stored for later usage as shown in Figure 3-2(d). Therefore, the SU-8 photoresist base layer with circular zones which were more hydrophilic was formed as in Figure 3-2(e).

3.3.3 Dipping in and out of diluted SU-8 photoresist

After the more hydrophilic zones were created and the SU-8 photoresist shadow mask was removed, the substrate was dipped in and out of the diluted SU-8 photoresist solution with a slow and constant velocity (approximately 0.3 mm/sec) as in Figure 3-2(f). The volume ratio of the diluted SU-8 photoresist solution was a 1: 6 mixture of SU-8 3035 and SU-8 2000 thinner. The mixture should be diluted so that the viscosity was low enough to ensure separation of SU-8 solution on different zones on the SU-8 photoresist base layer due to surface energy difference. The MLA was created after taking out of the diluted SU-8 photoresist solution. At this time, the MLA was still liquid.

3.3.4 Applying electric field and UV curing

Finally, the ITO glass substrate with fabricated MLA was then applied by an external electric field to pull liquid SU-8 into desirable curvature. The electric fields were 1.7 V/μm and 3.4 V/μm, respectively. The fabricated SU-8 photoresist MLA was then exposed to UV light radiation with 7.2 J/cm^2 at the wavelength of 405 μm, as in Figure 3-2(g), to be the final step in making cross-linked SU-8 MLA with high mechanical strength. A shorter focal length MLA was fabricated when it was compared with the MLA without an external electric field pulling.

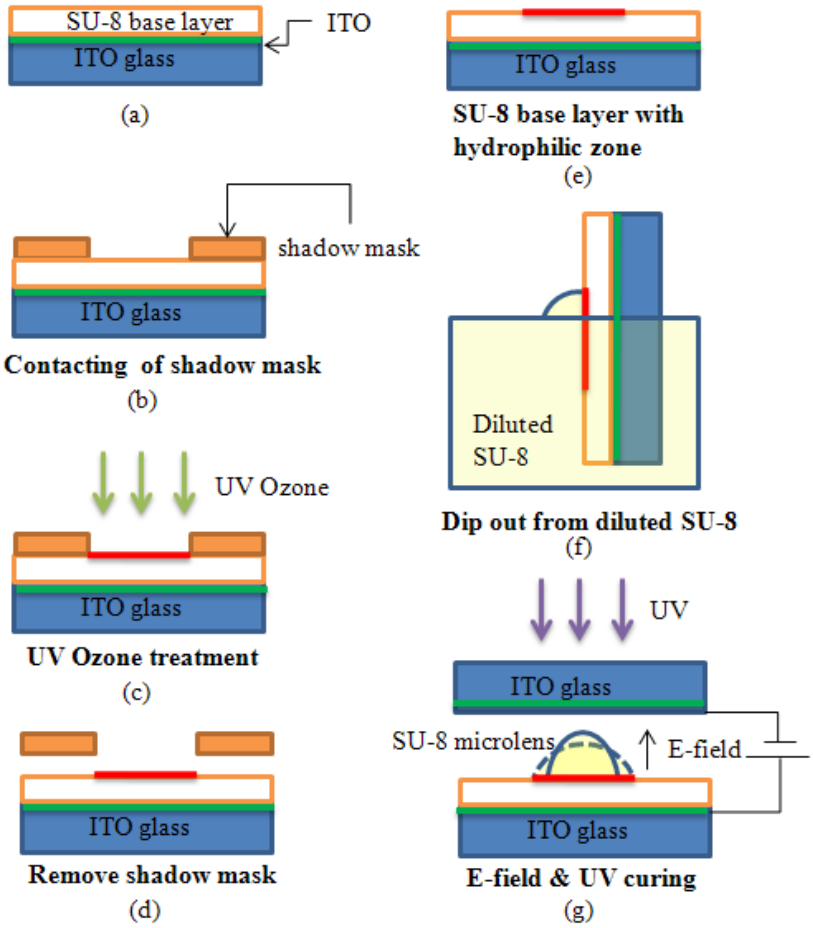

Figure 3-2 The fabrication process. (a) An SU-8 base layer on the ITO glass (b) Contact shadow mask (c) UV/ozone treatment (d) remove shadow mask (e) Hydrophilic zones presented (f) Dip out from diluted SU-8 photoresist solution (g) Apply the external voltage.

3.4 Experimental results and discussions

MLAs of 100 μm diameter with four minutes UV/ozone treatment time were treated with 1.7 V/μm, and 3.4 V/μm electrical fields to enhance optical focusing power. At the same time, the MLAs were cured by 7.2 J/cm^2 of UV light (wavelength at 405 μm). The process temperature was kept at the room temperature. This feature results in no thermal

residual stress. The MLAs were measured by using scanning electron microscope (SEM), surface profiler, and optical microscope. Figure 3-3(a) and (b) show the scanning electronic microscopy (SEM) photograph of the four minutes UV/ozone treated MLA of 100 μm diameter without and with 3.4 V/μm of applying electric field. It shows that the sag height of MLA is higher under electric field pulling. The cross section profile in Figure 3-3(c) shows four layers, which are a glass substrate, an ITO conductive layer, an SU-8 photoresist base layer and an SU-8 photoresist microlens.

Two dimensional profiles of MLAs were measured by surface profiler (Alpha Step 500, TENCOR), as shown in Figure 3-4. It shows that the lenses had good surface smoothness. The surface roughness of the 100 μm MLAs via electric fields of 1.7 V/μm, and 3.4 V/μm were 40 nm, and 30 nm, respectively. The surface roughness of 100 μm MLAs without electric field was 70 nm. Therefore, a larger electric field resulted in a better surface roughness. These are typical values for microlenses without going through etching process. The surface profiles show that the sag height increases, the footprint diameter decreases, and the contact angle increases as the electric field increases. This phenomenon agrees with the previous work [14]. We made the curve fitting of the microlens profile in Figure 3-5 by using the sag equation,

$$z = \frac{cx^2}{1+\sqrt{1-(1+k)c^2x^2}} \tag{1.3}$$

, where sag z is the surface at any point x , c is the curvature, and k is the conic constant. From the fitting result, the conic constants were approximately 0.0002, -0.002, and -0.006, corresponding to 0 V/μm, 1.7 V/μm, and 3.4 V/μm of electric field respectively. It also indicates that the surface of MLA fabricated by this method was nearly spherical. Meanwhile, the radius of curvature was decreased from 0.85 to 0.38.

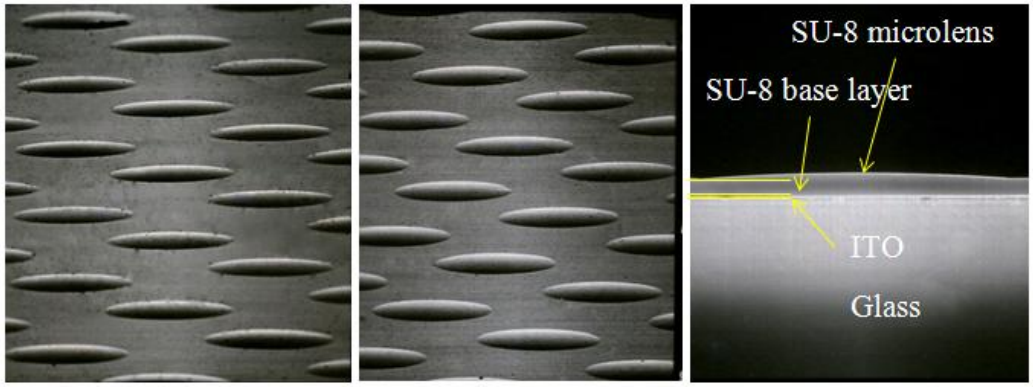

Figure 3-3 SEM images of 4 minutes UV/ozone treated MLA of 100 μm diameter (a) without and (b) with external electric field of 3.4 V/μm. (c) The cross section profile of an SU-8 microlens.

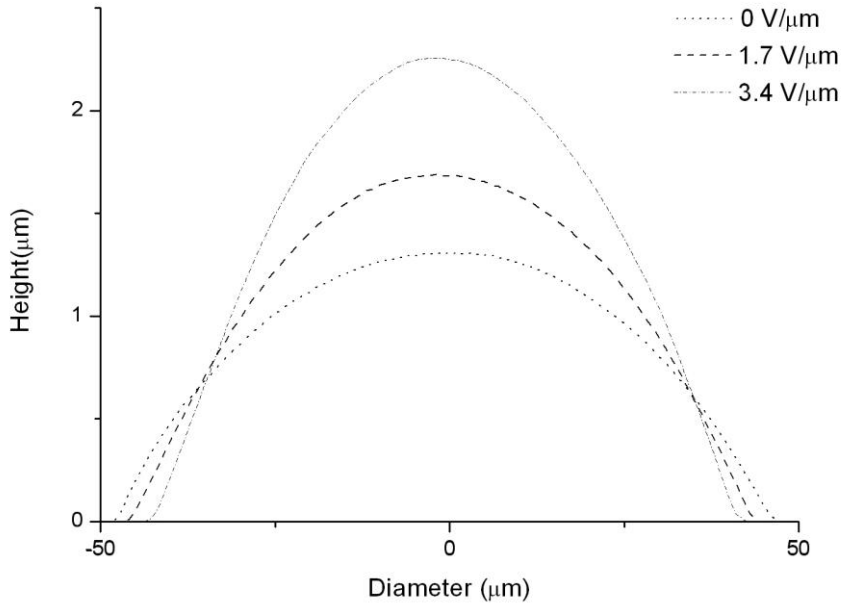

Figure 3-4Surface profile of microlens via different electric fields.

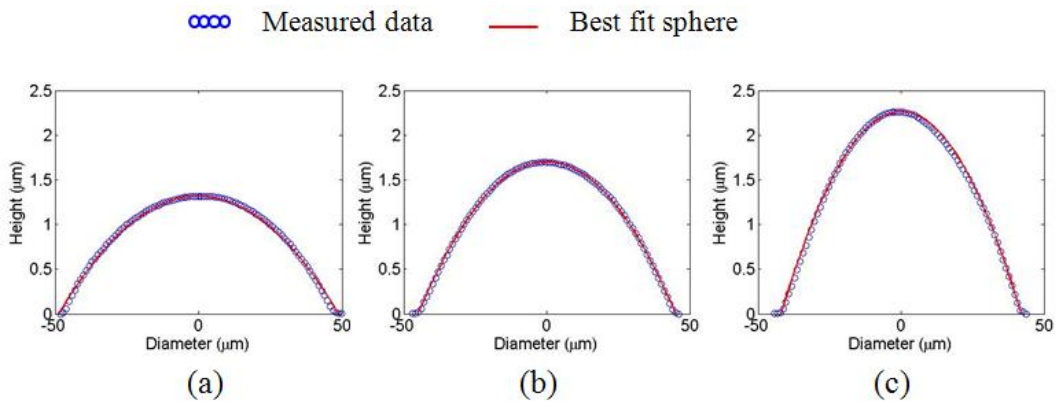

Figure 3-5 Lens profile and the corresponding best fit sphere of the fabricated microlens (a) without applied electric field, (b) with 1.7 V/μm, and (c) 3.4 V/μm measured by probe-type surface analyzer. The circles show measure points and solid red lines are best fit spheres.

As mentioned above, the contact angle became smaller with longer UV/ozone treatment time. According to the reference [17], water contact angles on the modified surface ranged from 72◦ to 12◦ depending on the processing time, UV power and ozone concentration. The measurement system was based on the Sessile Drop Method, which was set up by a backlight, a camera, and software programmed by LabVIEW® . The program detected the two endpoints of the footprint and the spherical centroid of the droplet's profile, where the profile was assumed to be spherical because the drop was small so that the gravity can be neglected. Thereafter, the contact angle was derived by the three points. The diluted SU-8 photoresist droplet (~10 μL) contact angles were measured after one, two, three, and four minutes UV/ozone treatment of SU-8 base layer. At least three samples were measured for each treatment time to obtain meaningful data. The contact angles of the diluted SU-8 photoresist were 27˚, 18˚, 16˚, 15˚, and 15˚ at which were without, with one, two, three, and four minutes UV/ozone treatment

correspondingly. The MLAs were fabricated by the use of the 50 μm, 100 μm, and 200 μm openings of shadow masks under one, two, three, and four minutes UV/ozone treatment time without external electric field yet. The gaps between microlenses were 50 μm. Figure 3-6 shows the contact angles of microlenses with different opening diameters of shadow mask under different UV/ozone treatment time. These angles were calculated by the footprint diameter and the sag height which were measured by using the surface profiler. The longer treatment time resulted in a smaller contact angle. By comparing the contact angles of non-UV-exposed (uncured) SU-8 photoresist droplet and the UV-exposed (cured) microlenses, the contact angle of MLA was somehow smaller than the non-UV-exposed SU-8 photoresist droplet without shadow mask. This was mainly due to the evaporation of the solvent in the diluted SU-8 photoresist solution after UV curing. From Figure 3-6, the larger opening of the shadow mask also made smaller contact angles, which means that the UV/ozone treatment was more effective. But, openings larger than 100 μm did not make any distinguishable difference. UV/ozone treatment time longer than three minutes did not make any significant change either.

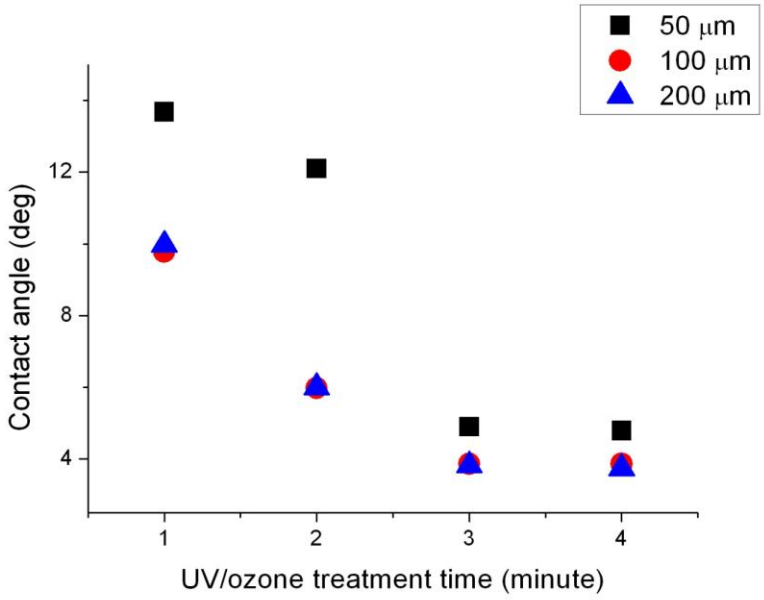

Figure 3-6 The experimental results of UV/ozone treatment time versus contact angle. The black solid squares are the experimental results of contact angles between a non-UV-exposed diluted SU-8 photoresist droplet and an SU-8 photoresist base layer.

We moved the stage of optical microscope (ECLIPSE 50i with 20X objective, Nikon, Japan) up and down to get two clear images at a focus spot and microlens captured by a CCD camera (CoolPix4500, Nikon, Japan). The focal length was approximately the vertical traveling distance of the stage positions referring to two clear image planes. Because of a high NA (= 0.3) objective lens, the depth of focus (DOF) of a microscopy is very small (~2 μm). The accuracy of image plane position is around 2 μm. We measured the fabricated microlens with different UV/ozone treatment time and without external electric field enhancement yet. The distances between the light focusing point and vertex of a microlens (or focal lengths) were listed in Table 3-1. The SU-8 photoresist MLAs were measured under microscope with bottom emitting

light. From this table, we noticed that the larger microlens diameter and the longer UV/ozone time resulted in longer focal length.

Table 3-1 The focal length, sag height, and radius of curvature of fabricated MLA by different UV/ozone treatment time without external electric field enhancement.

Diameter (μm)	UV/ozone time (minute)	Focal length (mm)	Sag Height (μm)	Radius of Curvature (mm)
50	One	0.09	1.54	0.06
	Two	0.13	1.42	0.08
	Three	0.39	0.89	0.24
	Four	0.40	0.87	0.25
100	One	0.24	2.27	0.15
	Two	0.65	1.95	0.41
	Three	1.28	1.14	0.81
	Four	1.35	1.34	0.85
200	One	0.40	4.55	0.25
	Two	1.30	4.11	0.82
	Three	2.87	2.28	1.81
	Four	2.91	2.52	1.83

We also measured the MLAs pulled by electric field. The focal lengths were approximately 0.9 mm and 0.6 mm. A larger electric field resulted in a shorter focal length, or larger optical power. We took the optical microscopy images of the 100 μm diameter MLAs that went through different electric field pulling and re-plotted the intensity profile of the focus beam spot (focal point) in Figure 3-7. The top three optical microscope pictures captured by a CCD camera indicate that a larger electric field produces a smaller fabricated diameter. This phenomenon was caused by the previously mentioned electric field-dependent surface tension effect. The spots of the middle row of pictures were measured by using an optical microscope with a bottom emitting light

source. Because the distance between the light source and MLA (~12 cm) is much larger than the diameter of the microlens, the rays are approximately parallel to the optical axis and focus on a spot with a 150 μm pitch. The image was then gray-scaled and analyzed using the commercial software Matlab® to calculate the intensity profile of each light spot, as in the bottom of Figure 3-7. The spot profiles are symmetric, which means that each SU-8 photoresist microlens in MLAs was in good quality. Because the variation between focus light spots was not significant, the uniformity was high. The FWHM (Full Width of Half Maximum) focus beam spot sizes are listed in table 2, which were smaller than 11 μm in diameter. This phenomenon agrees with previous discussion that the focus spot is smaller when the optical power is higher. The yield rate is an important index to determine the practicability. We averaged five pieces of MLA samples via each electric field by using the beam spot images and then listed in the Table 3-2. It shows good reproducibility of this presented method since the yield rates are higher than 97%. Finally, we summarized the results of the fabricated MLA in table 2.

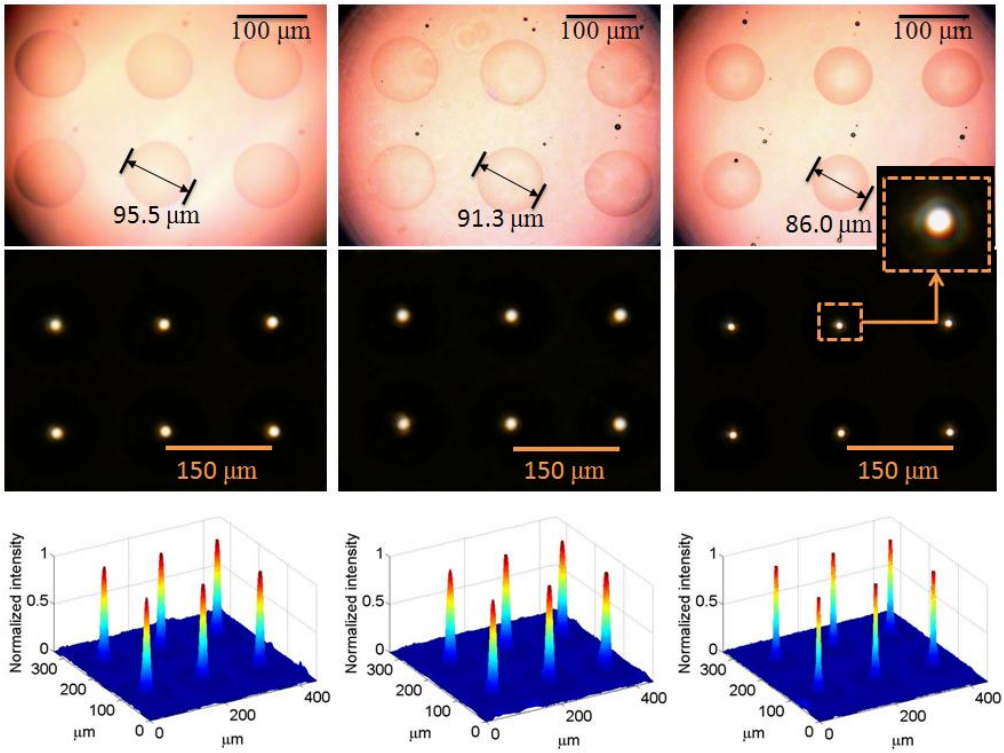

(a) 0 V/µm (b) 1.7 V/µm (b) 3.4 V/µm

Figure 3-7 MLAs of 100 µm diameter with 4 minutes UV/ozone treatment time via electric fields of (a) 0 V/µm, (b) 1.7 V/µm, and (c) 3.4 V/µm and the corresponding focus beam spots.

Table 3-2 The summarized results of the fabricated MLA.

Electric field (V/μm)	Focal length (mm)	Lens diameter (μm)	Lens sag height (μm)	Radius of Curvature (mm)	Beam spot size (μm)	Surface roughness (nm)	Yield rate (%)
0	1.35	95.5	1.34	0.85	10.78	70	97.3
1.7	0.94	91.3	1.75	0.59	9.8	40	98.1
3.4	0.61	86.0	2.38	0.38	5.88	30	98.5

3.5 Conclusions

A transparent, self-assembled, variable, and spherical MLAs fabricated by use of the hydrophilic effect under UV/ozone treatment via electric field enhancement were presented and demonstrated experimentally. The MLA was made of negative photoresist SU-8 (n=1.63) on an ITO glass substrate. The focal length of MLA was controllable by changing UV/ozone time and external electric field. A larger shadow mask opening, a longer UV/ozone treatment time, and a smaller electric field produced MLA with longer focal length. MLAs of 50 μm, 100 μm, 200 μm diameters for one, two, three, and four minutes UV/ozone treatment time have been fabricated and investigated. MLA of 100 μm via electric field of 1.7 V/μm and 3.4 V/μm has been fabricated successfully. The external electric field not only increases the optical power but also makes the surface roughness smaller. The focal lengths of microlens were varied from 0.09 mm to 2.91 mm. The surface roughness was less than 70 nm and became better under larger electric field pulling. The shape of a microlens was nearly spherical. We verify that this method provides a fast, low cost, no etch-transfer and room temperature fabrication process.

References

[1] Peng H, Ho YL, Yu X-J, Wong M and Kwok H-S. Coupling efficiency enhancement in organic light-emitting devices using microlens array - Theory and experiment. *IEEE/OSA Journal of Display Technology*. 2005; 1: 278-82.

[2] Yoon GY, Jitsuno T, Nakatsuka M and Nakai S. Shack Hartmann wave-front measurement with a large F-number plastic microlens array. *Applied Optics*. 1996; 35: 188-.

[3] Pan J-W, Wang C-M, Lan H-C, Sun W-S and Chang J-Y. Homogenized LED-illumination using microlens arrays for a pocket-sized projector. *Optics Express*. 2007; 15: 10483-91.

[4] Karp JH, Tremblay E, Hallas JM and Ford JE. Orthogonal and secondary concentration in planar micro-optic solar collectors. *Optics Express*. 2011; 19: A673-A85.

[5] Davies NA, McCormick M and Brewin M. Design and analysis of an image transfer system using microlens arrays. *Optical Engineering*. 1994; 33: 3624-33.

[6] Daly D, Stevens RF, Hutley MC and Davies N. Manufacture of microlenses by melting photoresist. *Measurement Science and Technology*. 1990; 1: 759-66.

[7] Kuo S-M and Lin C-H. Fabrication of aspherical SU-8 microlens array utilizing novel stamping process and electro-static pulling method. *Opt Express*. 2010; 18: 19114-9.

[8] Mihailov S and Lazare S. Fabrication of refractive microlens arrays by excimer laser ablation of amorphous Teflon. *Applied Optics*. 1993; 32: 6211-8.

[9] Danzebrink R and Aegerter MA. Deposition of micropatterned coating using an ink-jet technique. *Thin Solid Films*. 1999; 351: 115-8.

[10] Ornelas-Rodriguez M and Calixto S. Direct laser writing of mid-infrared microelements on polyethylene material. *Optical Engineering*. 2001; 40: 921-5.

[11] Rogers JD, Karkkainen AHO, Tkaczyk T, Rantala JT and Descour MR. Realization of refractive microoptics through grayscale lithographic patterning of photosensitive hybrid glass. *Optics Express*. 2004; 12: 1294-303.

[12] Biebuyck HA and Whitesides GM. Self-organization of organic liquids on patterned self-assembled monolayers of alkanethiolates on gold. *Langmuir*. 1994; 10: 2790-3.

[13] Hartmann DM, Kibar O and Esener SG. Characterization of a polymer microlens fabricated by use of the hydrophobic effect. *Optics Letters*. 2000; 25: 975-7.

[14] Parida OP and Bhat N. Characterization of optical properties of SU-8 and fabrication of optical components. *Int Conf on Optics and Photonics*. CSIO, Chandigarh, India2009.

[15] Zhan Z, Wang K, Yao H and Cao Z. Fabrication and characterization of aspherical lens manipulated by electrostatic field. *Applied Optics*. 2009; 48: 4375-80.

[16] Bateni A, Laughton S, Tavana H, Susnar S, Amirfazli A and Neumann A. Effect of electric fields on contact angle and surface tension of drops. *Journal of colloid and interface science*. 2005; 283: 215-22.

[17] Chang C-J, Yang C-S, Lan L-H, Wang P-C and Tseng F-G. Fabrication of a SU-8-based polymer-enclosed channel with a penetrating UV/ozone-modified interior surface for electrokinetic separation of proteins. *Journal of Micromechanics and Microengineering*. 2010; 20.

Chapter 4 Self-assembled microlens on top of light emitting diodes using hydrophilic effect for improving extraction efficiency and increasing viewing angle

In this work, we propose a self-assembled microlens arrays (MLAs) on top of light emitting diodes (LEDs) based on hydrophilic effect under ultraviolet (UV)/ozone treatment to improve extraction efficiency and to increase viewing angle. The LED chip was encapsulated by polydimethylsiloxane (PDMS) (n = 1.44) before the fabrication process of MLA. The MLA was made of transparent negative photoresist SU-8 (n = 1.63). The SU-8 photoresist became more hydrophilic after UV/ozone treatment. After hydrophilic zones were produced by using shadow masks and UV/ozone, the substrate with hydrophilic zones was dipped in and out of diluted SU-8 photoresist solution with slow and constant velocity. Meanwhile, a 200-μm MLA was formed by self-surface tension and cohesion of diluted SU-8. Finally, MLA was hardened after UV curing. This approach is low cost and low time-consuming. It did not require photo masks, heating, or etch-transfer processes. It's a new fabrication method that can be easily applied to opto-electronic devices. Integration with LED, extraction efficiency was improved 15% and 28% in maximum and total accordingly, and viewing angle was increased 17 degree.

4.1 Introduction

Light emitting diodes (LEDs) are important and popular light source for general lighting and the backlight unit of displays. The well-known advantages of LED include high energy efficiency, long life, wide range of colour, light weight, and small size. In the direct-lighting backlight module, high brightness and large viewing angle LED is suitable for large area liquid crystal display [1]. A shortcoming of LEDs is that only a small fraction of the light is available from the device due to total internal reflection in the substrates. There are two main approaches for improving LED efficiency: the first is increasing the internal quantum efficiency (η_i), which is determined by crystal quality and epitaxial layer structure, and the second is increasing light extraction efficiency ($\eta_{extraction}$). The internal quantum efficiency has been very close to their theoretical limits already. However, there is still much room for improving the extraction efficiency. Several methods have been reported to enhance the extraction efficiency, including the use of photonic crystal pattern [2], surface roughening [3], and microlens arrays (MLAs) [4]. Among these approaches, the process of MLAs is much simpler and more reliable. For microlenses which were much smaller than LED chip, the different arrangements of microlenses had the same improvement of luminous current efficiency of the LED when the fill factors were kept the same [6, 7]. However, if the lens diameter was comparable to the size of the LED chip, the radiation pattern shows peaks that correspond to the out-coupling of individual lenses, indicating that alignment of the lenses becomes important in this case [7]. There have been many techniques to fabricate MLAs, including thermal reflow, laser ablation, direct laser writing, ink-jet printing, gray-scale mask methods, micro-contact printing (μCP) of self-assembled mono layers (SAMs) and adhesive lithography [8-10]. However, most of these mentioned methods have the

drawbacks of high facility cost, time consumption, alignment inaccuracy, or high temperature process. Therefore, a fast, cost effective, stable, and focal length controllable method is desirable to fabricate MLAs.

SU-8 photoresist (MicroChem, MA) has high optical transmittance from visible to near-infrared wavelength and high refractive index (~1.63) [11]. Furthermore, it has better chemical resistance and mechanical strength than other common polymers such as polycarbonate or PMMA. As a result, SU-8 photoresist is ideal for microlens array fabrication [12]. In this work, a transparent and self-assembled MLA fabricated by the hydrophilic effect through ultra-violet (UV)/ozone treatment is presented. A base layer of SU-8 photoresist can be surface modified to become more hydrophilic using UV/ozone cleaner (model UV-1,Samco) [13]. The contact angle depends on the processing time, UV power and ozone concentration. This method provides a fast, low cost, no etch-transfer, no photo mask fabrication processes to make microlenses on LED chips. Polydimethylsiloxane (PDMS from Dow Corning, USA) is an elastomer which has good chemical stability and is available in a variety of useful forms as conformal coatings, encapsulants and adhesives. Reduction of the hydrophobicity can be also achieved by exposing PDMS to UV/ozone [14]. It was used to encapsulate the LED chips and the bonding wires. In the following sections, the fabrication process is described. The microlens on the LED chip not only enhanced the extraction efficiency but also increased the viewing angle.

4.2 The working mechanism

The SU-8 photoresist microlens was fabricated on a bared LED chip, which was pre-encapsulated by a layer of PDMS. The PDMS was used to protect the LED chip and the bonding wire. SU-8 is a well-known photoresist which has good mechanical

strength and UV curable property. The surface can be modified to be more hydrophilic by using UV/ozone treatment. It directly generate O−H on the phenol group, C=O and O−C=O hydrophilic functional groups on SU-8 photoresist surfaces, which contributes to the hydrophilic surface of SU-8 polymer. Diluted SU-8 contact angles on the modified surface are ranged from 27˚ to 15˚ depending on the processing time, UV power and ozone concentration. Figure 4-1 illustrates schematically the working principle of SU-8 photoresist MLA by the use of the hydrophilic effect through UV/ozone treatment. LED chips on silicon substrate were first encapsulated by PDMS, as in Figure 4-1(a). The PDMS surface was treated by UV/ozone in order to reduce the hydrophobicity. This made it easier to spin a layer of SU-8 base layer. A 10-μm thick SU-8 photoresist shadow mask with circular openings was used to define the UV/ozone treatment areas on the SU-8 photoresist base layer, as in Figure 4-1(b). The exposed zones became more hydrophilic than the obstructed zones after UV/ozone treatment, as in Figure 4-1(c). According to the surface modification, more treatment time results in more hydrophilic surfaces. In other words, a smaller contact angle was formed under longer UV/ozone treatment time. After the more hydrophilic zones were created and the SU-8 photoresist mask was removed, the substrate was dipped in and out of the diluted SU-8 photoresist solution with a slow and constant velocity (approximately 0.3 mm/sec), as in Figure 4-1(d). Finally, SU-8 photoresist MLA was formed on the substrate after applying the UV curing process, as in Figure 4-1(e).

The self-assembled technique utilizes the crosslink between SU-8 microlens and SU-8 base layer. It is very strong and not easy to be separated. The concentration of SU-8 photoresist must be diluted first to automatically stay on the areas with more hydrophilic property. Because of the evaporation of the solvent after UV curing process, the volume of the diluted SU-8 photoresist liquid microlens shrinks. Therefore, the

contact angle is smaller compared to the default and the footprint area is smaller than the shadow mask opening. In general, a higher surface energy of SU-8 base layer results in a larger footprint area. In the other words, longer UV/ozone treatment time and larger shadow mask opening results in higher surface energy, in which larger shadow mask makes UV/ozone treatment more efficiently. In these regards, the size and focal length can be manipulated by controlling the UV/ozone treatment time and shadow mask opening for this process. Once the microlens was designed, the thickness of PDMS was used to determine the distance between a microlens and the LED chip. The shorter distance induced the wider viewing angle.

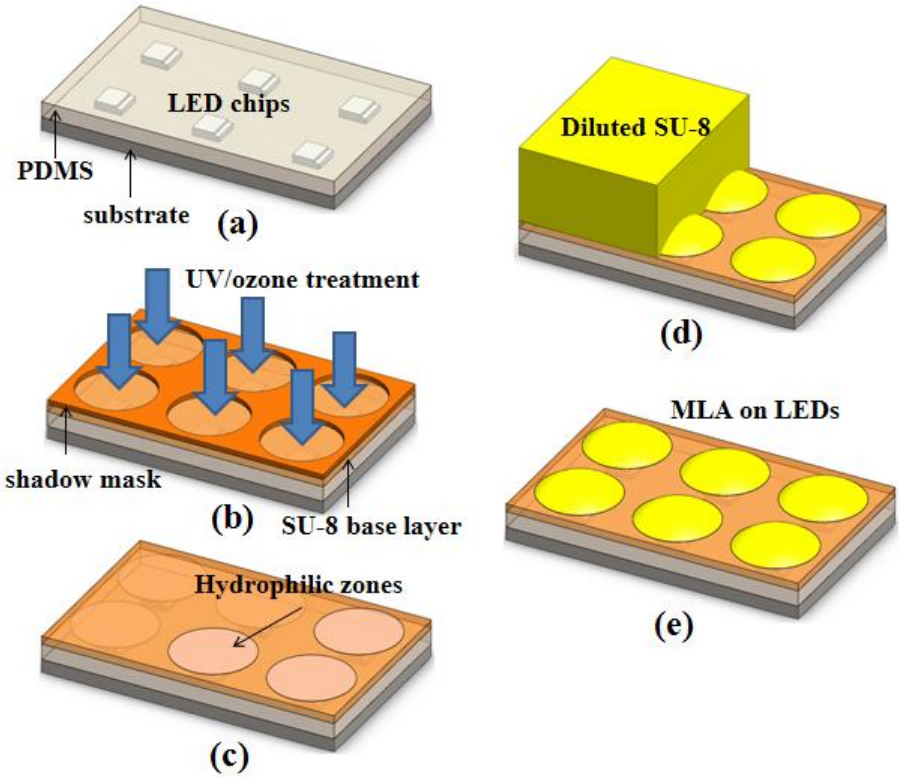

Figure 4-1 The schematic of the presented fabrication of the SU-8 MLA. (a) Encapsulating the LED chips by PDMS. (b) UV/ozone treatment through the shadow mask. (c) Removing the shadow mask. (d) Dipping out from the diluted SU-8 solution. (e) UV curing.

4.3 Fabrication process

In order to define the hydrophilic zones, we fabricated an SU-8 photoresist shadow mask at first. The SU-8 photoresist shadow mask has good mechanical strength and chemical resistance. Therefore, it is removable and reusable. It was fabricated by micromachining processes. At first, the SU-8 photoresist was spun on the glass substrate with the speed of 500 rpm for 5 sec and 1000 rpm for 30 sec. Then, it was soft baked at 95 ℃ for 3 min followed by 3.2 J/cm^2 exposures in the wavelength of 405 nm with optical masks of 200 μm diameter. The post exposure baking was 65 ℃ for 2 min and 95 ℃ for 1 min. The hard backing was 150 ℃ for 3 min. Finally, The SU-8 photoresist shadow mask with circular openings was released by isotropic etching in buffered oxide etcher (BOE). The thickness of the shadow mask was approximately 10 μm.

In this study, green LED chips (HWFR-P341, Philips Lumileds, USA) were fixed on a silicon wafer by UV resin. The wavelengths were from 515 to 535 nm. The max forward voltage was 3.8 V with 20 mA. A commercially available SU-8 3035 negative photoresist, a SU-8 2000 thinner, and a SU-8 developer were used (MicroChem Corp., MA, USA). For cleaning the substrate, a silicon wafer was first cleaned with acetone, isopropanol (IPA) and deionized (DI) water, and then dehydrated on a hot plate with a temperature of 100 ℃ for 10 min. Figure 4-2 shows schematic drawings of the fabrication process of the presented method. The detailed fabrication processes are described below.

4.4 LED encapsulation

The LED chips in Figure 4-2(a) were attached to a silicon wafer by using a layer of UV resin. It was cured by exposing to UV light radiation with 7.2 J/cm^2 at the

wavelength of 405 nm. Thereafter, the LED chips were bonded to copper taps by aluminum wire. In order to protect the LED chips and the bonding wires, a layer of PDMS on LED chips was performed by using molding method as shown in Figure 4-2(b). The thickness of PDMS encapsulant was approximately 500 μm.

4.4.1 SU-8 photoresist base layer

We employed the spin coating method (NMC-W-1102, Laurell Technologies Corp., USA) to coat SU-8 photoresist on the LED chips with the PDMS encapsulant. However, it was not easy to coat SU-8 photoresist on the hydrophobic PDMS surface. It had to be surface modified to reduce the hydrophobicity by 15-min UV/ozone treatment, as shown in Figure 4-2(c). The spin speed of coating SU-8 photoresist was 500 rpm for 5 sec and 4000 rpm for 30 sec. In order to produce a thinner SU-8 photoresist layer, the weight ratio was a 10:8 mixture of SU-8 3035 and SU-8 2000 thinner. Although the absorbance of SU-8 photoresist in visible wavelengths is relatively low, shorter optical propagation path induces lower absorbance. The baking process was skipped in order to control the process at room temperature. It was finally exposed to 9.6 J/cm^2 for UV curing. An SU-8 photoresist base layer with 5 μm thickness was formed, as shown in Figure 4-2(d).

4.4.2 UV/ozone treatment

The surface of SU-8 photoresist became more hydrophilic via UV/ozone treatment. It depends on the processing time, UV power and ozone concentration. The light source of UV/ozone cleaner (model UV-1,Samco) is 110 W with primary process wavelength of 254 and 182 nm. The oxygen flow rate is 0.5 L/min. In order to define the microlens footprint areas, the SU-8 photoresist shadow masks with 200 μm diameter opening was applied on the SU-8 photoresist base layer as shown in Figure 4-2(e). Then, UV/ozone

treatment was applied within three minutes on shadow masks as shown in Figure 4-2(e). After the UV/ozone treatment, the SU-8 photoresist shadow mask could be removed easily and stored for usage next time as shown in Figure 4-2(f). Therefore, the SU-8 photoresist base layer with circular zones which were more hydrophilic was formed as in Figure 4-2(f).

4.4.3 Dipping in and out of diluted SU-8 photoresist & UV curing

After the hydrophilic zones were created and the shadow mask was removed, the substrate was dipped in and out of the diluted SU-8 photoresist solution with a slow and constant velocity (approximately 0.3 mm/sec) as in Figure 4-2(g). The volume ratio of the diluted SU-8 photoresist solution was a 1: 6 mixture of SU-8 3035 with its thinner, SU-8 2000 thinner. The SU-8 photoresist should be diluted so that the viscosity was low enough to ensure separation of SU-8 solution on different zones on the SU-8 photoresist base layer due to surface energy difference. The MLA was created after taking out of the diluted SU-8 photoresist solution. Finally, the fabricated SU-8 photoresist MLA was then exposed to UV light radiation with 7.2 J/cm^2 at the wavelength of 405 nm, as in Figure 4-2(h), to be the final step in making cross-linked SU-8 MLA with high mechanical strength.

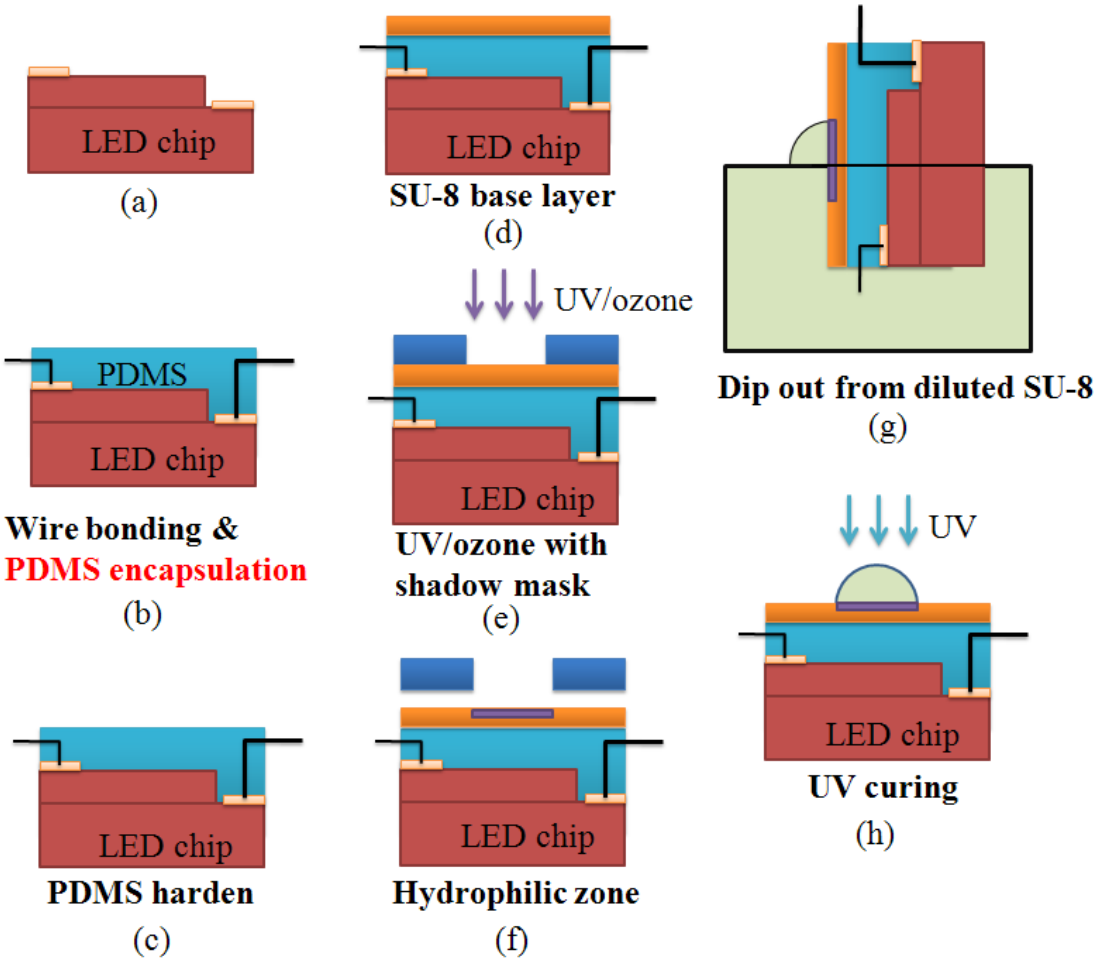

Figure 4-2 The fabrication process. (a) The bared LED chip. (b) Wire bonding and PDMS encapsulation. (c) PDMS hardening. (d) A layer of SU-8 base layer. (e) UV/ozone treatment through shadow mask. (f) Removing the shadow mask. (g) Dipping out from diluted SU-8 solution. (h) UV curing.

4.5 Optical System Simulation and experimental results

In this section, we first simulated the optical performance of a LED chip with a microlens in Figure 4-3 by using the commercial computer aid design software, ZEMAX® . The non-sequential mode in ZEMAX® was adapted. Figure 4-3 shows four layers including LED chip (n = 2.5), PDMS (n = 1.44) encapsulant, SU-8 (n = 1.63)

base layer, and SU-8 microlens. The lens diameter was 182 mm and the LED chip was 200 μm by 300 μm. The radius of curvature of the microlens was 1.83 mm. The detector plan (30 mm x 30 mm) was 30 mm away from the LED chip. A close-up drawing of the simulation model is also shown at the right hand side of Figure 4-3. The simulation results of optical illuminance are presented in Figure 4-4. The illumination pattern form a LED without a microlens was shown in Figure 4-4(a) and Figure 4-4(b) is the illumination patter after a microlens was placed on the LED chip. From the simulation result, it reveals that the peak luminance was approximately 15 % improved.

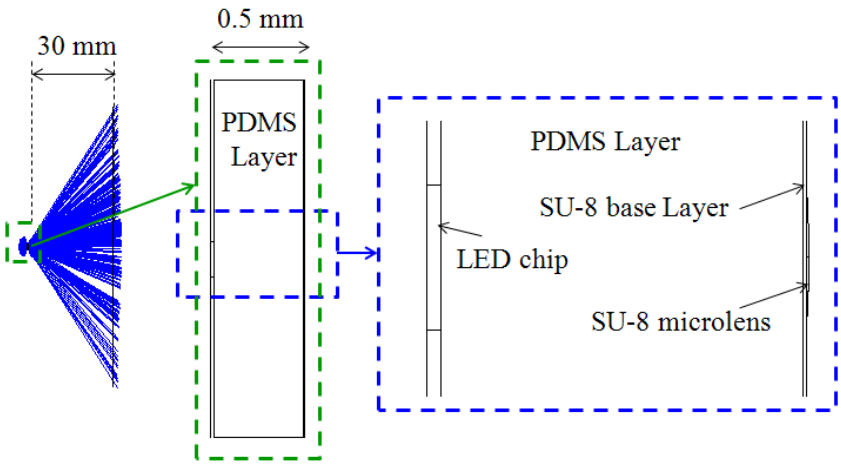

Figure 4-3 The optical system of microlens on LED.

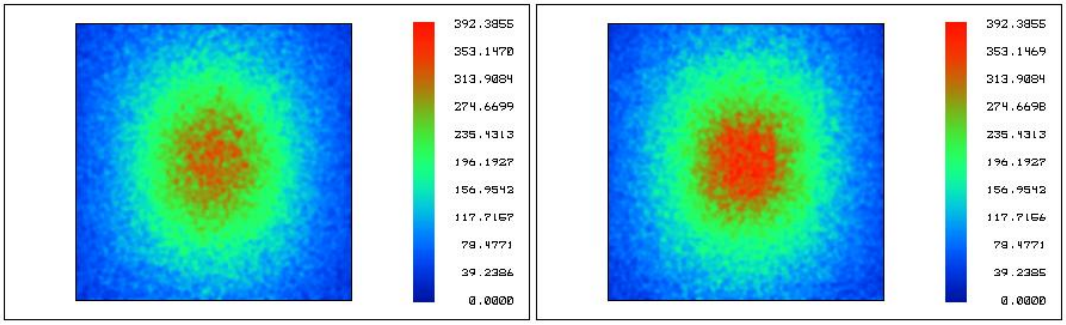

Figure 4-4 The simulation result of luminance map (30 mm x 30 mm). (a) Without microlens (b) With microlens.

As described above, the contact angle became smaller with longer UV/ozone treatment time. Figure 4-5(a) shows the experimental result of contact angles of diluted SU-8 photoresist with zero, one, two, three, and four minutes UV/ozone treatment time on an SU-8 photoresist base layer before UV curing. The measurement system was based on the Sessile Drop Method, which was set up by a uniform backlight, a digital camera (R10, Ricoh, Japan), and the software programmed by LabVIEW® , as shown in Figure 4-5(b). The program detected the two endpoints of the footprint and the spherical centroid of the profile of droplet, where the profile was assumed to be spherical because the drop was small so that the gravity can be neglected. Thereafter, the contact angle was derived by the three points. From the result, the contact angles reached its minimum value when UV/ozone treatment time was longer than three minute. The scanning electron microscope (SEM) photograph is shown in Figure 4-6. It shows that the 200-μm diameter MLA with three minutes UV/ozone treatment time was fabricated successfully on the PDMS encapsulant. Figure 4-6(b) indicates the layers of SU-8 microlens, SU-8 base layer, and PDMS encapsulant. The thickness of the PDMS and the SU-8 base layer were approximately 500 μm and 10 μm, respectively.

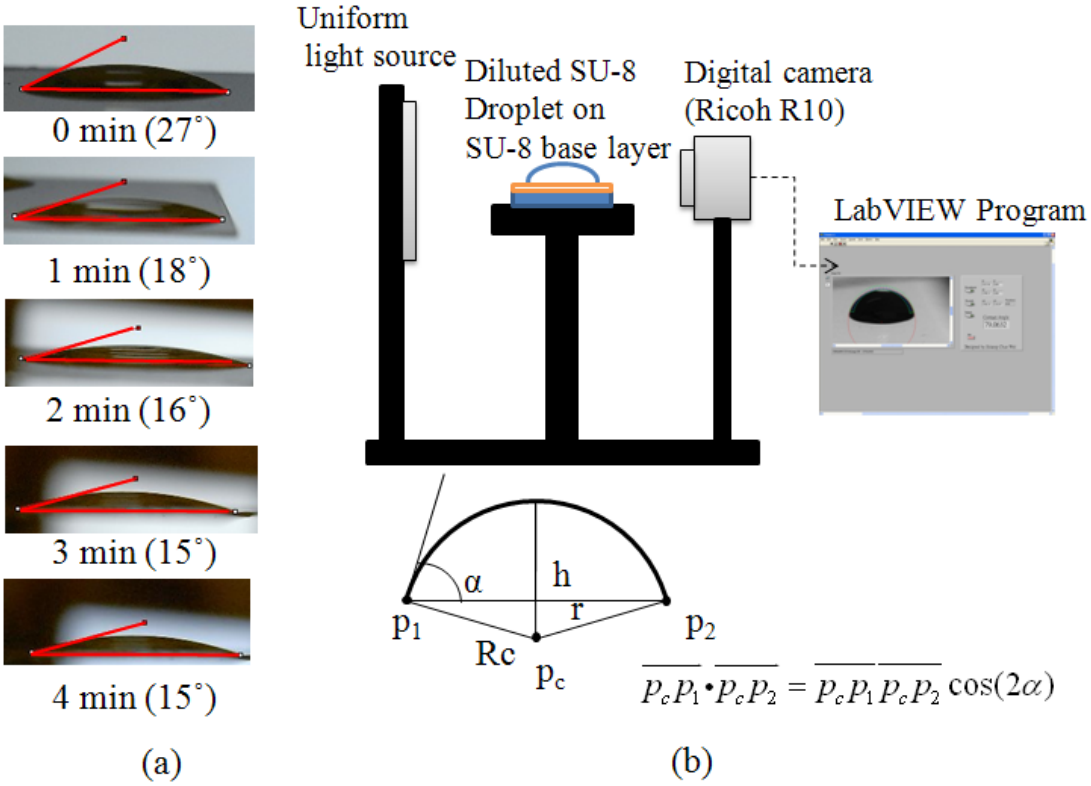

Figure 4-5 (a) The experimental results of contact angles between a non-UV-exposed diluted SU-8 photoresist droplet and an SU-8 photoresist base layer. (b) The experiment setup of Sessile Drop method.

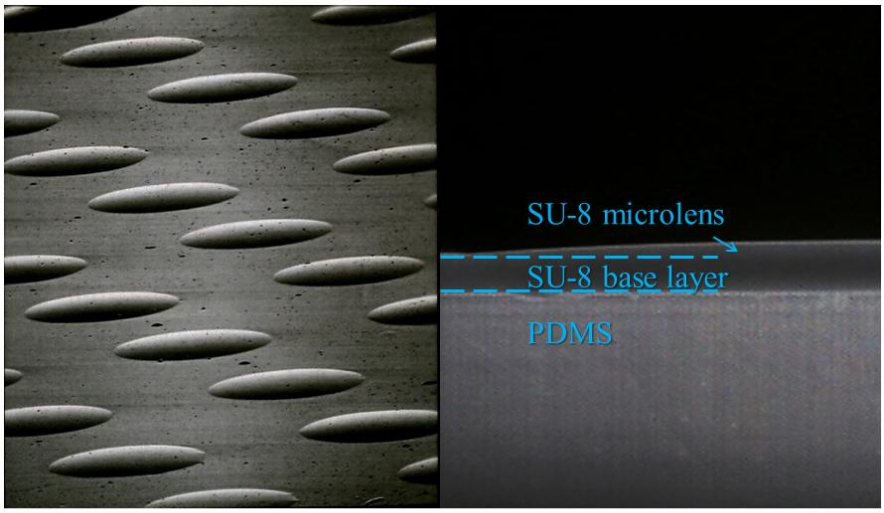

(a) (b)

Figure 4-6 (a) The SEM photograph of 200-μm diameter MLA under three minutes UV/ozone treatment time. (b) The cross section profile of an SU-8 microlens.

Two dimensional profile of MLA which was measured by surface profiler (Alpha Step 500, TENCOR) showed that the lenses had good surface smoothness. The surface roughness was less than 70 nm. This is a typical value for microlenses without going through etching process. Meanwhile, the footprint diameter and the sag height of the microlens were 182 μm and 3.04 μm. Thereafter, the corresponding focal length and contact angle were 2.16 mm and 3.82 degree by using the following equations, assuming the microlens spherical.

$$f = \frac{r^2 + h^2}{2h(n-1)} \tag{1.1}$$

$$\alpha = \tan^{-1}\left(\frac{2hr}{r^2 - h^2}\right) \tag{1.2}$$

,where f is the focal length, r is the footprint radius, h is the sag height, and the α is the contact angle. The measured footprint diameter and the calculated contact angle were smaller than the diluted SU-8 droplet. It was resulted from the shrinkage of SU-8

photoresist after UV curing.

We have fabricated microlens direct on the top of LED chip successfully by using this method. The opening of the shadow mask was 200 μm and the UV/ozone treatment time was three minutes. The size of LED chip was approximately 200 μm and 300 μm. Figure 4-7 (a) and (b) shows the optical microscopy (ECLIPSE 50i with 50X objective, Nikon, Japan) image of the fabrication result of the microlens on a LED chip. It was captured by a CCD camera (CoolPix4500, Nikon, Japan). Because of a high NA (= 0.8) objective lens, the depth of focus (DOF) of a microscopy is very small (~0.6 μm). Figure 4-7(a) is a LED chip with aluminium wire bonding. Figure 4-7(b) is a microlens on the LED chip. Figure 4-7(c) shows the stereo microscopy (PS-130a, Potop, Taiwan) image of the microlens on the LED. It shows both clear image on LED chip and microlens. Figure 4-7(d) shows the tilt view of the stereo microscopy image.

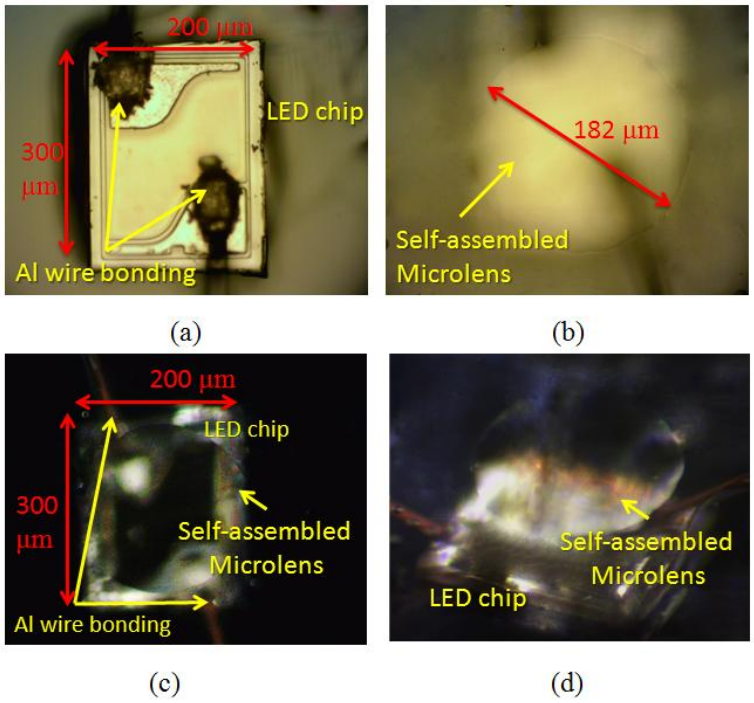

Figure 4-7 The optical microscope image of fabrication result. (a) The LED chip with aluminum (Al) wire bonding. (b) The 200-μm diameter microlens on LED. (c) The clear stereo microscope image on both LED chip and microlens. (d) The tile view of the stereo microscope image of the microlens on LED.

In order to measure the angular light field distribution, we setup a measurement system as shown in Figure 4-8. It included a computer, a step-motor controller (DS102, Suruga, Japan), a motorized rotation stage (KS101, Suruga, Japan), a current meter (Kathley 2400, USA), a power supply, and a photo detector. We measured the light field distribution from -90 degree to +90 degree, where zero degree stood for the normal direction, with a step of one degree, as shown in Figure 4-9. The intensity was normalized by the maximum value of the LED with microlens on it. From the result in Figure 4-9, the out coupling of LED was approximately 15% and 28% improved in maximum and total accordingly, and the viewing angle was 17 degree increased (half of

the maximum intensity). Figure 4-10 shows the illumination map. It reveals that the luminance was improved as well.

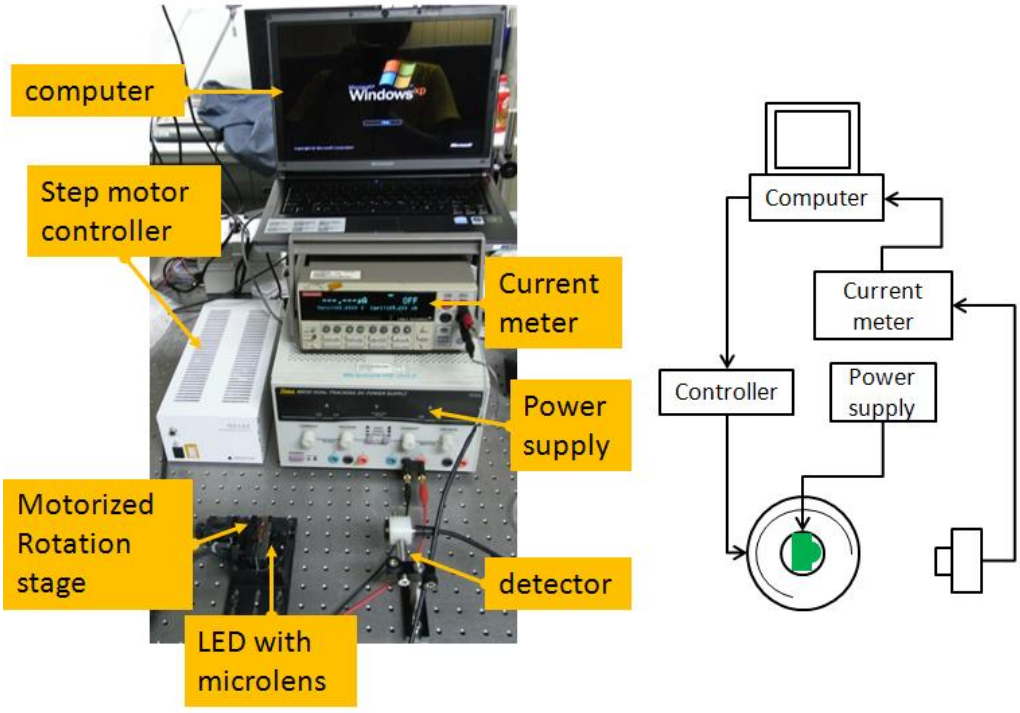

Figure 4-8 The measurement setup of the angular light field distribution.

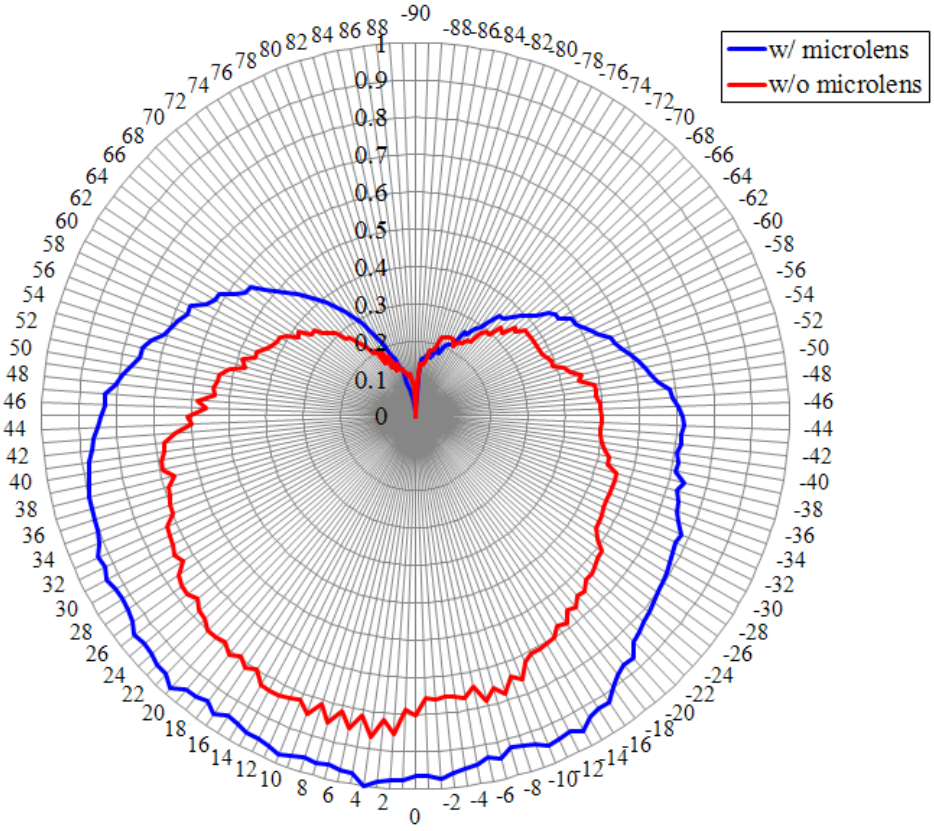

Figure 4-9 The normalized angular distribution of light intensity (from -90 to 90 degree). It improved the extraction efficiency of 15 % and 28% in maximum and total accordingly, and increased the viewing angle of 17 degree ($\theta_{1/2}$).

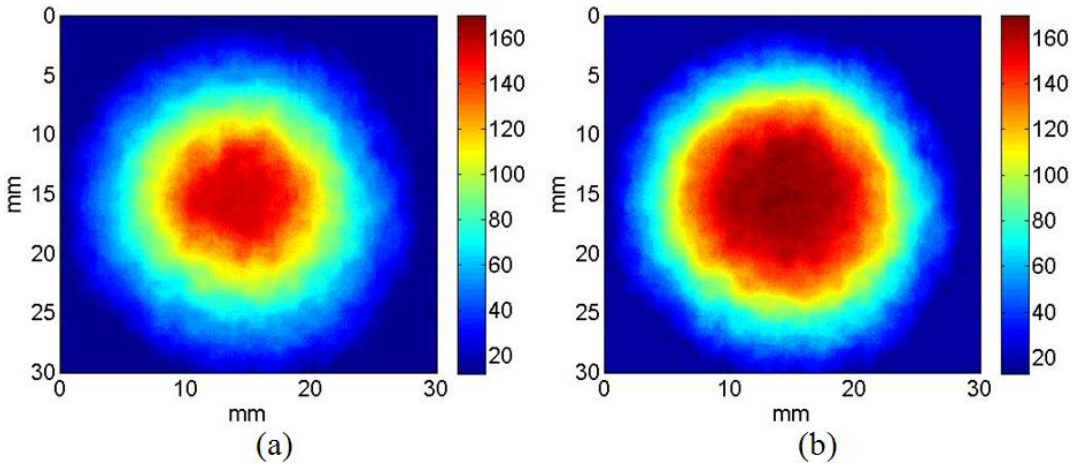

Figure 4-10 The experimental illumination map. (a) Without microlens and (b) With microlens.

4.6 Conclusions

A transparent and self-assembled microlens on the top of LED fabricated by using hydrophilic effect under UV/ozone treatment was presented. This method provides a fast, low cost, no etch-transfer, no photo lithography fabrication processes. MLA by the use of a shadow mask of 200 μm diameter for three minutes UV/ozone treatment time has been fabricated successfully. The LED chips were encapsulated by a layer of thick PDMS (n = 1.44) and the MLA was made of negative photoresist SU-8 (n=1.63). The high refractive index material of PDMS and SU-8 photoresist and the microlens on the top of LED improved the extraction efficiency of 15 % and 28% in maximum and total accordingly, and increased the viewing angle of 17 degree.

References

[1] W.-C. Chen, T.-T. Lai, M.-W. Wang, and H.-W. Hung, "An optimization system for LED lens design," *Expert Systems with Applications*, vol. 38, pp. 11976-11983, 2011.

[2] A. Bateni, S. Laughton, H. Tavana, S. Susnar, A. Amirfazli, and A. Neumann, "Effect of electric fields on contact angle and surface tension of drops," *Journal of colloid and interface science*, vol. 283, pp. 215-222, 2005.

[3] S. M. Kuo and C. H. Lin, "Fabrication of aspherical SU-8 microlens array utilizing novel stamping process and electro-static pulling method," *Optics Express*, vol. 18, pp. 19114-19119, 2010.

[4] Z. Zhan, K. Wang, H. Yao, and Z. Cao, "Fabrication and characterization of aspherical lens manipulated by electrostatic field," *Applied Optics*, vol. 48, pp. 4375-4380, 2009.

[5] J. H. Karp, E. Tremblay, J. M. Hallas, and J. E. Ford, "Orthogonal and secondary concentration in planar micro-optic solar collectors," *Optics Express*, vol. 19, pp. A673-A685, 2011.

[6] K. Y. Chen, H. Y. Lin, M. K. Wei, J. H. Lee, Y. T. Hsiao, C. C. Lin, Y. H. Ho, and J. H. Tsai, "Enhancement and Saturation Phenomena on Luminous Current and Power Efficiencies of Organic Light-Emitting Devices by Attaching Microlens Array Films," *Journal of display technology*, vol. 7, pp. 242-249, 2011.

[7] S. Moller and S. Forrest, "Improved light out-coupling in organic light emitting diodes employing ordered microlens arrays," *Journal of applied physics*, vol. 91, p. 3324, 2002.

[8] H. A. Biebuyck and G. M. Whitesides, "Self-organization of organic liquids on

patterned self-assembled monolayers of alkanethiolates on gold," *Langmuir,* vol. 10, pp. 2790-2793, 1994.

[9] D. M. Hartmann, O. Kibar, and S. G. Esener, "Characterization of a polymer microlens fabricated by use of the hydrophobic effect," *Optics Letters,* vol. 25, pp. 975-977, 2000.

[10] H. Ottevaere, R. Cox, H. P. Herzig, T. Miyashita, K. Naessens, M. Taghizadeh, R. Völkel, H. Woo, and H. Thienpont, "Comparing glass and plastic refractive microlenses fabricated with different technologies," *Journal of Optics A: Pure and Applied Optics,* vol. 8, p. S407, 2006.

[11] O. P. Parida and N. Bhat, "Characterization of optical properties of SU-8 and fabrication of optical components," in *Int. Conf. on Optics and Photonics*, CSIO, Chandigarh, India, 2009.

[12] S.-M. Kuo and C.-H. Lin, "Fabrication of aspherical SU-8 microlens array utilizing novel stamping process and electro-static pulling method," *Opt. Express,* vol. 18, pp. 19114-19119, 2010.

[13] C.-J. Chang, C.-S. Yang, L.-H. Lan, P.-C. Wang, and F.-G. Tseng, "Fabrication of a SU-8-based polymer-enclosed channel with a penetrating UV/ozone-modified interior surface for electrokinetic separation of proteins," *Journal of Micromechanics and Microengineering*, vol. 20, 2010.

[14] H. Hillborg, N. Tomczak, A. Olah, H. Schonherr, and G. J. Vancso, "Nanoscale hydrophobic recovery: a chemical force microscopy study of UV/ozone-treated cross-linked poly (dimethylsiloxane)," *Langmuir,* vol. 20, pp. 785-794, 2004.

Chapter 5 An Optical Wavefront Sensor Based on a Double Layer Microlens Array

In order to determine light aberrations, Shack-Hartmann optical wavefront sensors make use of microlens arrays (MLA) to divide the incident light into small parts and focus them onto image planes. In this work, we present the design and fabrication of long focal length MLA with various shapes and arrangements based on a double layer structure for optical wavefront sensing applications. A longer focal length MLA could provide high sensitivity in determining the average slope across each microlens under a given wavefront, and spatial resolution of a wavefront sensor is increased by numbers of microlenses across a detector. In order to extend focal length, we used polydimethysiloxane (PDMS) above MLA on a glass substrate. Because of small refractive index difference between PDMS and MLA interface (UV-resin), the incident light is less refracted and focused in further distance. Other specific focal lengths could also be realized by modifying the refractive index difference without changing the MLA size. Thus, the wavefront sensor could be improved with better sensitivity and higher spatial resolution.

In this chapter, Vinna Lin was the one who has the primary contribution including the fabrication and discussion of double layer microlens array and the comparison between commercial SHWS and ours. I was the coauthor with the contribution to the part of wavefront sensor computing algorithm programing and the wavefront reconstruction. Most contents were adopted from the published paper in Sensors with some revisions. Section 5.1 to section 5.5 are materials from Vinna's work [1]. Figure 5-3, -4, -5(a), -6, -7, -8 are from Vinna's work. Table 5-1 to 5-3 are also from Vinna's work.

5.1 Introduction

An optical wavefront sensor is an important device in determining wavefront aberration if fields ranging from the astronomy to any optical testing application. There are several types of wavefront sensors including the Michelson interferometer, Shearing interferometer, Fizeau interferometer, and even the Foucault knife-edge test. Among these interferometric methods, the Shack-Hartmann wavefront sensor (SHWS) is the most popular sensor because of its simplicity and elegance for measuring the shape of a wavefront. It has been applied to adaptive optics for high-energy lasers and astronomy for many years [2]. The main goal is to improve image quality taken by ground-based telescopes which might be distorted by atmospheric turbulence. However, as the technology has been developed, the technique has been implemented in many other fields. Over time, applications in quality laser beam measurement, optics testing, and optical system calibration and alignment have been discussed. Furthermore, this technology quickly led to the evolution of more sophisticated sensors focused around ophthalmic applications [3], CCD cameras, and micro-optics. The applications of SHWS have become widespread throughout the World, with hundreds of millions of astronomical images benefiting from the process to millions of corrective surgeries that will be performed in upcoming years to enhance vision. It is amazing for a technology to have such a dramatic impact and evolution from a single field to multiple fields as the SHWS has.

The most critical element of an SHWS is its microlens array (MLA). The incident light is divided into a number of small samples by the lenslet arrays, which then are focused onto a detector array. These focal spots of light are the key principle in the measurement of wavefront aberration. The wavefront slopes are computed by the

displacement of the measured focal spots from their reference spot positions. In this work, we first propose a design and method for extending the focal length of MLA effectively based on double layer structure; the evaluation of the MLA is presented accordingly. Furthermore, we integrated the MLA with an image sensor to build a SHWS. Not only the development of the SHWS is discussed but also the experimental results of the SHWS performance is explained by comparing the measured wavefront with the commercial one. The experimental results of the system are discussed and compared between the long focal length, the shorter focal length and the commercial SHWS.

5.2 Design of Double Layer Microlens Array

In a thermal reflow process, microlenses are made by heating photoresist cylinders. The focal length (*f*) of MLA could be described as in Equation (1.3) [4]:

$$f = \frac{r_c}{n-1}$$
$$r_c = \frac{h^2 + r^2}{2h} \tag{1.3}$$

where n is the refractive index of MLA material, r_c is radius of curvature, which is related to the height, h and radius, r of melted MLA [5], the lens profile is assumed to be a spherical shape here. However, only some profiles are possible. If the ratio of height to diameter is too low, photoresist cylinders only reflow at the edge of itself. In other words, photoresist cylinders would not become microlens arrays. The ratio of lens height to diameter should not be too small. Although increasing diameter does increase maximum focal length, the thickness of the photoresist also needs to be increased. A thick photoresist is hard coat uniformly and multi-coatings increase the complexity of the process, so there is a trade-off between a long focal length and photoresist thickness.

Therefore, we propose a new design to extend the focal length based on the calculations that follow.

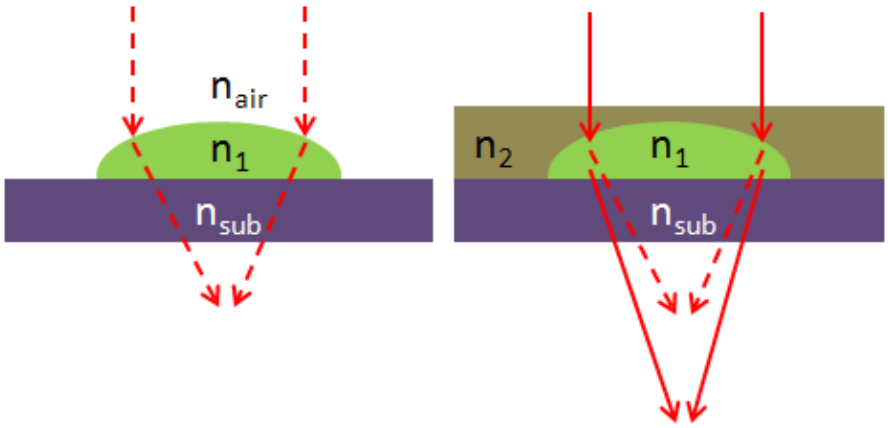

Figure 5-1 Light propagation in a microlens by (a) traditional thermal method (dashed lines) and (b) our new method (solid lines).

Figure 5-1 shows the schematic drawing of our new design. An additional cover layer is applied on the top of MLA. The light is less refracted at the MLA surface as shown in Figure 5-1(b) and this results in the extension of the focal length. The new MLA design consists of a plano-concave lens and a following plano-convex lens. The total focal length is described by Equation (1.4) [6]:

$$\frac{1}{f} = \frac{1}{f_1} + \frac{1}{f_2} - \frac{d}{f_1 \cdot f_2} \tag{1.4}$$

Parameter d is the separate distance, which is zero in our case. Substituting Equation (1.3) into f_1 and f_2, we can get the effective focal length as in Equation(1.5). Notice the focal length of cover layer or plano-concave lens is negative.

$$f_{eff} = \left(\left(\frac{r_c}{n_1 - 1} \right)^{-1} + \left(\frac{-r_c}{n_2 - 1} \right)^{-1} \right)^{-1} = \frac{r_c}{n_1 - n_2} \tag{1.5}$$

Comparing focal length in Equations (1.3) and (1.5), the denominator is reduced from $(n_1 - 1)$ to $(n_1 - n_2)$. The extending factor of focal length is determined by the ratio of $(n_1 - 1)$ over $(n_1 - n_2)$. We adopt UV-resin (n = 1.4887) as our lens material and PDMS (n = 1.41) as our cover layer material. The focal length increased after a cover layer was added. Based on the calculations, the focal length of 235 μm diameter MLA is expected to be extended from 0.85 mm to 5.27 mm, which is six times longer than original one.

5.3 Fabrication Processes and Results

The long-focal-length MLA was made of polymer materials. We fabricated an opaque photoresist MLA first and transferred it into a transparency MLA with a cover layer. The fabrication steps are illustrated in Figure 5-2. In photoresist MLA fabrication, the silicon wafer was cleaned by piranha (H_2O_2 + H_2SO_4) solution and dehydrated by baking at 120 ℃ for 10 minutes. Then, we spun a layer of photoresist (AZ-P4620) at 1,000 rpm for 60 seconds on the silicon substrate, which resulted in a 13 μm thick photoresist. The photoresist cylinders were patterned after photolithography as seen in Figure 5-2(a). After heating at 160 ℃ for 10 hours, photoresist cylinders formed MLA with a spherical profile as seen in Figure 5-2(b). The next step was the transfer process, which replicated photoresist MLA to a new MLA made of UV-resin. As shown in Figure 5-2(c), we poured liquid polydimethysiloxane (PDMS, 184 from Dow Corning) on photoresist MLA followed by a low-speed spin of 100 rpm to reduce the thickness. After spin coating, the PDMS replicated the surface profile of MLA (e.g., PDMS was conjugated to the MLA surface). The PDMS coated wafer was relaxed for 10 minutes to reduce roughness. Once the top of liquid PDMS became flat after standing for 10 minutes, it was heated and cured at 65 ℃ for four hours. After cooling to room temperature, the PDMS mold was removed from the photoresist MLA. Because of low

surface free energy and elasticity of PDMS [8], it could be released from MLA easily without anti-stiction issue. Figure 5-2(d) shows a negative or concave master mold after releasing. Then, a drop of UV-resin (GA-126) was put on a PDMS mold and the mold was attached to a cover glass as shown in Figure 5-2(e). The UV-resin liquid went outward and filled the whole MLA area. We did this step carefully on a flat optical table without any air bubbles between the PDMS mold and a cover glass. This makes sure only a thin UV-resin layer was left. After UV curing, long-focal-length microlens arrays were fabricated on a cover glass as shown in Figure 5-2(f).

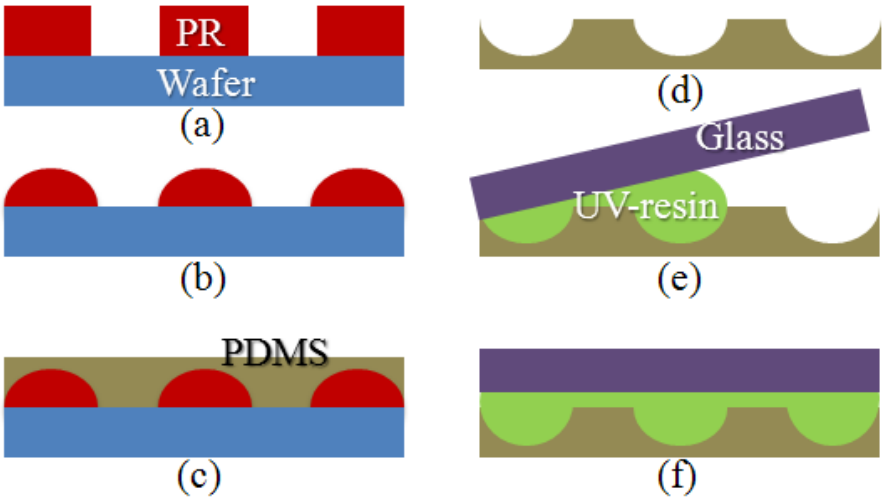

Figure 5-2 Fabrication steps of long-focal length MLA. (a)PR cylinders (b)Thermal reflow (c)PDMS molding (d)Release PDMS mold (e)Drop UV-resin & attach glass(f)UV curing.

錯誤! 找不到參照來源。 is the scanning electron microscope (SEM) image of the UV-resin MLA without and with the covering layer of PDMS. There are three layers shown in **錯誤! 找不到參照來源。**(b) from bottom to top: a glass substrate, UV-resin, and PDMS film as the flip structure in Figure 5-2(f). In addition, the UV-resin layer could also be replaced by other polymers such as SU-8 photoresist with different

refractive index. The resulting focal length was then determined by the refractive index difference. In this fabrication, the refractive index n_1 of UV resin (microlens layer) was 1.4887 and the refractive index n_2 of PDMS (covering layer) was 1.41. We measured the focal spot experimentally by moving the optical microscope up and down. The distance between the light-focusing point and vertex of the microlens was approximately 5.25 mm for a 235 μm diameter microlens and 2 mm for a 135 μm diameter microlens. Because of its high NA objective lens, the depth of focus (DOF) of a microscope is very small (~0.7 μm). The accuracy of the image plane position is around ±0.7 μm. The focused spot patterns and their intensity distribution are shown in Figure 5-4. The spot was measured under a microscope (ECLIPSE 50i with 50 × objective, Nikon) with bottom emitting light source. The spot profiles were symmetric, which means that each UV lens in the MLAs has good quality. In other words, the fabricated microlenses are symmetric. The profile of our microlenses is close to a sphere near the vertex and the side part of the microlenses is differs slightly from a spherical curve.

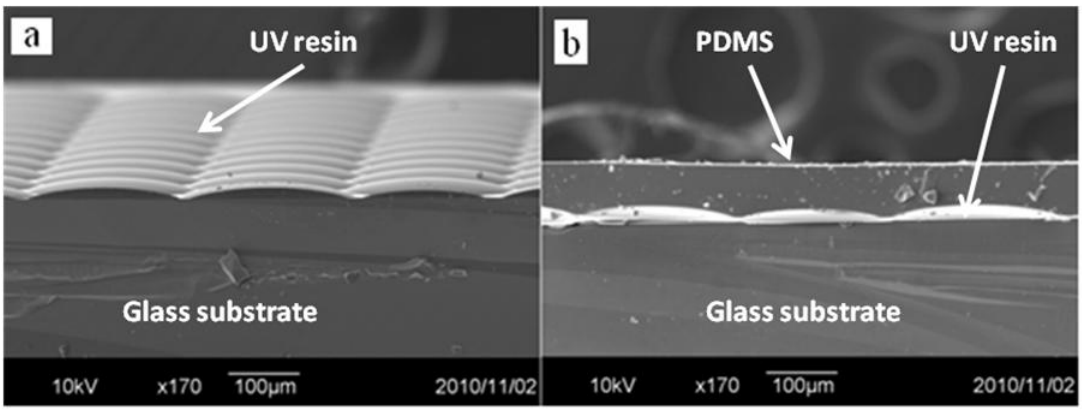

Figure 5-3 SEM image of the UV-resin MLA (a) without and (b) with the second layer of PDMS.

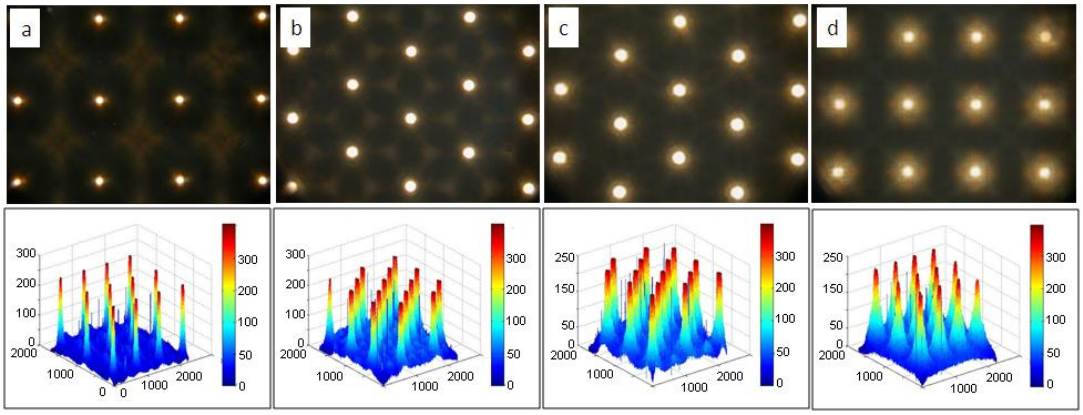

Figure 5-4 The focused spot images (above) and their intensity distribution (below) of **(a)** circular lens quadratic grid MLA, **(b)** circular lens hexagonal grid MLA, **(c)** hexagonal lens MLA, and **(d)** square lens MLA.

The fill factor of MLAs is related to the arrangement and gap of each lens as shown in Table 5-1. It shows that a square lens and a hexagonal lens have the same fill factor and a circular lens with a square arrangement has the lowest fill factor. The gap between each lens in our experiment was 20 μm. The fill factor could be increased by decreasing the gap distance of each lens.

Table 5-1 Lens arrangement versus fill factor for 20 μm of lens gap.

Lens Arrangement	**Lens Area (mm^2)**	**Total Area (mm^2)**	**Fill Factor**
Circular lens quadratic grid (d = 135 μm)	0.0143	0.0240	59.58%
Circular lens hexagonal grid (d = 235 μm)	0.0434	0.0563	77.09%
Hexagonal lens (d = 235 μm)	0.0478	0.0563	84.9%
Square lens (d = 235 μm)	0.0552	0.0650	84.9%

Finally, we show the comparison of methods which could increase the focal length by modifying different variables in Table 5-2. Unlike other methods that increase the focal length slightly (~1X), the method in this work produces a significant increment (~6X) in the focal length. Although two material layers are required, the second PDMS coating process is easy and could be done at room temperature. The room temperature curable properties of PDMS prevent any temperature variation during the processes, which minimizes the residual stress due to coefficient of thermal expansion (CTE) mismatch. Besides, the cured PDMS has good chemical stability. It also provides a passivation layer, which protects the inner microlens material from water absorption or chemical attack. In addition, the flat MLA surface is easier to clean than an uneven surface (e.g., the original single layer MLA without a passivation layer).

Table 5-2 Methods for increasing the focal length of MLA.

Methods	Advantage	Disadvantage
Refractive index difference	Significant increment (6X longer)	Double layer (2nd PDMS coating is easy)
Increase refractive index, n	Single layer process	Slightly (~1X, Depends on material property)
Increase diameter	Single layer process	Results in thick photoresist and spin coating problems

5.4 Wavefront Sensor Computing Algorithm and Measurement Results

The Shack-Hartmann wavefront sensor utilizes a microlens array to divide and reconstruct the incident wavefront. The incident light is divided into a number of beamlets by the two-dimensional microlens array [9]. The spot displacement which is related to the wavefront slope could be calculated by comparing the reference focal

spots and the measured wavefront focal spots provided by each lenslet. Each local wavefront slope corresponds to a wavefront distortion. The relationship between incoming wavefront slope θ, spot displacement Δd, and focal length of the lenslet f can be described by Equation (1.6) [7]:

$$\theta = \frac{\Delta d}{f} \tag{1.6}$$

There are various methods for reconstructing the wavefront from the slope measurements. We chose modal reconstruction in our calculation. The wavefront is described in terms of functions that have analytic derivatives in the modal reconstruction method. The measured slope data was then fit to the derivative of these functions, allowing a direct determination of the wavefront from the fitting coefficients. Therefore, it is desirable to expand the wavefront aberration in terms of a complete set of basis functions that are orthogonal, such as Zernike polynomials $Z_k(x,y)$ [10]:

$$w(x,y) = \sum_{k=1}^{+\infty} \omega_k Z_k(x,y) \tag{1.7}$$

where ω_k represents the Zernike coefficient. So we can write the local wavefront slopes as in Equation (1.8):

$$\begin{pmatrix} \partial w/\partial x \\ \partial w/\partial y \end{pmatrix}_m = \begin{pmatrix} \sum_{k=1}^{+\infty} \omega_k \frac{\partial Z_k}{\partial x} \\ \sum_{k=1}^{+\infty} \omega_k \frac{\partial Z_k}{\partial y} \end{pmatrix} \tag{1.8}$$

We can rewrite Equations (1.6) and (1.8) as following matrix:

$$\begin{bmatrix} \theta_x(1) \\ \cdots \\ \theta_x(p) \\ \theta_y(1) \\ \cdots \\ \theta_y(p) \end{bmatrix} = \begin{bmatrix} g_1(1) & \cdots & g_k(1) \\ \cdots & \cdots & \cdots \\ g_1(p) & \cdots & g_k(p) \\ h_1(1) & \cdots & h_k(1) \\ \cdots & \cdots & \cdots \\ h_1(p) & \cdots & h_k(p) \end{bmatrix} \begin{bmatrix} \omega_1 \\ \cdots \\ \omega_k \end{bmatrix} \tag{1.9}$$

where p is the number of centroid positions in this calculation. Therefore, we can calculate the unknown Zernike coefficient, ω_k by the inverse and the transpose of above matrix. By the matrix operation, we could get each of the corresponding Zernike polynomial wavefront aberration coefficients and take them into Equation (1.7). The working principle of the Shack-Hartmann wavefront sensor included the recognition of the aperture size/lens focal length, the detection of the image spots for reference beam and distorted beam, the calculation of the spot center and the displacement, the calculation of the Zernike coefficients from the wavefront, and the reconstruction of wavefront.

In order to measure the wavefront aberration, we integrated our fabricated MLA with an image sensor to construct a Shack-Hartmann wavefront sensor. We show the whole experiment setup in Figure 5-5. The laser light source from optical fiber is collimated by an aspherical lens screwed in front of the fiber connector. The collimated laser produces a reference wavefront which passes through our microlens array and results in separated focal spots on the detector. In this set up, we chose our fabricated hexagonal shaped MLA to focus the light on sensor because it not only has a higher fill factor, but also higher reconstruction precision.

To evaluate our SHWS performance, testing samples such as PAL (progressive addition lens) and PCX (plano-convex lens) was measured by our wavefront sensor. The test samples could produce wavefront aberrations when they are placed between the

laser light source and the SHWS.

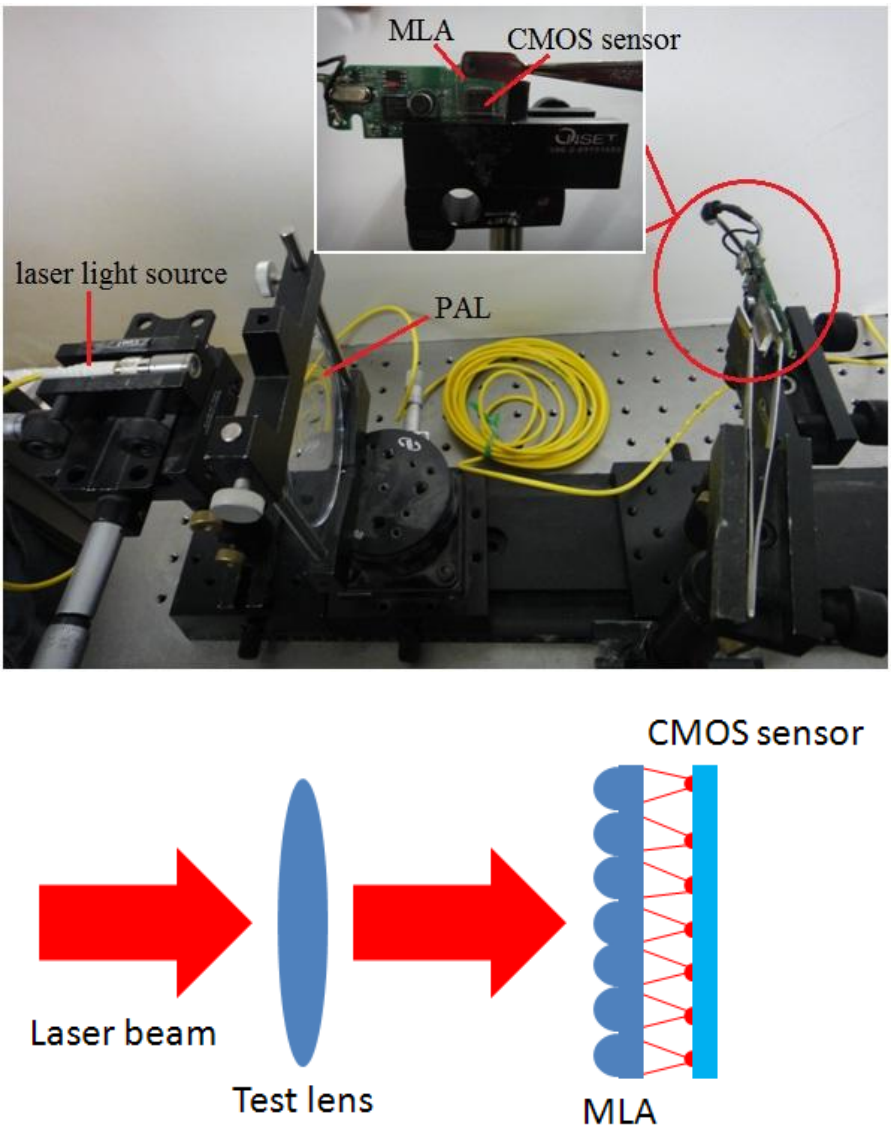

Figure 5-5 (a)The experiment setup for measuring a wavefront aberration of testing lens (PAL) by using our fabricated MLA and SHWS. (b) The schematic diagram.

For the measurement, we first took pictures of focal spots without aberration from the test samples as the reference points, as shown in Figure 5-6(a), and then a second picture of focal spots with aberration by putting the test lens between the laser light source and our SHWS, as shown in Figure 5-6(b). In order to calculate the centroid

spots precisely, a hexagon mask is defined to cover only one point in every calculation. We calculated 37 wavefront slopes of focal spots taken by the CMOS (complementary metal–oxide–semiconductor) image sensor. Therefore, our system was computed by four orders of Zernike coefficients with 10 aberration terms and each centroid position was calculated by the Labview® program. The comparison between the reference focal spots and the aberrated focal spots was shown in Figure 5-6(c), two previous pictures stacking, where red rectangles are the detected reference spots position and green rectangles were the detected aberrated spots position. The displacement was then calculated with the equations listed above.

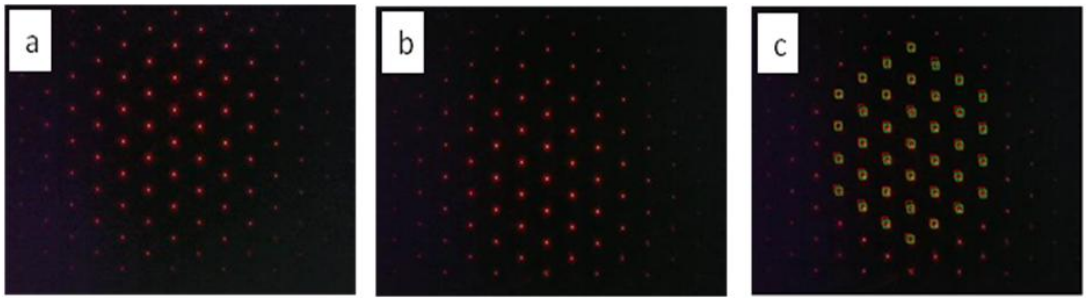

Figure 5-6 (a) Focal spots image of the reference wavefront, (b) focal spots image of the aberrated wavefront, and (c) detection picture of image spots for reference beam and distorted beams.

The wavefront aberration generated by the testing lens was measured by both our SHWS and a commercial wavefront sensor from OKO Tech (UI2210-m, UEye, NL). The lenslet array in the commercial wavefront sensor is in hexagonal configuration and the pitch size is 300 μm. To evaluate the performance of double layer microlens arrays, we compared the measurement result between our SHWS and the commercial one. First, we examined the PAL which is used to compensate the presbyopia. SHWS is used to observe the change of planar wavefront caused by lenses. Second, we observed the

aberration caused by titled incidence wavefront through PCX where rays pass through the lens at an angle to the axis θ. Figure 5-7 shows the measurement results by a three-dimensional phase map and its contour.

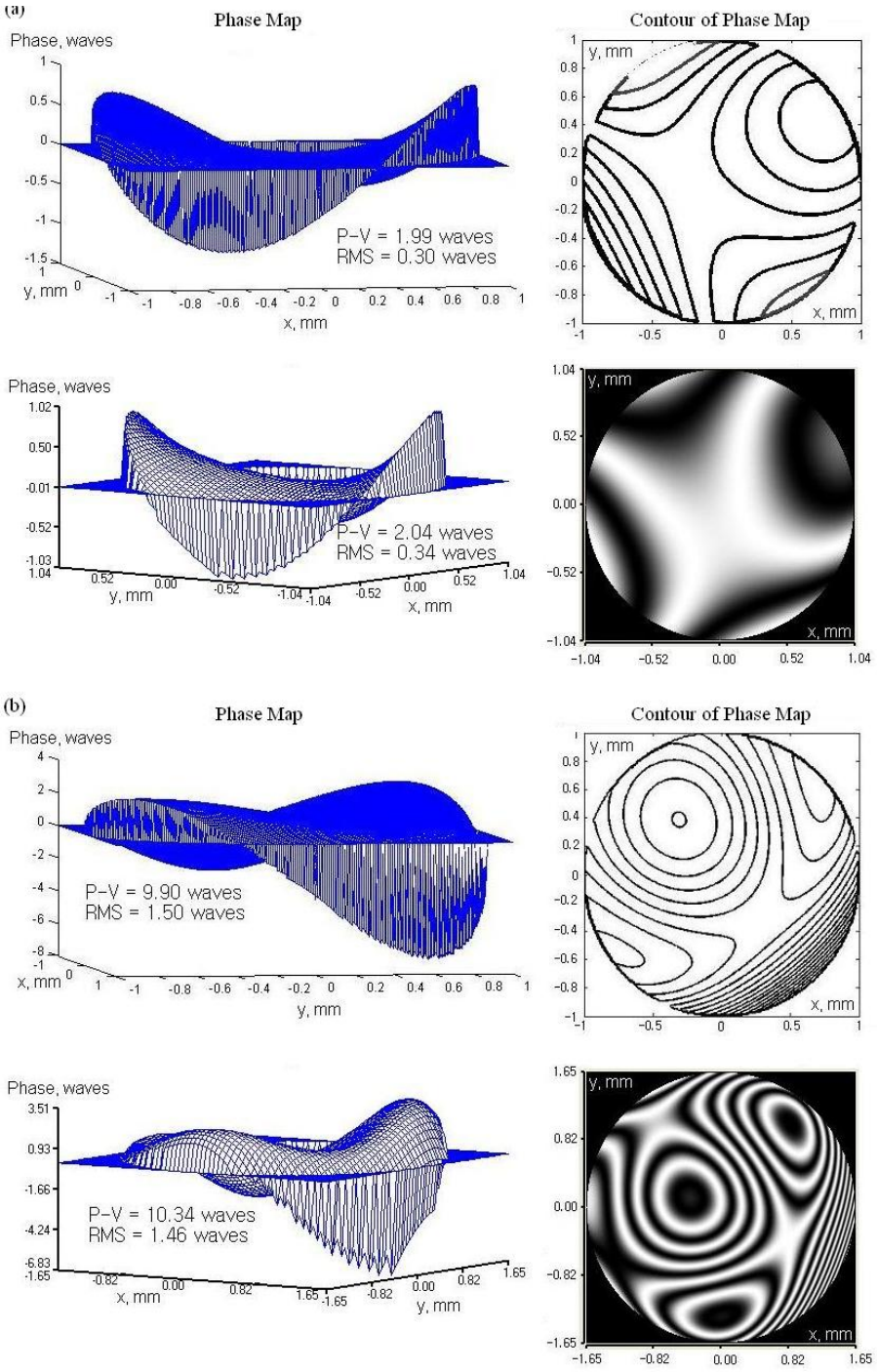

Figure 5-7 Wavefront measurement results of (a) PAL and (b) PCX by our SHWS (above) and commercial SHWS (below).

Because the reference and the distorted beams pass through exactly the same optical path in this system, the aberrations are eliminated by the reference beam. Thus, the wavefront of the optical objectives can be measured precisely. The displacements of the reference spots and the aberrated spots are detected by a CMOS image sensor and processed by the Labview® program on a personal computer. The calculation of Zernike coefficients and wavefront reconstruction are performed by Matlab® .

The wavefront measurement accuracy of our SHWS was evaluated by a comparative measurement with the commercial wavefront sensor. Unlike our SHWS that calculated 37 wavefront slopes, the commercial SHWS automatically chose the brightest centroid spots to calculate aberrations. The number of spots found is variable; it depends on two parameters- the intensity threshold (with respect to the intensity of the brightest spot) and the upper limit of maximum number of spots. The commercial program searches for spots in the reference pattern and builds bounding boxes around them. Then, spots of the main pattern are searched within the bounding boxes calculated from the reference pattern. Our SHWS apply the same technique; however, the calculated number of spots is fixed to 37.

As shown in Figure 5-7(a), from a review of the coefficient and the contour map, we noticed that the astigmatism aberration dominates in which light in one plane (the "plane of the paper" or meridional plane) focused at different location from the orthogonal plane. The root-mean-square (RMS) value of the wavefront aberration calculated by the commercial SHWS is 0.336λ (λ = 630 nm) while the RMS value calculated by our SHWS is 0.3λ. The measurement difference is less than λ/25 in RMS. Figure 5-7(b) shows the result for testing a PCX lens. The above plot shows the measured wavefront which resulted in combination of coma and astigmatism aberration,

nevertheless the coma aberration still dominates as expected and the plot below shows the expected wavefront taken by the commercial SHWS, and. The peak to valley difference is 0.438λ and the RMS wavefront difference is 0.036λ. The commercial SHWS calculated 19 wavefront slopes. Table 5-3 shows the comparison of wavefront measurement results between commercial SHWS and our SHWS.

Table 5-3 The comparison of wavefront measurement by our SHWS and commercial SHWS.

Lens	**RMS (λ = 630 nm)**		**Peak-to-Valley (λ = 630 nm)**		**Wavefront Aberration**
	our SHWS	**commercial SHWS**	**our SHWS**	**commercial SHWS**	
PAL	0.3λ	0.336λ	1.987λ	2.043λ	Astigmatism
PCX	1.5λ	1.464λ	9.903λ	10.341λ	Coma

We believe that high sensitive wavefront sensors could be used in measuring dynamic deformation of microstructures under high operation frequency [11]. There, however, is a tradeoff between dynamic range and sensitivity according to the number of microlenses and the focal length [12]. A small-size, long-focal-length MLA could increase the measurement accuracy associated with Equation (1.6) [9]. A longer focal length will provide high sensitivity in determining the average slope across each lenslet under a given wavefront [13]. Nevertheless, a microlens array with a shorter focal length will have greater dynamic range at the cost of reduced sensitivity. According to Equation (1.3), the focal length of microlens array is related to the radius of curvature of the lens. In order to produce a short or long focal length MLA, the size of the lenslet need to be redesigned. However, by our new proposed method, we do not have to redesign and fabricate new microlenses; different focal lengths can be realized by

simply modifying the refractive index difference without changing the MLA size. The master mold could be reused to replicate new optical transparent polymers and different MLA materials could be applied, which results in different focal length MLAs. Hence, we could build distinctive characteristic SHWS according to different applications.

In order to verify the feasibility of this technique, we also fabricated an SU-8 (n = 1.59) polymer MLA which has shorter focal length of 2.6 mm. Figure 5-8 shows the wavefront measurement compared between the previous built SHWS with long focal length and the new SHWS with SU-8 MLA as the lenslet component. Both evaluated wavefronts were dominated by defocus aberration which corresponds to the parabola-shaped optical path difference between two wavefronts that was tangent at the vertices and had different curvature radii. The peak-to-valley difference between long focal length MLA SHWS and shorter focal length MLA SHWS is 0.433λ. The RMS wavefront of the long focal length MLA SHWS is λ/20 less than the shorter focal length MLA. In other word, long focal length MLA SHWS has higher accuracy and sensitivity than the expected 1.17λ wavefront in rms. As a result, another advantage of the proposed microlens is that we can make different MLAs without changing lens curvature or pitch size. That means that the spatial resolution can be kept the same while the sensitivity is changed.

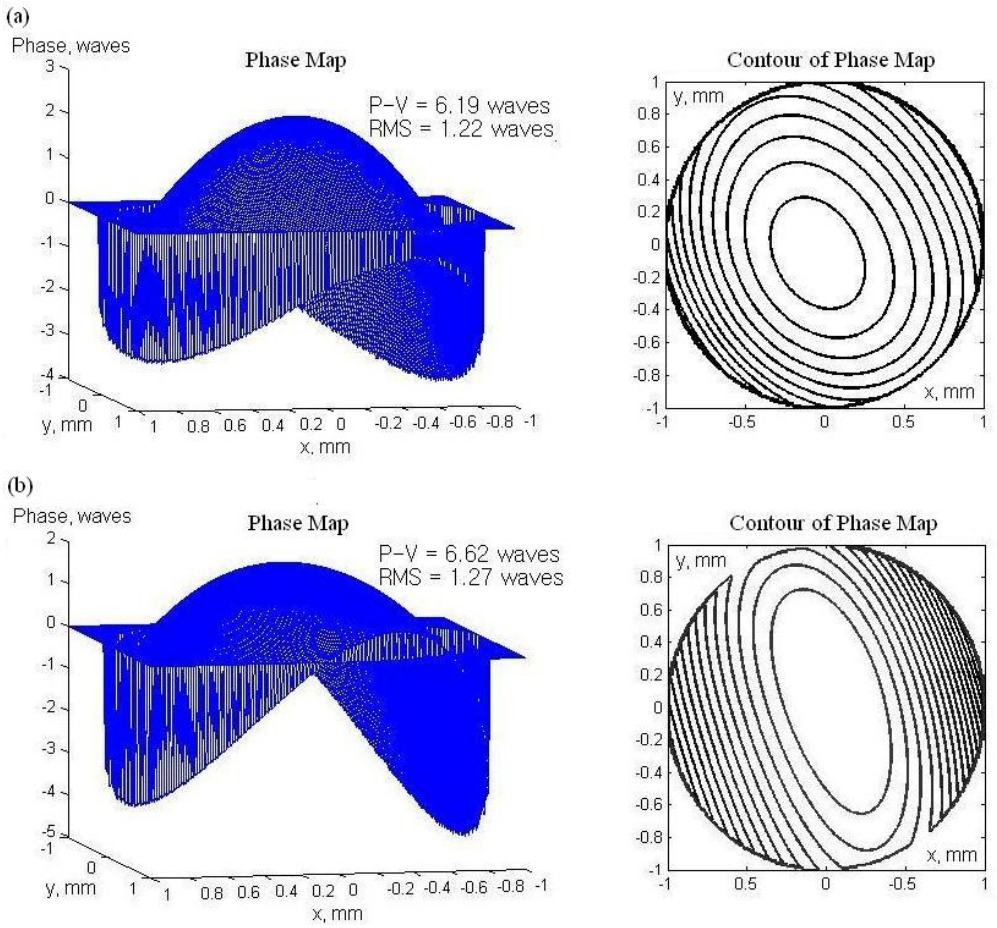

Figure 5-8 Wavefront measurement results of defocus by using (a) long focal length (UV-resin) and (b) shorter focal length (SU-8) MLA as our SHWS lenslet component.

5.5 Conclusions

A simple and easy method to extend the focal length of MLAs was experimentally demonstrated. A covered PDMS layer was room-temperature cured upon the MLA. Because of the reduced refractive index difference, the light is less refracted and this results in a long focal length. We used the UV-resin microlens to implement the MLA and other materials, such as SU-8, can be employed with the same concept, resulting in a shorter focal length MLA. Different focal lengths could be available using the same

master mold by simply modifying the refractive index of the microlens material. In other words, we can achieve different MLAs without changing the curvature or pitch distance. The method in this work also provides a significant increment in the focal length and the development of long focal length MLAs has been successful both using UV-resin and SU-8 as the MLA material.

The fabricated MLAs were also compatible with a CMOS image sensor in constructing wavefront sensors. The wavefront measurement accuracy of our wavefront sensor was evaluated by a comparative measurement using a commercial wavefront sensor, which was less than λ/25 in RMS difference. On the other hand, we also compared a long focal length MLA and a shorter focal length MLA produced by the same method with different refractive index difference. The wavefront measurement result verifies that the long focal length MLA has higher accuracy and sensitivity and its RMS is λ/20 better than that of the shorter focal length MLA. Hence, our MLA fabrication method has high reproducibility and could be implemented to build SHWS with different specifications. Spatial resolution remains the same while sensitivity is changed. The proposed double layer microlens was proven to be suitable for wavefront sensing applications.

References

[1] Vinna Lin, Application of long-focal-length microlens arrays on Shack-Hartmann wavefront sensor, published master thesis, National Taiwan University, Taipei, Taiwan (2011).

[2] Platt, B.C. History and principles of Shack-Hartmann wavefront sensing. *J. Refract. Surg.* **2001**, *17*, 573-577.

[3] Liang, J.; Grimm, B.; Goelz, S.; Bille, J.F. Objective measurement of wave aberrations of the human eye with the use of a Hartmann-Shack wave-front sensor. *J. Opt. Soc. Am. A* **1994**, *11*, 1949-1957.

[4] Daly, D.; Stevens, R.; Hutley, M.; Davies, N. The manufacture of microlenses by melting photoresist. *Meas. Sci. Tech.* **1990**, *1*, 759-766.

[5] Sinzinger, S.; Jahns, J. *Microoptics*; Wiley-VCH: Weinheim, Germany, 2003.

[6] Hecht, E. *Optics*, 4th ed.; Addison-Wesley: Reading, MA, USA, 2001.

[7] McDonald, J.C.; Whitesides, G.M. Poly(dimethylsiloxane) as a Material for Fabricating Microfluidic Devices. *Acc. Chem. Res.* **2002**, *35*, 491-499.

[8] Fischer, R.E.; Tadic-Galeb, B.; Yoder, P.R. *Optical System Design*; McGraw-Hill: New York, NY, USA, 2008.

[9] Yoon, G.Y.; Jitsuno, T.; Nakatsuka, M.; Nakai, S. Shack Hartmann wave-front measurement with a large F-number plastic microlens array. *Appl. Opt.* **1996**, *35*, 188-192.

[10] Malacara, D. *Optical Shop Testing*; Wiley-Blackwell: New York, NY, USA, 2007.

[11] Brown, M.; Gong, T.; Neal, D.R.; Roller, J.; Luanava, S.; Urey, H.; Measurement of the dynamic deformation of a high frequency scanning mirror using a Shack-Hartmann wavefront sensor. *Proc. SPIE* **2001**, *4451*, 480-488.

[12] Greivenkamp, J.E.; Smith, D.G.; Gappinger, R.O.; Williby, G.A. Optical testing using
Shack-Hartmann wavefront. *Proc. SPIE* **2001**, *4416*, doi:10.1117/12.427063.

[13] Greivenkamp, J.E.; Smith, D.G. Graphical approach to Shack-Hartmann lenselet array design. *Opt. Eng.* **2008**, *47*, 063601.

PART II DEFORMABLE MIRROR

Chapter 6 Controlling a MEMS Deformable Mirror in a Miniature Auto-Focusing Imaging System

Conventional auto-focusing camera modules adjust their optical focus by moving lenses. Although motors, such as stepping motors or voice coil motors, can change the lens position with great precision and thus vary the image sharpness, large volume and excess power consumption remain critical issues for mobile device applications. This work discusses an auto-focusing camera module that adopts a microelectromechanical system (MEMS) deformable mirror (DM) with variable focusing capability to replace mechanical motors. The deformable mirror used in this work can provide 20 diopters of focusing capability, which is one order of magnitude higher than silicon-based deformable mirrors, so the autofocus module can be compact enough for mobile devices. Because of the characteristics of MEMS deformable mirrors, we proposed a "percentage-drop" searching algorithm to find a sharp image based on a focus value calculation. The average auto-focusing time is 45% faster than the global searching method.

6.1 Introduction

Because of extreme competition within the mobile phone industry, improving the quality of images captured with built-in camera modules is a critical issue. Consequently, auto-focusing camera modules are common components of present-day smartphones that can increase the image sharpness of photographs by varying the optical power of the whole imaging module intelligently. Furthermore, the strong demand for compact camera phones results in restrictions on the thickness of the camera modules. A typical auto-focusing camera module varies the optical power, which is also known as the focal length or the focal power, by moving the interior lenses with mechanical motors. The space occupied by the actuating motors and the reserved space for the moving lenses increase the volume of auto-focusing camera modules.

There are two alternative solutions for varying the optical power of a camera module without moving any lenses. One solution is the refractive-type design, which was reported by B. Berge et al. [1, 2]. Refractive optics designs adopt a biliquid lens that can deform the shape of the interface between two immiscible liquids by the electrowetting method. By changing the distribution of the two liquids, the camera module can change its optical focusing power. However, this approach might suffer some physical difficulties, such as density mismatching of the two liquids, changing of ambient temperature, shaking, and tilt of the module. The other proposed solution is a reflective-type design, which adopts a MEMS deformable mirror (MEMS DM) to vary the optical power of the camera module. D. Wick et al. [3] demonstrated that deformable mirrors with a variable focal length can be used to eliminate mechanical motors in zoom lens systems. By changing the surface of a deformable mirror, the optical power of the module changes to a designated degree. However, most

commercially available MEMS DMs are made by rigid silicon-based materials [4, 5], and their optical power adjustment capability is less than one diopter. This results in a large optical layout space and is not suitable for mobile devices. In addition, the actuating voltages were reported to be up to 300 volts.

This work discusses a new auto-focusing camera system, which features a reflective optics design based on a polymer MEMS deformable mirror and a control program. The optical power of the polymer MEMS DM is approximately 20 diopters, which is one order of magnitude higher than silicon-based DMs. The driving voltage is approximately 150 volts [6]. Because the deformable mirror described in this work is quite different from the traditional mechanical motors used in most cameras, the fabrication of a deformable mirror is discussed first. Because of the particular optical characteristics of this new auto-focus module, we then propose the percentage-drop searching algorithm to find the sharpest image. This algorithm was developed based on the focusing characteristics of the polymer deformable mirror. Finally, experiments were performed to demonstrate this idea. To the best of our knowledge, this is the first time that an automatic controlling mechanism has been applied to a MEMS deformable mirror to achieve an autofocus function in a miniature camera.

6.2 Deformable Mirror and Optical System Design

The schematic drawing of a MEMS deformable mirror is shown in Figure 1 [7, 8]. A deformable mirror comprises two electrode plates: a top electrode plate and a bottom electrode plate. At the top electrode plate, as shown in Figure 6-1(a), a polymer membrane is sandwiched between two aluminum layers and lies upon the

square-opened silicon wafers. On the other side is a layer of insulator spacer with a circular opening. Aluminum coated on both sides of the polymer membrane is used as a conducting electrode and to reflect the light. The polymer layer is also kept away from oxygen and moisture to ensure good reliability by double-sided, coated aluminum [9]. At the bottom electrode plate, as shown in Figure 6-1(b), aluminum was first coated on the silicon wafer and then photoresist-made arrays were planted on the aluminum layer in a cylindrical shape. The photoresist serves as an adhesive for wafer bonding [10] and is used to exhaust air when the membrane is deformed. Figure 1(c) shows the bonding of the top and bottom electrode plates. The fabrication of the polymer deformable mirror was accomplished by a complementary metal oxide semiconductor (CMOS)–compatible micromachining process. The description of the fabrication process was detailed in a previous work [11]. When a voltage difference is applied between the top electrode plate and the bottom electrode plate, the electrostatic force pulls down the planar polymer membrane toward the bottom electrode plate, as shown in Figure 6-2. The polymer membrane then acts as a concave mirror to focus the light variably by adjusting the applied voltage.

Figure 6-3 illustrates the relation between the optical power of the polymer deformable mirror and the applied voltage on the electrode plates. Note that a diopter is a unit of optical power and is the reciprocal of the focal length measured in meters. When the applied voltage was raised to 150 volts (V), the center-displacement of the deformable mirror was approximately 15 μm, and the corresponding optical power was approximately 20 diopters. This is very close to the maximal displacement of this deformable mirror limited by the pull-off effect. Besides, the increasing rate of optical power was higher as the voltage increased. The response time of the deformable mirror has been reported as 400 μs [11].

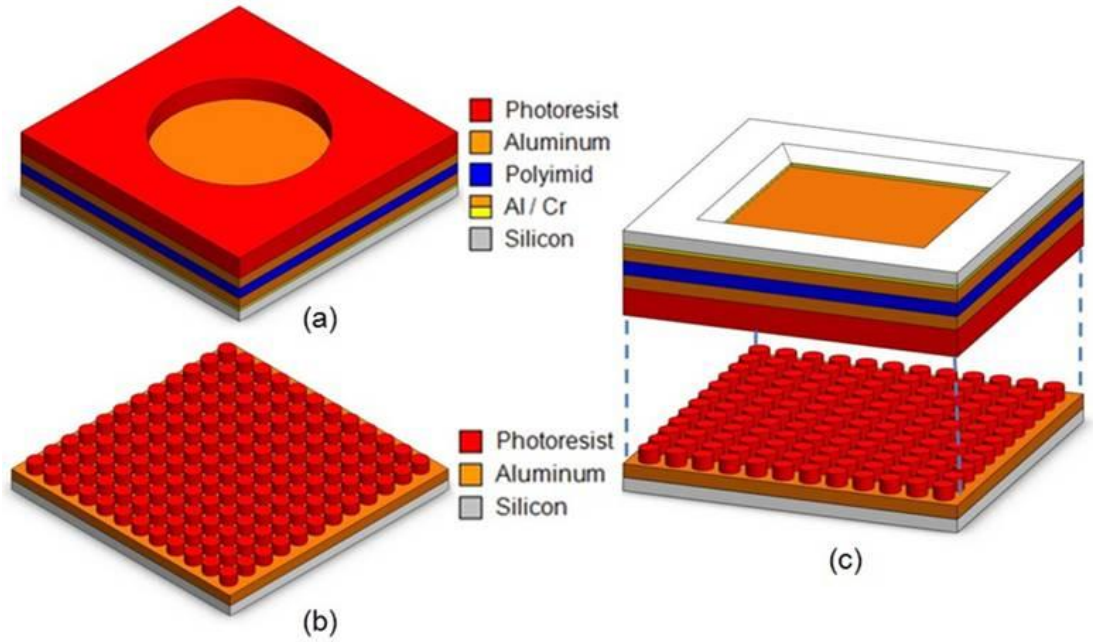

Figure 6-1 Structure of MEMS deformable mirror [(a) Top electrode plate; (b) Bottom electrode plate; (c) Encapsulation].

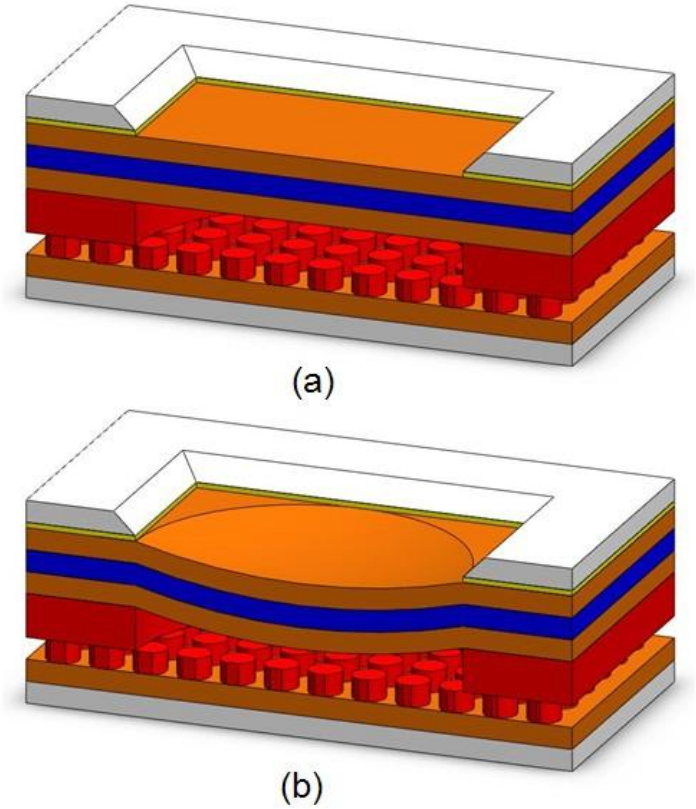

Figure 6-2 Deformable Mirror [(a) Without an applied voltage; (b) With an applied voltage]

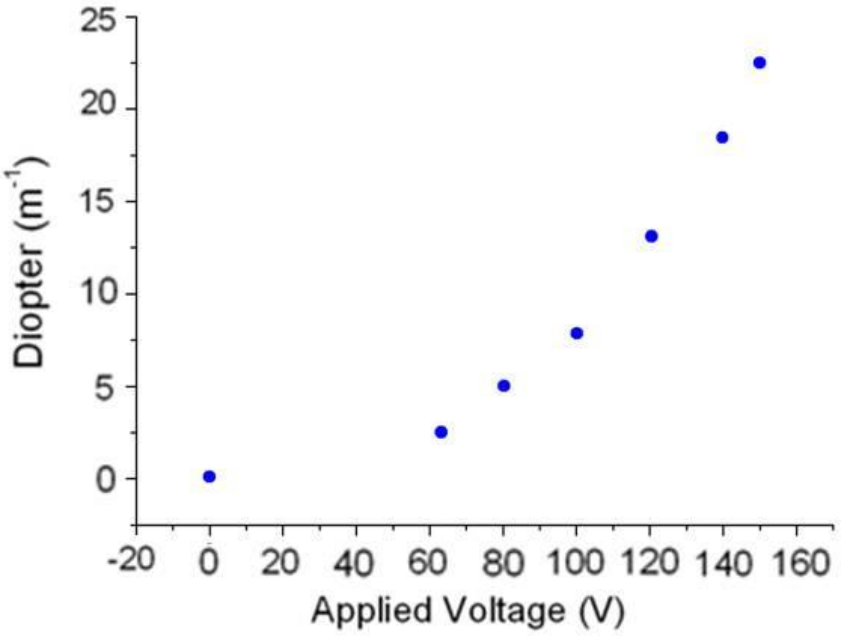

Figure 6-3 Relation between the optical power of the deformable mirror and the applied voltage difference.

The optical design of this auto-focusing camera module consists of one MEMS deformable mirror, one ordinary mirror, and two aspherical acrylic solid lenses, as shown in Figure 6-4. The light bundles first go through the first solid lens called Lens 1, which is designed to collect wide-angle light. This module can focus light within ± 26 degrees. Then, light is reflected by an ordinary mirror to the polymer deformable mirror. An aperture stop is used to reduce the noise caused by scattering. The deformable mirror reflects and refocuses the lights to the corresponding focal point. Finally, light goes through the second solid lens called Lens 2, which refocuses the light and reduces aberrations. An image is formed on an electronic image sensor. Therefore, the MEMS DM is used to alter the effective focal length (EFL) of the whole optical system to achieve autofocus function. A cover is then placed on top of the base to block out auxiliary lights. Figure 6-5 shows that the module is approximately 8.3

mm thick, 11.5 mm long, and 10 mm high. By using this design, a long total-track-length can be realized in a thin optical module.

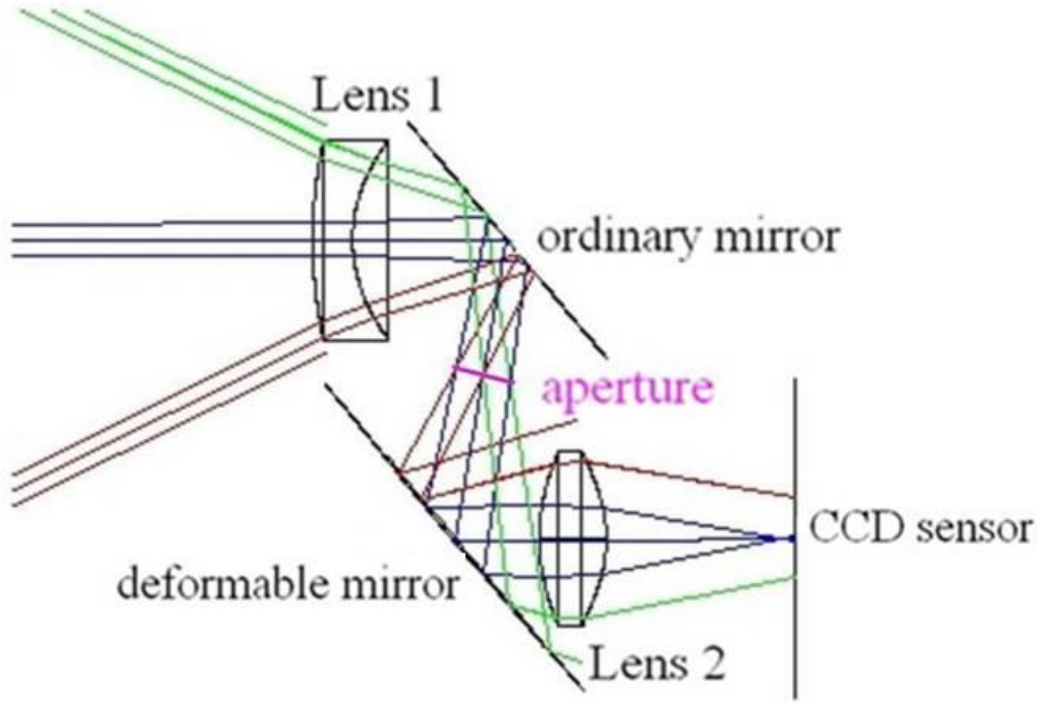

Figure 6-4 Optical system layout of the reflective auto-focusing camera module.

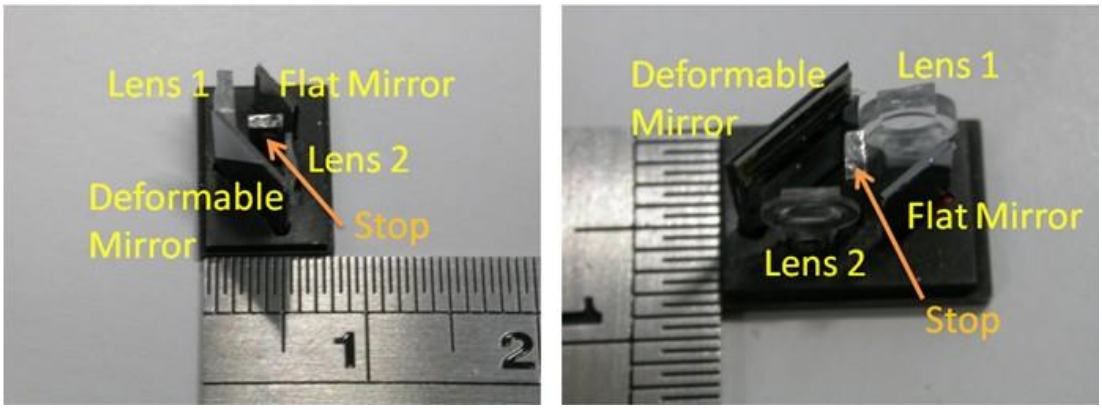

Figure 6-5 Picture of the actual optical camera module.

Figure 6-6 shows the modulation transfer function (MTF) of the camera module in this work. The MTF is the widely used scientific method of describing lens performance. The higher MTF means better image performance. There are three groups of MTF lines from different view's angles. The blue, red, and green lines represent viewing angle of 0, 26, and -26 degree, respectively. We name the viewing angle of 0 degree as "on axis", and the other two are "off-axis." There are two lines of each group with the same colour. One represents tangential plane as "T", and another represents sagittal plane as "S". The on-axis MTF has good performance, which is approximately 0.13 at full spatial frequency and 0.28 at half spatial frequency. The full spatial frequency is calculated by $1/(2\times pixelsize)$ and the image pixel size is 2.1 μm in this experiment. The off-axis MTF still needs optimization in the sagittal direction because of the Z-shape folded optical path. All the aberrations are minimized and the dominant aberrations are astigmatism and distortion, according to the optical simulation software ZEMAX. In our previous work [12], we noticed that the deformation of the deformable mirrors needs to have a "biconic shape" to eliminate aberrations for closer objects. This can be achieved by properly defining the photoresist opening depicted in Figure 6-1(a).

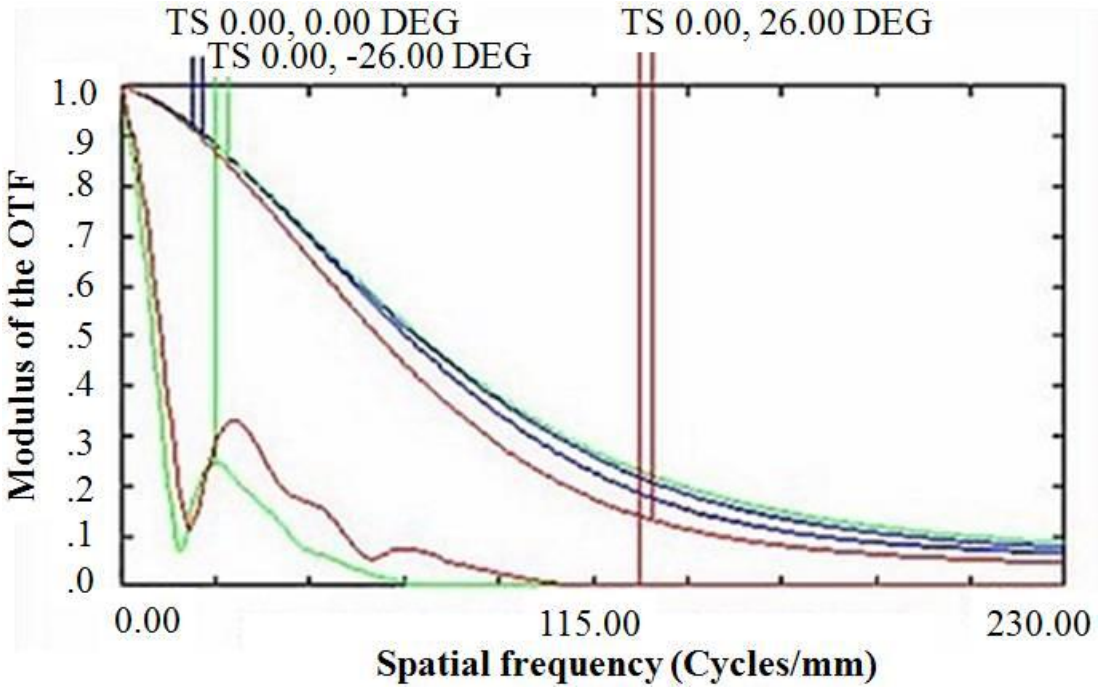

Figure 6-6 Modulation transfer function (MTF) of the optical system.

6.3 Tenengrad Method and Percentage-Drop Searching Algorithm

The level of image sharpness is defined by a pixel-based method. The pixel-based method judges the image sharpness by measuring the CMOS image sensor outputs. The degree of image sharpness is called the focus value. We chose the Tenengrad method to calculate the focus value because it uses the absolute sum of the gradient to achieve more accurate results compared with other methods [13, 14]. In addition, a single gray image averaged by three primary colors (red, green, blue) should be used to minimize the color effect. The Tenengrad sharpness function is described as follows and can be found in reference [13] and [14] :

The Sobel horizontal and vertical operators [13] are

$$i_x = \frac{1}{4}\begin{bmatrix} -1 & 0 & 1 \\ -2 & 0 & 2 \\ -1 & 0 & 1 \end{bmatrix} \quad \text{and} \quad i_y = \frac{1}{4}\begin{bmatrix} 1 & 2 & 1 \\ 0 & 0 & 0 \\ -1 & -2 & -1 \end{bmatrix} \tag{1.10}$$

,which are used to find the strength of the horizontal and vertical gradients respectively by convolution calculations of image pixels. The image sharpness is then defined as

$$\frac{1}{n}\sum_x \sum_y \left(S(x,y), S(x,y) > T\right) \tag{1.11},$$

where $S(x,y) = \left(i_x * f(x,y)\right)^2 + \left(i_y * f(x,y)\right)^2$, *f(x,y)* is the pixel intensity, T is the threshold value selected to restrain the effect of the noise, and *n* is the number of pixels in the focusing window.

The searching algorithm helps the auto-focusing system find the optical power with the best focus [15], such as the interior lens position for a conventional camera module. Unlike mechanical motors, the polymer MEMS DM shows an increasing rate of optical power when the driving voltage is increased. This makes its focusing characteristics different from conventional autofocus modules with mechanical motors. Figure 6-7 shows the experimental plot of the focus value with two different object distances (50 mm and 200 mm). The voltage applied to the deformable mirror ranged from 0 to 150 volts. In this experiment, a postcard featuring words of different sizes was used as the sample object. While the object was placed closer to the camera module, the maximal focus value occurred at a higher voltage. This results in a larger center displacement of the deformable mirror. The plot of focus value was normalized at a two-object distance in order to easily compare the location of the maximal image sharpness.

Figure 6-7 shows the asymmetric and monopeak curve based on this optical imaging system featuring a MEMS DM. The slope beyond the peak value is much steeper than before it. So, the drop in the focus value is much larger after the peak.

The asymmetric curve is very different from a conventional motor-based camera module, which is almost symmetric in shape. Therefore, based on the characteristics, we propose a searching algorithm called "percentage-drop searching," as shown in Figure 6-8. Percentage-drop searching is a modified global searching method [16], where not all searching steps, or the specified center-displacement of the deformable mirror, are scanned. The continuously changing optical power lasts until a percentage-drop of the focus value from a preceding amount is detected, as shown in Figure 6-8. In the percentage-drop search, we used two parameters to find the best image: the focus value and the drop of focus value. The speed of this method is determined in part by the allowed percentage-drop of the focus value. A low threshold setting might cause the searching algorithm to be caught in a local maximum of the focus value curve. On the other hand, a high threshold value results in missing the real maximum of the focus value. We set the threshold to be 10% based on the focusing characteristics in Figure 6-7. Considering an object at 50 mm, the normalized focus value is approximately 80% when it is out of focus. The normalized focus value is 100% when the image is sharp. There is 20% difference between focused and not-focused images. We take half of this value as our threshold (i.e., 10%). This is similar to a 3 dB signal-to-noise ratio drop if we consider out-of-focus images as background noise. However, this threshold number is adjustable to fit different optical system designs.

The applied voltage steps could be inverted to fit the nonlinear characteristics of the deformable mirror, which gives a characteristic similar to other optical autofocus systems. However, according to the different process parameters, such as the diameters of the deformable mirrors, the thickness of the polymers, and the process

temperature, the characteristics of deformable mirrors could vary. This means that the voltage steps can be different for different deformable mirrors. Even though the overall optical power of the optical system was affected by the encapsulation tolerance, the trend of optical power with applied voltage was almost the same, which means smoother at the beginning and steeper at the end. An overall percentage-drop algorithm is a better method to control this characteristic.

In this auto-focusing camera system, the Tenengrad method and the percentage-drop searching algorithm were programmed in MATLAB® and LabVIEW®, respectively. The controlling program was composed of these two methods. It takes less time because fewer searching steps are taken into the image sharpness calculation, and the searching result of the percentage-drop algorithm was expected to be accurate. The experimental results are discussed in the next section.

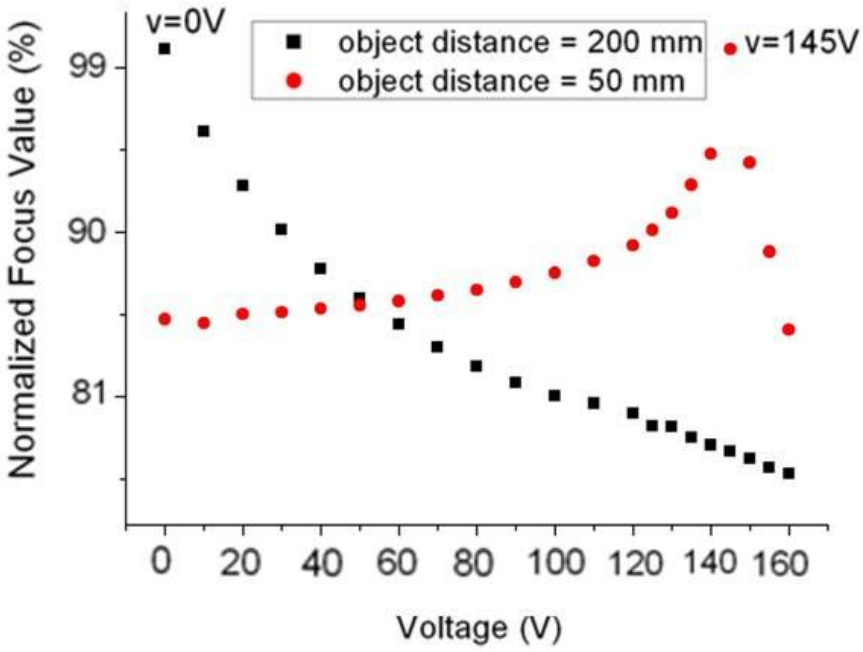

Figure 6-7 Focus value vs. applied voltage at different object distances.

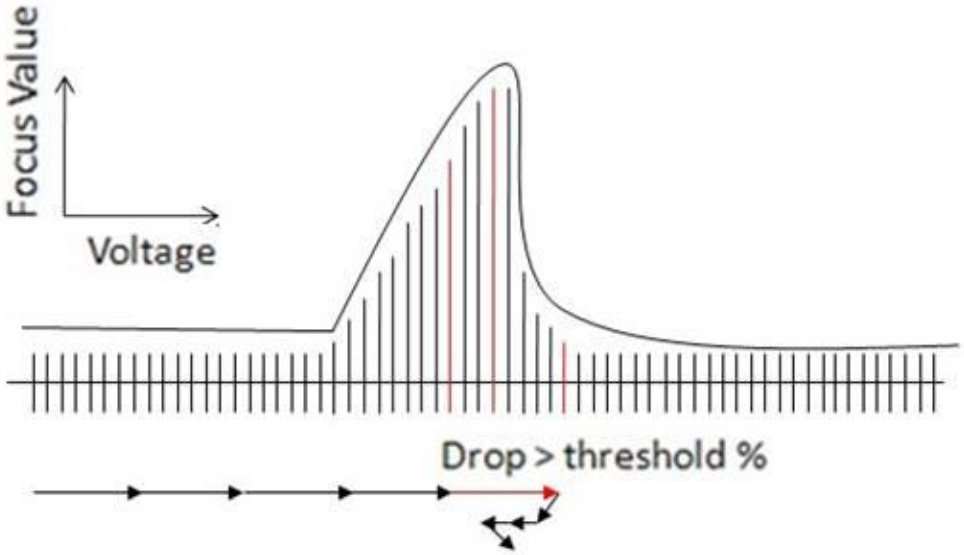

Figure 6-8 Percentage-drop searching algorithm.

6.4 Experiment Results and Discussion

Figure 6-9 shows the experimental setup of the camera system. The program is loaded on a computer, which is connected to a data acquisition (DAQ) system (NI USB-6009) to generate a voltage range from 0 to 5 V. The voltage span generated by the DAQ system is then amplified by a voltage amplifier from 0 to 800 V. The actuating voltage of the MEMS deformable mirror is sent to the camera module. The CMOS image sensor captures the real-time image and sends it to the personal computer (PC) for image sharpness calculations. By appropriately setting the output voltage of the DAQ system and the magnification of the voltage amplifier, actuating voltages in every searching step can be produced by the controlling program.

When the object was placed 50 mm away from the camera module, the image was sharper with a high applied voltage than without an applied voltage, shown in Figure

6-10(b) and (a), respectively. The deformable mirror was deformed to achieve high optical power and to make the image of the near object sharper. However, when the object was placed 200 mm away from the camera module, it was considered to be a great distance from the camera optical system. The image was sharper without an applied voltage, as depicted in Figure 6-10(c) and (d), respectively. This is what we expected because the system can effectively focus on a far object when the mirror is flat. If a high voltage was imposed on a deformable mirror, the image became sharper for a near object because the equivalent focal length was reduced and the system could focus on the close object.

Figure 6-11 shows the focus value repeatability for the percentage-drop searching algorithm. The target object was placed at specified distances (50 mm and 200 mm) away from the camera module and auto-focusing picture-taking was iteratively executed 10 times. The maximal focus value of each experiment was recorded, along with its corresponding voltage. The averages of absolute focus value were 127.1 and 284.2. Meanwhile, the standard deviations were 0.31 and 0.02 when object distances were 200 mm and 50 mm respectively. In Figure 11, the applied voltages and the maximal focus value agreed with each other when the target object was located at the same distance. The actuation voltage was 145 volts when the object is placed at 50 mm. On the other hand, we did not need any actuation voltage when the object was 200 mm away. The corresponding voltage comes down when the target object was pulled away. Though there were some differences in the maximal focus value between each time, these differences did not change the searching step in which the maximal image sharpness occurs. Thus, the results of percentage-drop searching are reliable. Moreover, the average searching time of percentage-drop searching is 1.57 seconds, and a global search takes 3 seconds, on average. The searching time is limited by the speed of the

computer hardware and the operating system. This, however, is a 45% improvement over the global search method. We also noticed that the image was not perfect because a simple auto focus control mechanism cannot correct high-order aberrations [17], such as coma and astigmatism. The autofocus mechanism can only correct the defocus aberration from the optics. Careful designs of the optical system and the MEMS deformable mirrors are still needed.

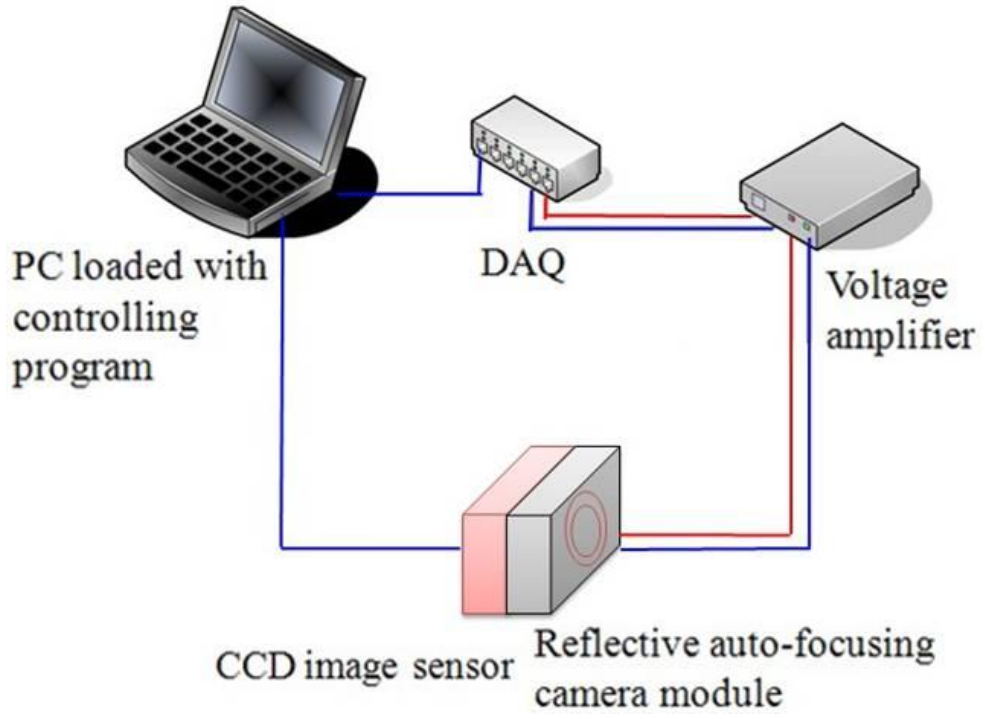

Figure 6-9 Setup of the auto-focusing camera system.

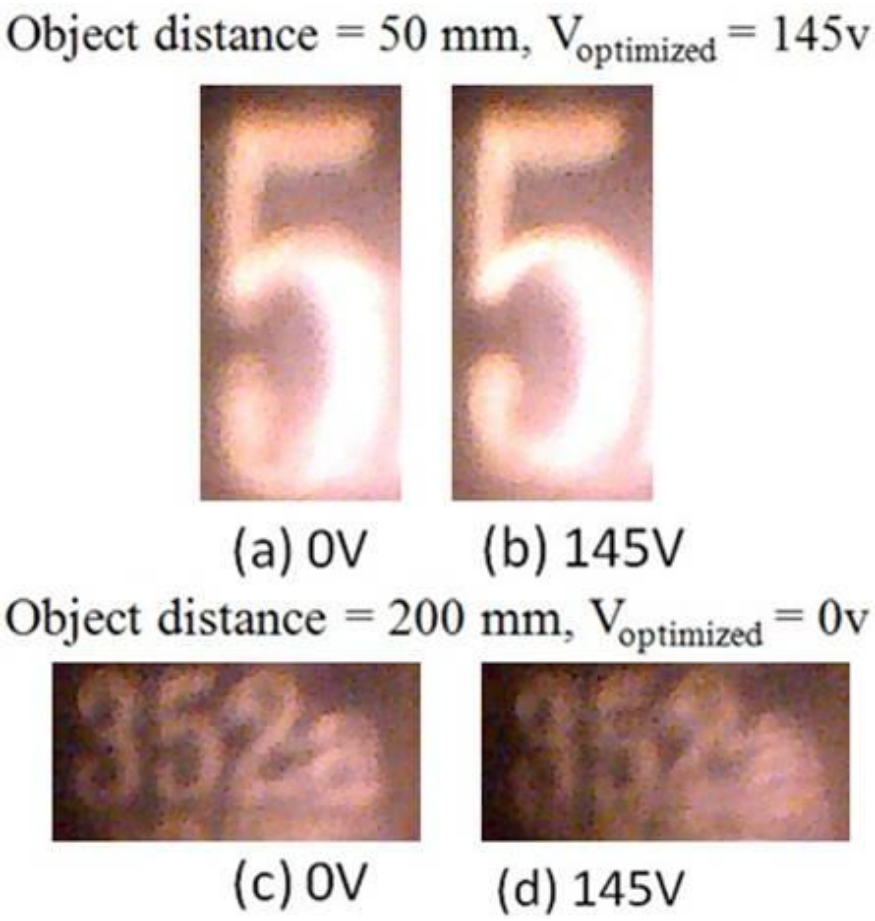

Figure 6-10 Images taken at different object distances and with optimized applied voltages.

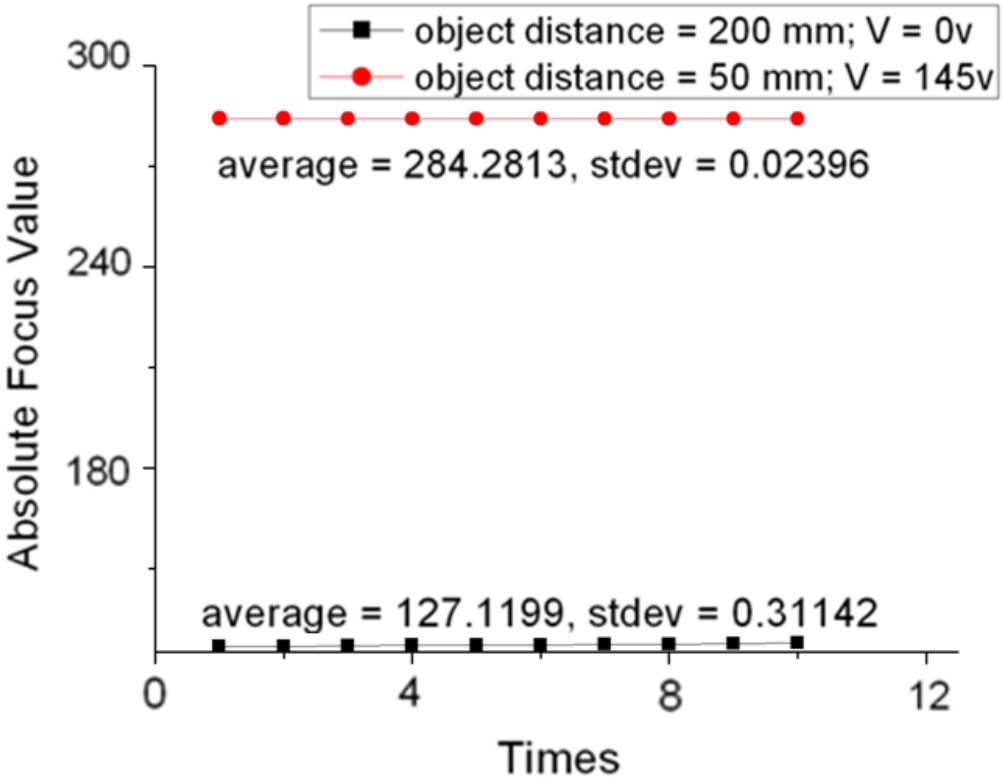

Figure 6-11 Experimental results of percentage-drop Searching. The standard deviations are 0.31 and 0.02 when the object distances were 200 mm and 50 mm respectively.

6.5 SUMMARY

An auto-focusing camera system with a MEMS deformable mirror was demonstrated to adjust the optical power of the whole system. The deformable mirror can provide 20 diopters of focusing capability, which is one order of magnitude higher than current commercial products. In order to optimize the optical performance of the MEMS deformable mirror and control it accurately, the optical properties of the deformable mirror were taken into consideration. The auto-focusing method was explained, and it includes the Tenengrad method and a percentage-drop searching algorithm. Accuracy and time issues were also discussed. Finally, we demonstrated

the experimental setup and the experimental results of this auto-focusing system. A searching time 45% faster than a global search was achieved. As a result, an innovative auto-focusing camera system has been successfully demonstrated.

References

[1] B. Berge, "Liquid lens technology: Principle of electrowetting based lenses and applications to imaging," in *Proc. IEEE Int. Conf. Micro Electro Mech. Syst. MEMS*, Miami Beach, FL, United states, 2005, pp. 227-230.

[2] C. Gabay, *et al.*, "Dynamic study of a varioptic variable focal lens," in *Proc SPIE Int Soc Opt Eng*, Seattle, WA, United states, 2002, pp. 159-165.

[3] D. V. Wick, *et al.*, "Active optical zoom system," in *Proc SPIE Int Soc Opt Eng*, Orlando, FL, United states, 2005, pp. 151-157.

[4] T. Bifano, *et al.*, "Micromachined deformable mirrors for adaptive optics," in *Proc SPIE Int Soc Opt Eng*, Seattle, WA, United states, 2002, pp. 10-13.

[5] G. Vdovin and P. M. Sarro, "Flexible mirror micromachined in silicon," *Appl Opt*, vol. 34, pp. 2968-2968, 1995.

[6] H.-T. Hsieh, *et al.*, "Thin autofocus camera module by a large-stroke micromachined deformable mirror," *Opt. Express*, vol. 18, pp. 11097-11104, 2010.

[7] Y.-W. Yeh, *et al.*, "Organic variable optical attenuator made by compliant fluoropolymer membrane," in *IEEE/LEOS Opt. MEMS Int. Conf. Opt. MEMS Applic.*, Oulu, Finland, 2005, pp. 51-52.

[8] Y.-W. Yeh, *et al.*, "Large displacement deformable mirrors made by low stress polyimide membrane," in *IEEE/LEOS Int. Conf. Optical MEMS Appl. Conf.*, Big Sky, MT, United states, 2006, pp. 116-117.

[9] J. D. Mansell, *et al.*, "A low-cost compact metric adaptive optics system," in *Proc SPIE Int Soc Opt Eng*, San Diego, CA, USA, 2007, pp. 67110K-11.

[10] C. den Besten, *et al.*, "Polymer bonding of micro-machined silicon structures," in *Proc IEEE Micro Electro Mech Syst Workshop*, Travemuende, Ger, 1992, pp.

104-109.

[11] J. Wang, *et al.*, "Miniature optical autofocus camera by micromachined fluoropolymer deformable mirror," *Opt. Express*, vol. 17, pp. 6268-6274, 2009.

[12] M.-H. Lin, *et al.*, "Auto-focus imaging systems with MEMS deformable mirrors," in *Current Developments in Lens Design and Optical Engineering X*, San Diego, CA, United states, 2009, p. 74280Q.

[13] K.-S. Choi and S.-J. Ko, "New autofocusing technique using the frequency selective weighted median filter for video cameras," in *Dig Tech Pap IEEE Int Conf Consum Electron*, Los Angeles, CA, USA, 1999, pp. 160-161.

[14] N. K. C. Nathaniel, *et al.*, "Practical issues in pixel-based autofocusing for machine vision," in *Proc IEEE Int Conf Rob Autom*, Seoul, Korea, Republic of, 2001, pp. 2791-2796.

[15] J. Schlag, *et al.*, "Implementation of automatic focusing algorithms for a computer vision system with camera control," *Proc CMU Robotics Institute*, 1983.

[16] N. Kehtarnavaz and H. J. Oh, "Development and real-time implementation of a rule-based auto-focus algorithm," *Real-Time Imaging*, vol. 9, pp. 197-203, 2003.

[17] Y. Lu, *et al.*, "Polymorphic optical zoom with MEMS DMs," San Francisco, California, USA, 2011, pp. 79310D-7.

Chapter 7 Thin autofocus camera module by a large-stroke micromachined deformable mirror

The conventional auto-focus and zoom image systems were made by a set of motor-moved lenses. Because of mechanical moving parts, it is not easy to miniaturize their sizes. In this work, we propose a thin autofocus system using a large stroke MEMS (micro-electro-mechanical systems) deformable mirror which has the potential to downscale the size and to minimize chromatic aberration. The large stroke MEMS deformable mirror is made by a polyimide membrane that has a maximum 12 μm displacement over a 3 mm aperture. The module size is 5.4 mm thick in optical design layout and 6.7 mm after packaging. This autofocus system is designed with the f-number = 4.13, on-axis MTF = 0.28 at full frequency of 230 cycles/mm, and incident light within ± 26 degree. The position of clear image can vary from 4 cm to 50 cm achieved by controlling the surface curvature of the MEMS deformable mirror.

It was the second generation of autofocus camera module by our MEMS deformable mirror. The main difference from the first generation was the optical system design which was devoted by Meng-Hsuan Lin. The image quality was much improved. The key component was the MEMS DM fabricated by Hsin-Ta Hsieh. My main contribution was the integration of hardware and software, such as sharpness function and searching algorithm, to realize an autofocus camera function. Meanwhile, I also re-simulated the optical system regarded different angle fields and the oval opening. The content was adopted from the published paper in Optics Express with minor revisions. Section 7.1 to section 7.5 are materials from Meng-Hsuan Lin, Hsin-Ta Hsieh [1], and

me. Although the material in this chapter is mainly from Hsin-Ta Hsieh's paper which published in Optics Express, the material in the paper was also from Meng-Hsuan Lin's thesis and my conference paper in OPT2009. Figure 7-1, -2, -6 are from Meng-Hsuan Lin's work. Figure 7-3 and 7-5 are from Hsin-Ta Hsieh's work. Figure 7-4, 7, 8, 9 are from my own work.

7.1 Introduction

Conventional autofocus or zoom systems require a set of lenses and need large space because of mechanical motors. Recently, a MEMS-based motion control stage is used to minimize the space of mechanical motors [2]. However, manipulation of the space between lenses is not the only way to change the effective optical power. It also could be done by either varying the surface curvature or changing the refractive index distribution. These methods can be generally divided into refractive type and reflective type. Liquid lens [3] and liquid crystal lens (LC lens) [4] belong to refractive type. Liquid lens adopts bi-liquid lenses that can deform the shape of the interface between two immiscible liquids by electro-wetting method. Liquid crystals (LCs) are excellent electro-optic materials with electrical and optical anisotropies. The optical properties can be controlled easily by external electric field. According to the change of refractive indices, the light can be converged and diverged. However, both liquid lens and liquid crystal lens need to utilize refractive design forms that require straight optical path. This fundamentally limits packaging thickness.

Another solution is reflective type, which adopts MEMS deformable mirrors (MEMS DM) to vary the optical power by deforming reflecting surfaces [5,6]. The advantage of reflective type is chromatic aberration free [7]. Besides, the straight optical

path can be folded to reduce packaging thickness. DMs could be embedded with wave front sensors to correct the wavefront aberration for astronomical observation [8]. The system is commercialized for years [9]. Traditionally, MEMS DMs are made by inorganic materials, such as silicon or silicon nitride. These materials have high mechanical stiffness, which limits their deformation range [10]. The deformation of MEMS DM presented in this work is about one order of magnitude higher than commercial products. In this work we propose an optical system using a polymer MEMS DM in a reflective design form. The polymer MEMS DM could achieve 12-μm displacement over a 3-mm aperture that corresponds to about 20 diopter focusing power. The optical layout design is 5.4 mm thick and 6.7 mm after packaging. The optical system design, performance analysis, experimental results are discussed in following sections.

7.2 Optical System Design with Autofocus Function

The autofocus module in this work was designed in a Z-shape configuration, which consists of two solid lenses, a free-form shape mirror, a polymer MEMS DM, an aperture stop, and a 1/4" 2M pixels (2.2 μm × 2.2 μm per pixel) image sensor. The lens 1 is a diverging lens with negative power and the lens 2 is a converging lens with positive power. The function of lens 1 and lens 2 is to focus objects on to an image plane. There is a free-form shape mirror at the last surface to eliminate the residual on-axis aberrations because of large incident angle on lens surfaces. The total effective focal length is about 5.7 mm, f-number is 4.13, and the incident light is within ± 26 degree as show in Figure 7-1(a). However, the vignetting exists for light at large field angle and the off-axis aberrations degrade the MTF. The system can be optimized by

carefully optimize other solid lenses and reflecting surfaces as in [11]. The total thickness is about 5.4 mm due to folded light beams. The best performance is on-axis, and the MTF drops to 30 cycles/mm at 26-degree field angle. Figure 7-1(b) shows the on-axis MTF of the system when the object is placed at 500 mm and the MEMS deformable mirror is flat. At this distance, the object is considered far compared with the effective focal length of the system. The modulation is above 20% at the full frequency of 230 cycles/mm. The full frequency is determined by the size of the imaging pixel, which is 2.2 μm in this case. One can see that the total optical path is about 18 mm, but the thickness can be reduced to about 5 mm by folding its optical path. This means that we could adopt longer optical path designs to release high power lenses requirement. In other words, we could use solid lenses with lower power that are easier to be fabricated and cause less aberration. This reflective design also gives us flexibility of accommodating larger image sensors without increasing packaging thickness too much.

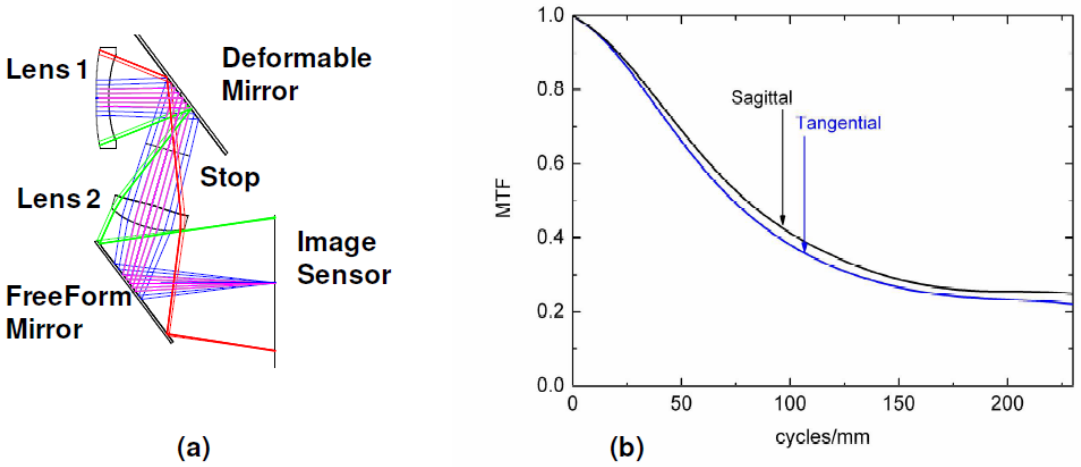

Figure 7-1 (a) Optical system design in reflective form, and (b) its modulation transfer function (MTF) when a MEMS deformable mirror is flat for far objects

When an object is placed closer to the autofocus module, the image position is expected to move away from the original position. To amend the image position change, the focusing power of a MEMS deformable mirror must be changed accordingly. When the object position is changed from 500 to 44 mm, the focusing power of a MEMS DM must be adjusted from 0 to 20 m^{-1} (i.e. flat to curve) in the optical system of Figure 7-1(a). The image of lady Lenna was simulated by ZEMAX® to illustrate this change. Figure 7-2(a) shows the image analysis simulation calculated by ray tracing method. We can observe that it will focus on 500 mm object with a flat MEMS DM. If the object is brought to 44 mm from the lens 1, we need to actuate MEMS DM to 20 diopter focusing power, which is approximately corresponding to 100 mm radius of curvature. Figure 7-2(b) shows the MTF of the optical system when the deformable is actuated to 20-diopter and the object is placed at 44 mm. One can see the MTF dropped slightly compared to a flat mirror, but still above 20% at the full frequency.

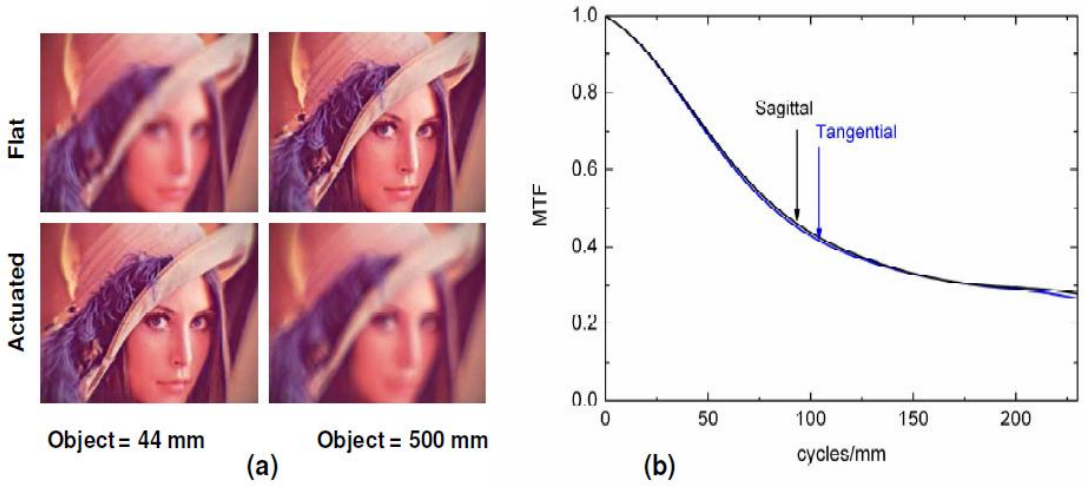

Figure 7-2 (a) Image simulation results of Lady Lenna, and (b) its modulation transfer function (MTF) when a MEMS deformable mirror is actuated for near objects.

7.3 Device Fabrication

The key component of the autofocus module is MEMS DM. The MEMS DM in this work consists of two parts. One is a deformable membrane and the other is a bottom electrode. A deformable membrane is a mirror made of a thin polyimide layer coated with aluminum reflecting layers and is actuated by electrostatic force. The deformable mirror was fabricated by MEMS technology. In deformable mirror part, we started from a (100) silicon wafer that is double side polished. A 6000 Å thermal oxide was grown for masking layer in wet etching process. Then, we patterned a square opening window on one side of oxide. We etched the non-PR covered region of oxide by BHF and remove PR after etching finished, as shown in Figure 7-3(b). The wafer was dipped into a 90 ℃ TMAH solution for about 8 hours wet etching tank and this resulted in a 25-μm residual silicon layer as Figure 7-3(c). The Al/Cr (1200 Å / 200 Å) layer were evaporate on the flatten side. Aluminum layer will become reflection layer and chromium layer can solve the adhesion problem. The polyimide PI-2610 from Dupont® was spun at 4000 rpm for 60 seconds and was cured at 300 ℃ for 30 minutes in furnace to form a polymer layer on aluminum. We evaporated another Al (1200 Å) layer for electrode and this formed a sandwich structure with polymer and previous Al layer as Figure 7-3(e). We choose the polyimide because similar coefficient of thermal expansion to Si substrate results in low thermal strain and low residual stress. The sandwich configuration balances the residual stress on double side of polymer layer. A PR (photoresist) layer was spun and an elliptical opening was defined on it to form an elliptical outside frame of a DM as Figure 7-3(f). The opening of the photoresist can be changed accordingly to fit into optical system design. In our design, the silicon opening is a 3.5 mm square and the PR opening is a 3 mm ellipse. The thickness of the PR

opening is 20 μm and is used to define the deflection shape of the polyimide membrane. Finally, we removed the residual Si layer by XeF2 and etched the oxide and Cr layer on reflection Al layer as shown in Figure 7-3(f). The remaining oxide on the membrane was then removed by Pad Etchant S (from AUECC, Taiwan.), which minimizes damage to metal layers unlike traditional buffered hydrogen fluoride (HF).

Regarding the bottom electrode part, a conducting Al/Cr layer was evaporated on a flatten wafer with an isolation oxide layer. In Figure 7-3(g), PR pillars were patterned to form air channels and short-circuit protection stoppers, which prevent DM from damage at snap down voltage. These air channels are important to improve the response time of the membrane because a sealed cavity underneath the membrane will slow down the moving speed of a membrane due to air damping effect. The thickness of the pillar is 12 μm so that the total gap between the polyimide membrane and the bottom Al electrode is 32 μm. This provides enough spacing for the membrane to deform to 20-diopter before snapping down caused by electrostatic force. Finally, top membrane and bottom electrode were bonded together by 100N force at 120C for 60 minutes. In order to connect the wires from the back side of DM, two small cavities were opened in TMAH etching step. Two conducting wires were attached on a DM by conductive epoxy. Due to the tensile residual stress of the polyimide membrane, the reflecting surface is very flat [4].

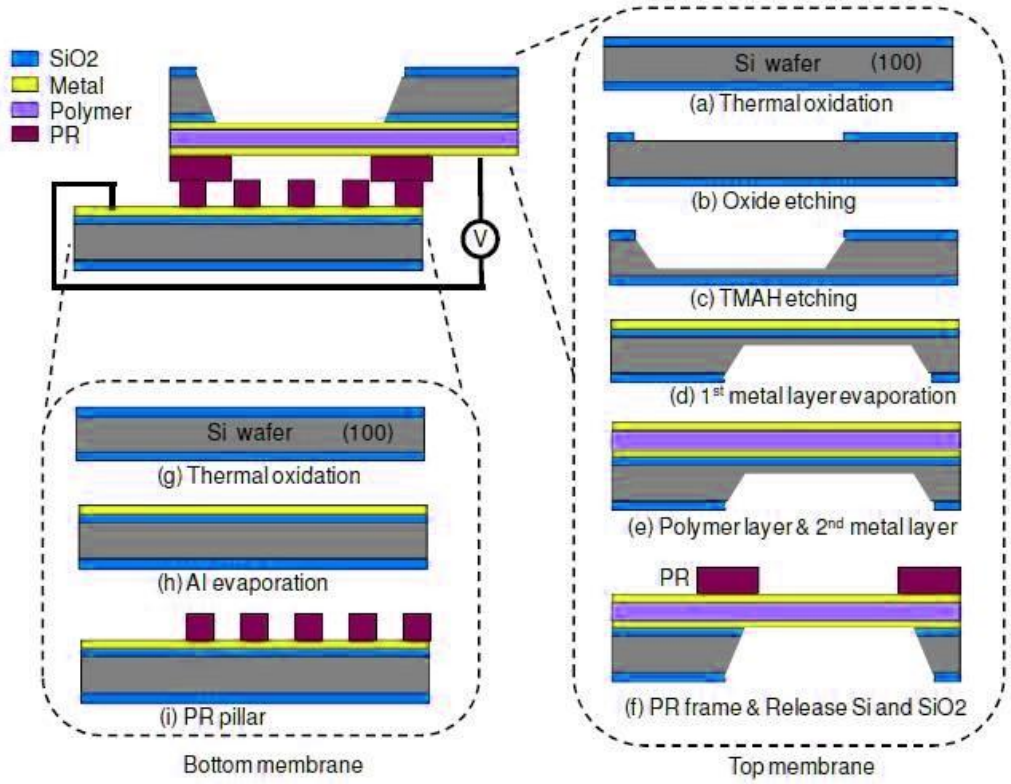

Figure 7-3 Device fabrication processes for a top polymer membrane and a bottom electrode.

A cross-section schematic drawing in Figure 7-4(a) shows a flat membrane surface without applied voltage. One can see the polyimide membrane is supported by a silicon frame. The PR defines the circular opening of the reflecting mirror surface. When a voltage is applied between the deformable membrane and the bottom electrode, the membrane is pulled down by electrostatic force and forms a curved surface to focus light, as in Figure 7-4(b). The PR pillars allow the air to flow out the gap without damping the motion of the polyimide membrane. Besides, they also prevent short circuit damages when the membrane is in touch with the bottom Al electrode. We also purposely sandwiched the polyimide layer with two aluminum layers so that the residual stress of metal layers are balanced out by this symmetric configuration. In

addition, the polyimide is all covered with metal layers, preventing it from in contact with oxygen and moisture in air. We found this increases the membrane reliability compared with only one side aluminum coating. A fabricated device is shown in Figure 7-4(c) where the bottom electrode is underneath the membrane and cannot be seen from this angle of view. The diced chip is 6.5 mm in width with a 3.5 mm square opening. The lower part of the diced chip is designed to be mounted on a package base later. The optical aperture of this MEMS DM is 3 mm because the photoresist define its deflection area as illustrated in Figure 7-3(f).

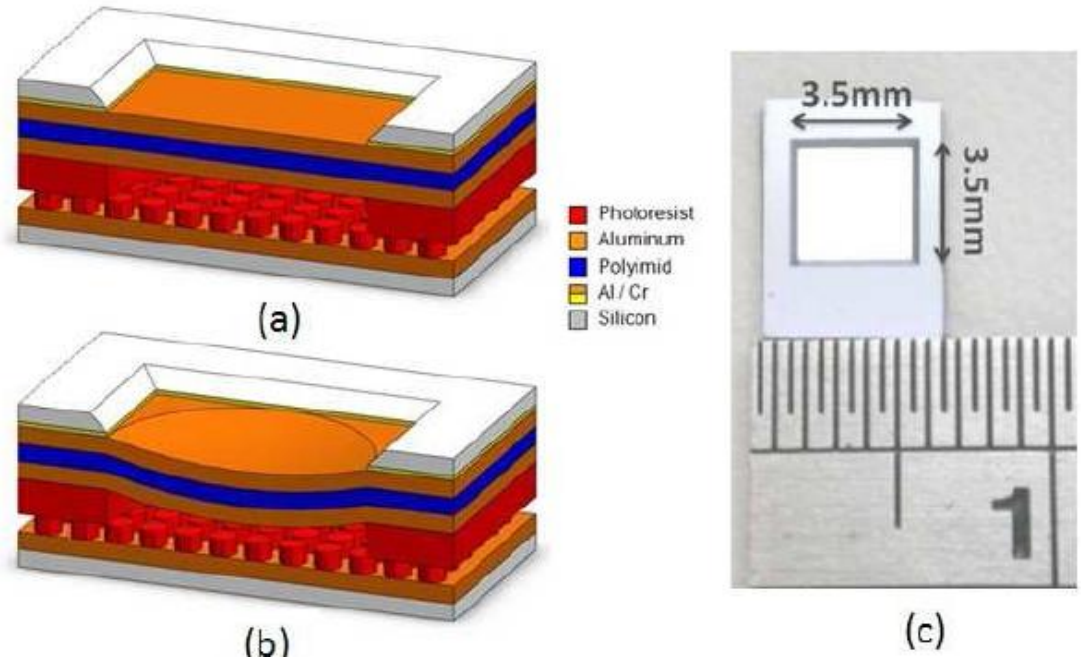

Figure 7-4 Schematic drawings and photos of a fabricated MEMS deformable mirror device.

We measured the center displacement versus applied voltage of the polymer MEMS DM. A DC-DC voltage amplifier circuit (From Matsusada Precision Inc.) is used to increase the input voltage from 15V to maximum 600V output. Although the

applied voltage is high, the power consuming is very low due to capacitor structure with negligible current (~nA statically). The optical power of the polymer DM is about reciprocal of half of the radius of curvature of the mirror surface. The diopter is calculated according to the first-order paraxial rays approximation [12], the radius of the curvature is calculated by the expression

$$P = \frac{16x}{D^2} \tag{1.12}$$

where P is the focusing power in unit of diopter (m^{-1}), D is diameter of the polymer membrane, and x is the deformation of the mirror from the center to the edge. The clear aperture is 3 mm in diameter and maximum center displacement is around 12 μm so the diopter is approximately 20 m^{-1} at 150V applied voltage. The experimental results are shown in Figure 7-5.

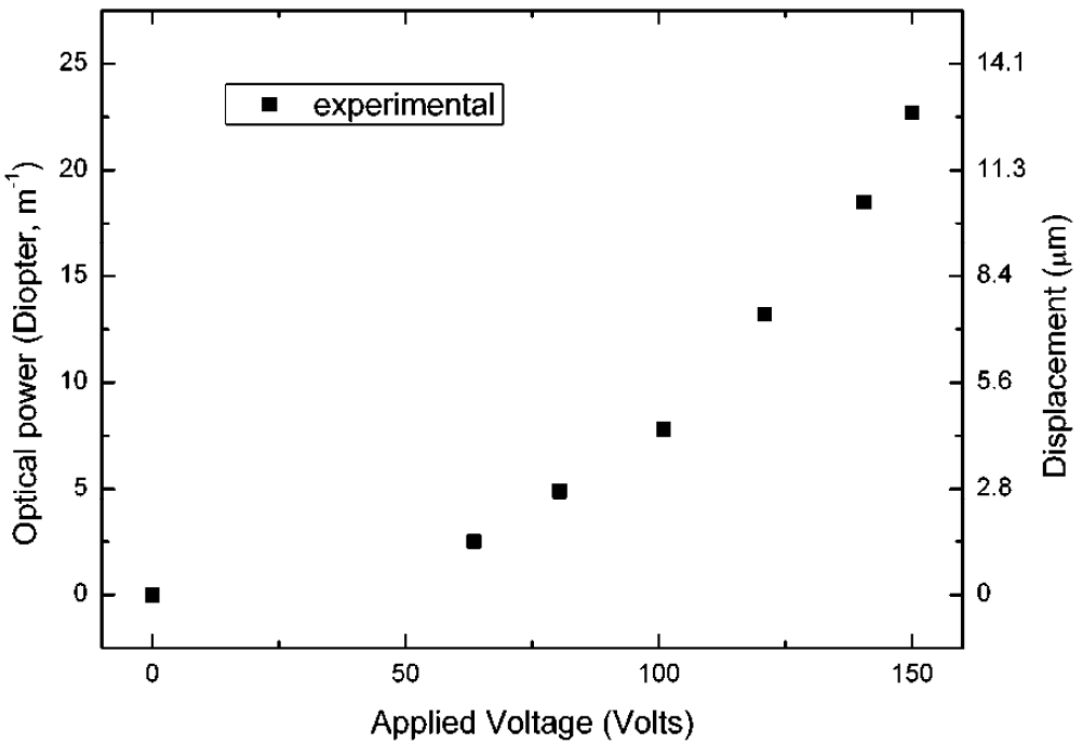

Figure 7-5 Diopter changes versus applied voltage of the polymer MEMS DM.

Figure 7-6 illustrates the 3D layout of an autofocus module consisting a MEMS deformable mirror. Unlike traditional camera systems that lenses are mounted on tubes in sequence, optical components are mounted in shapes of lollipop (e.g. solid lenses) or pillar (e.g. fixed mirror and deformable mirrors) in order to be mounted on the base, as shown in Figure 7-6. A cover is then placed on top of the base, and the cover is also used to block out auxiliary lights. The whole system will thus be approximately 6.7 mm in thickness, 11.5mm in length, and 10mm in height. Because the advantage of reflective optics is that lights can be folded within the system, the long total-track-length system can be realized in a thinner module. We believe that the imaging system can be even further miniaturized in near future with careful optimization.

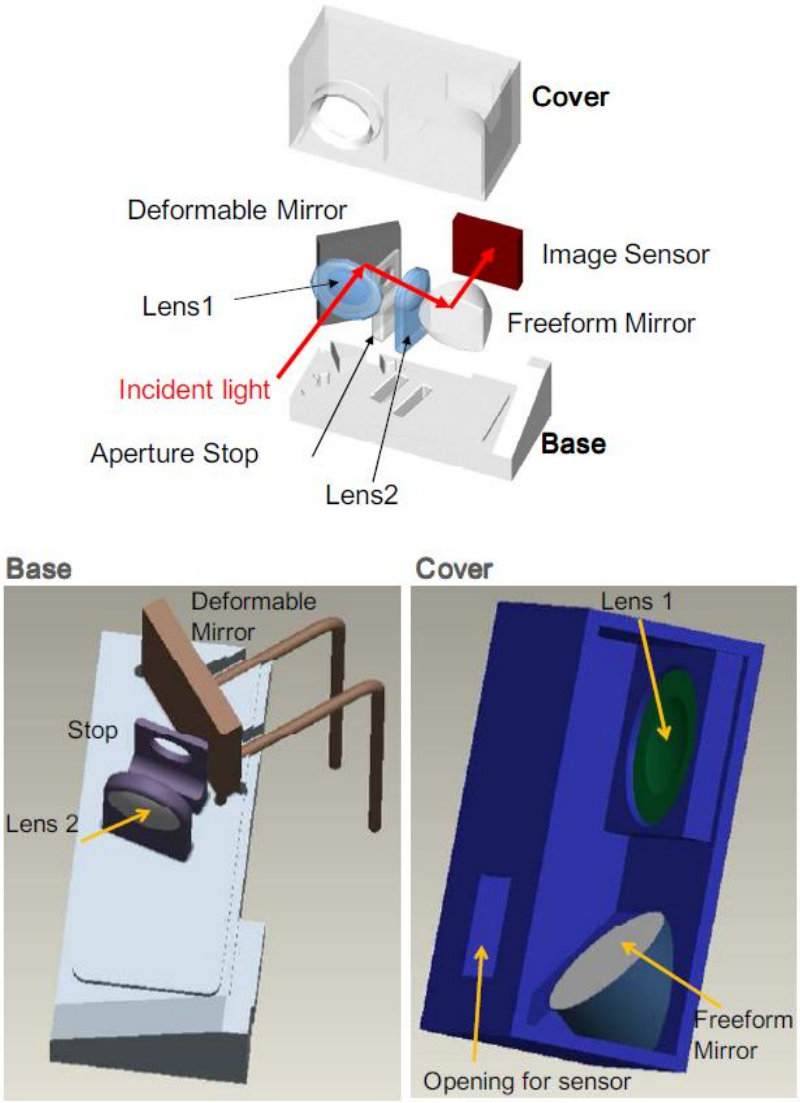

Figure 7-6 Assembly 3D drawings of an autofocus module

We used hot forming presses technology to manufacture solid lenses made of Arton, which is suitable for mass fabrication as well as MEMS deformable mirror. The free shape lens is manufactured by mechanical milling process. However, this part can be made by mode injection method in the future. Lens 1 and free shape mirror are mounted on the cover as in Figure 7-7(a), while lens 2, stop, and MEMS deformable mirror are plugged into the base shown in Figure 7-7(b). Traditional camera systems have lenses mounted on tubes for sliding, unlike ours that are vertically mounted on a flat base.

Optical components are formed in lollipop shape fixtures, such as Lens 2 in Figure 7-6 A module is completed when the cover is place on top of the base. This system is only 5.4 mm thick in optical lays out and 6.7 mm in thickness after package. The final assembled module is shown in Figure 7-7(c). The image sensor is not shown in this optical module because we used off-the-shelf image sensor which is not customized to our package.

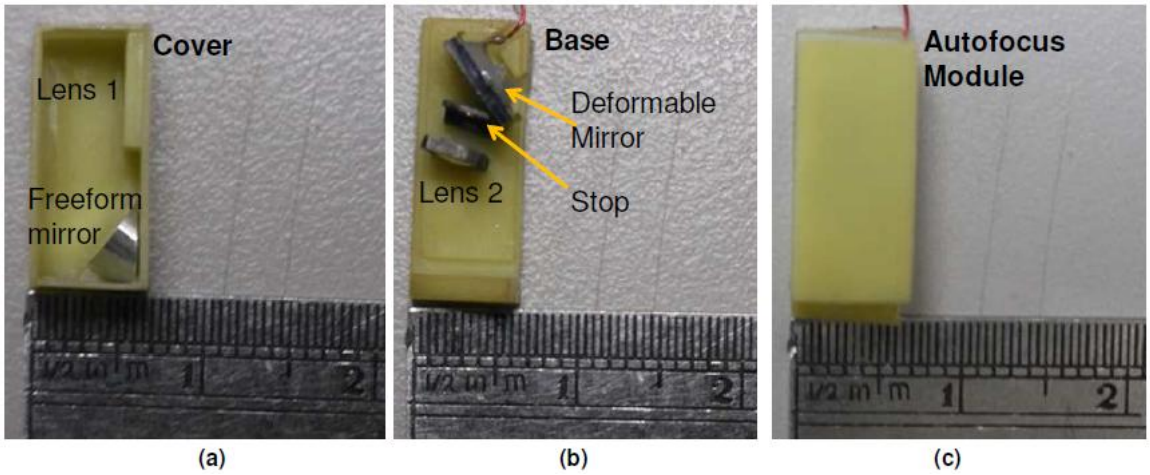

Figure 7-7 (a) Cover with a freeform mirror, (b) base with polymer MEMS DM and (c)final Assembly module.

7.4 Sharpness Function and Experiment Result

In order to realize the auto-focus function, it is very important to quantify the degree of clarity. There are many sharpness functions to calculate the clarity called focal value. The one we adopt is called Tenegrade method. From the simulation of image analysis, we can calculate the focal value changes with the optical power in a particular position. Figure 7-8(a) shows the focal value of image analysis simulation calculated by Tenegrade method. Red line with triangle is the focal value when object is in 500mm, and blue line with circle is the focal value when object is in 44 mm. We can observe that

it will focus on 550 mm with MEMS DM actuated and 44 mm without MEMS DM actuated. Combining focus-varying system and sharpness function, an auto-focus control system as shown in Figure 7-8(b) can be constructed with searching algorithm.

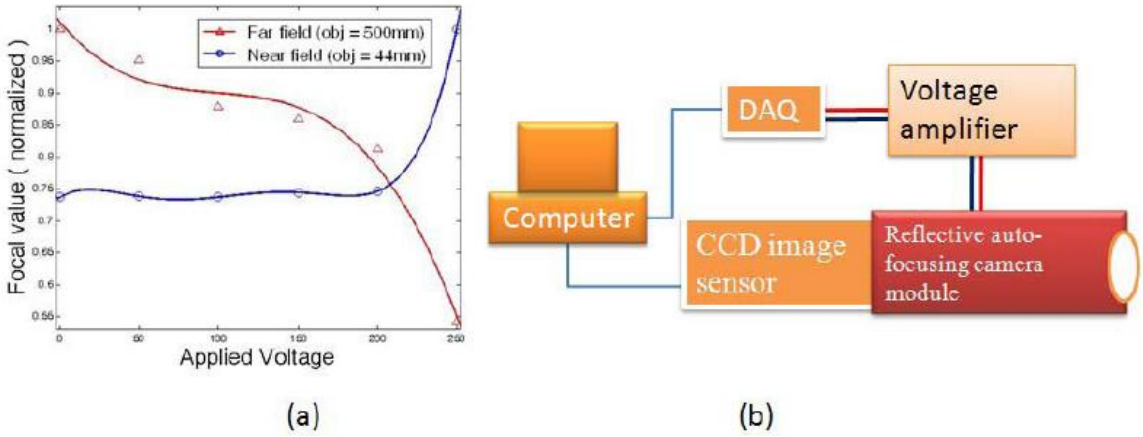

Figure 7-8 Pictures of near and far objects

Figure 7-9 shows the experimental results of optical auto-focusing function in this module. The incident light is within ± 26 degree, and focus is on a 6-mm-diameter-circle in the image plane. However, the size of 2M pixel sensors is 3.52 mm x 2.64 mm, which is covered within a 4.4-mm-diameter-circular. In other words, the edge of image circular is chopped due to the size of sensor. When object was placed in the far distance, the clear image happened without actuating the MEMS DM. The far object (~160 mm in distance, 80 mm in height) shows few Chinese characters and English words written as “made from natura”.On the other hand, when object was at the near distance (~78 mm in distance, 40 mm in height), the clear image happened when the polymer MEMS DM was actuated. Numbers, 6 and 3 can be seen clearly. In principle, the autofocus function is achieved in this module. The images, however, were not as sharp as we originally predicted. This may be due to no anti-reflection coating on the lenses surfaces, misalignment of each component and/or partially imperfect solid lenses. We believe that all of these can be improved for a commercial product.

Nevertheless, the concept of using MEMS deformable mirrors in a folded optical design can be realized in a thin package and demonstrated in the work.

Figure 7-9 Pictures of near and far objects

7.5 Conclusion

In this work, we have presented a innovative auto-focusing system featuring a reflective design form and an organic polymer membrane deformable mirror. As the simulation results shown above, it can peform the optical autofocus function without stepping motors and moving lenses. The over size of the packaged module is 6.7 mm in thickness, 11.5 mm in length, and 10 mm in height. The power consumption is low becuase the polymer MEMS DM is actuated by elecctrotstatic force. We will also work on system improvement and add zooming function in the future. The MEMS deformable mirror indeed has focus-varying function, and the optical image system we designed also provide the ability to focus on object in different distances. This work demonstrates that a MEMS deformable mirror and folded optical system design can form a thin optical module for imaging applications and mobile electronic devices.

References

[1] Hsin-Ta Hsieh, Design and fabrication of compact optical devices: organic deformable mirror and microlens arrays, published Phd dissertation, National Taiwan University, Taipei, Taiwan (2010).

[2] R. C. Gutierrez, T. K. Tang, R. Calvet, and E. R. Fossum, "MEMS digital camera," Proc. SPIE 6502, paper36, 1–8 (2007).

[3] S. Kuiper, and B. H. W. Hendriks, "Variable-focus liquid lens for miniature cameras," Appl. Phys. Lett. 85(7), 1128–1130 (2004).

[4] H. Ren, Y. Fan, S. Gauza, and S. Wu, "Tunable-Focus Cylindrical Liquid Crystal Lens," Jpn. J. Appl. Phys. 43(2), 652–653 (2004).

[5] J. L. Wang, T. Y. Chen, Y. H. Chien, and G. D. Su, "Miniature optical autofocus camera by micromachined fluoropolymer deformable mirror," Opt. Express 17(8), 6268–6274 (2009).

[6] D. Wick, "Active Optical Zoom System," US patent 6,977,777 (2005).

[7] W. Smith, Modern Optical Engineering: the design of optical systems, 2nd, (McGraw-Hill, 1990), pp.436.

[8] E. Hecht, Optics, 4nd (Addison Wesley, 2001).

[9] Boston Micromachines Corporation, http://www.bostonmicromachines.com/.

[10] V. T. Srikar, and S. M. Spearing, "Materials selection for microfabricated electrostatic actuators," Sens. Actuators A Phys. 102(3), 279–285 (2003).

[11] K. Seidl, J. Knobbe, and H. Grüger, "Design of an all-reflective unobscured optical-power zoom objective," Appl. Opt. 48(21), 4097–4107 (2009).

[12] J. Wang, T. Chen, C. Liu, C. Chiu, and G. Su, "Polymer Deformable Mirror for Optical Auto Focusing," ETRI Journal 29(6), 817–819 (2007).

Chapter 8 A Low Voltage Deformable Mirror using Ionic-conductive Polymer Metal Composite

Deformable mirror is a crucial component of adaptive optics. It can be used to vary the optical power of an optical image system, such as auto-focus and optical zoom function. An electrostatic type MEMS deformable mirror used in an optical image system has been promoted recently. However, high voltage in the range of hundreds volts is a serious concern for electrostatic type MEMS deformable mirror. Ionic-conductive polymer metal composite (IPMC) is a polymer actuator with the advantage of large deformation under low actuation voltage. It is a sandwich structure composed of two metal electrodes and a layer of polymer film. The hydrated cation inside the polymer film moves toward the cathode. Because of the migration of ions and water inside the film, volume expansion and contraction induce the deformation of IPMC. In this work, we design the IPMC type deformable mirror that is simulated by finite element method and then demonstrate its focus-varying function. It requires less than 5 volts to achieve 20 diopters.

8.1 Introduction

There are several methods to achieve auto focus function. These methods could be separated to two types, refractive and reflective types. Conventional camera module with moving lens sets is refractive type. It can change optical power using motors. However, it is volume and power consuming. Liquid lens reported by B. Berge et al. [1] is another solution of refractive type. It adopts a bi-liquid lens that can deform the shape of the interface between two immiscible liquids by the electro-wetting method to change its optical focusing power. However, the approach may suffer from some difficulties such as density variation with temperature, optical axis misalignment caused by gravity, and hand shaking. The other proposed solution is a reflective-type design, which adopts a MEMS deformable mirror (MEMS DM) to vary the optical power of the camera module. By changing the surface of a deformable mirror, the optical power of the module changes to designated degrees. MEMS DMs are made by rigid silicon-based materials [2-3] and their optical power adjustment capability is less than one diopter. This results in large optical layout space and is not suitable for mobile devices. Besides, the actuating voltage is reported up to 300 volts.

On the other hand, Ionic Polymer-Metal Composite (IPMC) is a promising alternative material to be used in fabricating DMs because of its ability to exhibit large bidirectional actuation with low applied voltage. IPMC is a sandwich structure composed of two layers of metals as electrodes and a layer of Nafion® inside. It can be used as an actuator or a transducer which was discovered by Oguro et al. [4] form the ion-exchange film of fuel cell. IPMC shows great potential for many applications, such as artificial muscles, robotic actuators, MEMS actuators, pressure sensors, micro pumps from micro to macro range of sizes because of it shows large deformation in the

presence of low applied voltage. There are several models that have proposed to describe the principle of IPMC's actuation: physical models and grey box models. Many researchers have built various physical models, or mathematical models, based on the fundamental mechanisms of IPMC which involved many deep physical parameters. However, it is too difficult to be applied on arbitrary shapes or patterns. So, the grey box models provide an easier way to reach the purposes. Grey box model consist of simple physical laws and use some parameters experimentally measured by curve fitting. There are several grey box models have been proposed. [5-6]

In this work, we discuss about reflective-type deformable mirror designs using IPMC, which has the advantage of high deformation with low actuation voltage, by Finite Element Method (FEM) simulations. The principle of IPMC would be introduced at first. Then the FEM model of IPMC in cantilever beam shape would be discussed. The grey box model is simplified to a double-virtual layers Nafion® cantilever beam with metal layers outside. One of the beams is contractive and another is expansive. The actuation force is equalized to normal surface compressive and tensile pressures on each surface of elements. This model is combined with important physical properties of IPMC: Young's modulus and poisson's ratio. Although the physical properties are quite difficult to determine experimentally due to the complexity of the morphology of IPMC, for the needs of further designs, we chose the physical properties of metal and Nafion® separately for which was reported by Jiang Yu Li et al. [7] The voltage-deformation experiment data shows the agreement with the FEM model. Finally, we propose a deformable mirror design in simulation which would manipulate the optical power to achieve the focus varying function.

8.2 Principle of IPMC

Ionic polymer-metal composite (IPMC) is a sandwich structure composed of two layer of metals as electrodes and a layer of Nafion® inside. Figure 8-1(a) shows the schematics of the electro-osmotic migration of hydrated counter-ions within the IPMC network. Figure 8-1(b) shows the molecular formula of Nafion® corresponding to Figure 8-1(a). Nafion® can be separated into two chains. The main chain builds the backbones to determine the mechanical strength and the side chain terminated by ionic groups, e.g., SO_3^- for cation exchange. Main chain is hydrophobic and side chain is hydrophilic, the chains form cluster networks (or nano-channels) with side chain inside. So, the hydrated cations, or hydrated alkali metal molecular typically sodium, can transport in the hydrophilic cluster networks. The underlying principle of actuation for IPMC is that when the electric field is applied, the hydrated cations move through clusters toward cathode so the volume will expand near cathode side and contract near anode side. Finally the IPMC will bend toward anode.

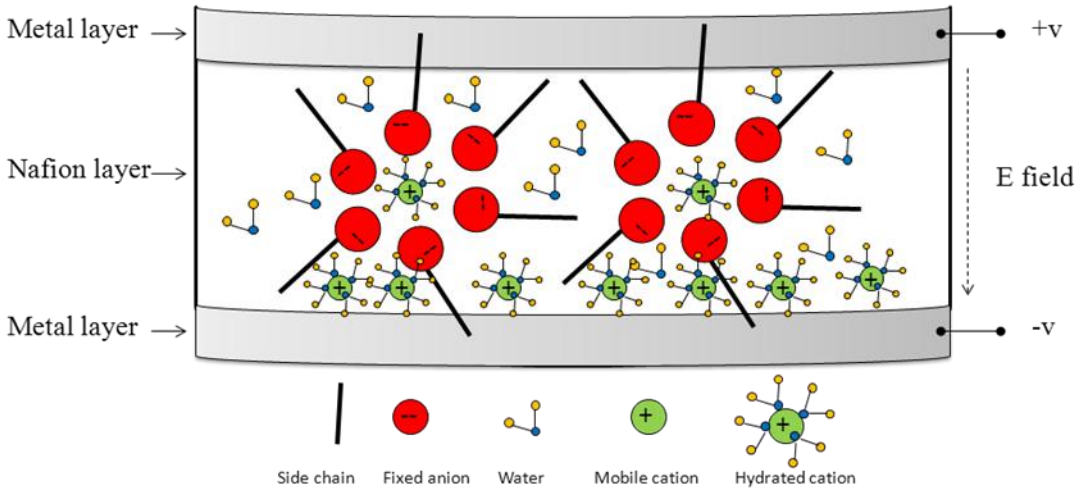

(a)

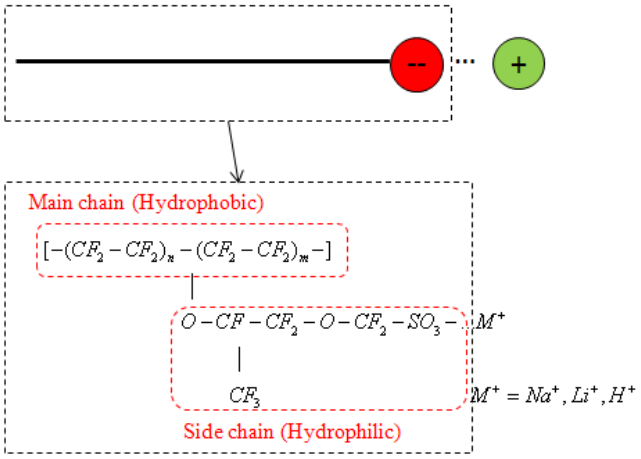

(b)

Figure 8-1 The schematics of the IPMC network and (b) the molecular formula of Nafion.

8.3 FEM simulation model of cantilever beam

According to the actuation mechanisms, the real actuation force should be symmetric distributed inside IPMC in the manner of positive stress linear increasing from neutral surface and negative stress to opposite direction. The stress fields would cause the bending moment. In our FEM simulation model, we assumed a simplified stress field distributed gray box model that there are only two constant stresses, one is

positive, or compressive, and another is negative, or tensile. Figure 8-2 shows this simplified stress field distributed model which would be implied to the FEM model. The total thickness is 2h and M_e denotes the bending moment caused by the internal stress. Figure 8-3 shows the structural model in ANSYS® . The IPMC could be divided to four parts, two layers of metallic electrodes, a layer of Nafion® with constant compressive surface force, and a layer of Nafion® with constant tensile surface force. Figure 8-4 shows the element model in ANSYS® . The red arrow depict that the compressive surface force on upper Nafion® elements, and blue arrow depict that the tensile surface force on lower Nafion® elements. All the stresses are applied normal to the element surface. The element type used in ANSYS® is SOLID45. The physical properties are as follows: Young's modulus for platinum is 168GPa, and for Nafion® is 275MPa. Poisson's ratio for platinum is 0.38, and for Nafion® is 0.487. All the physical parameters are listed in Table 8-1.

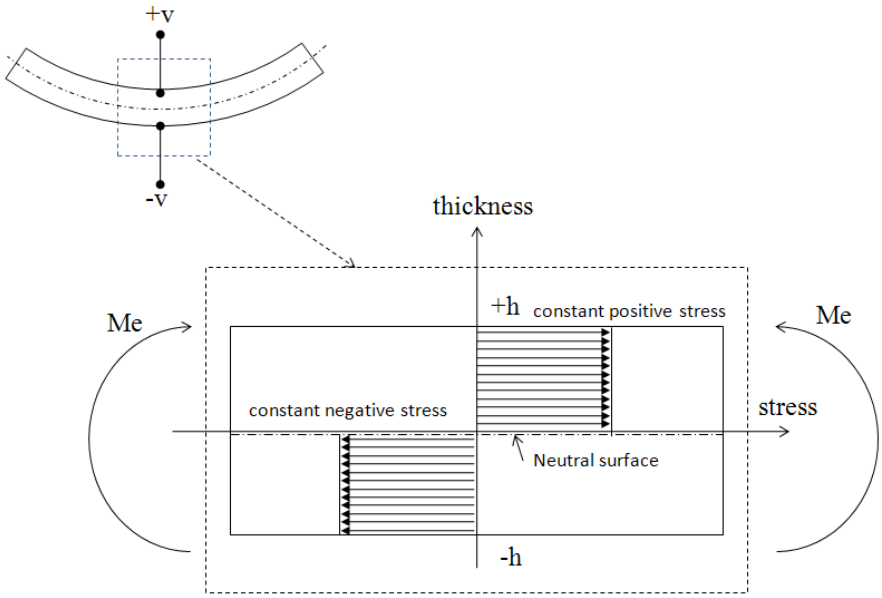

Figure 8-2 The simplified model with constant stress field which would be implied to the FEM model.

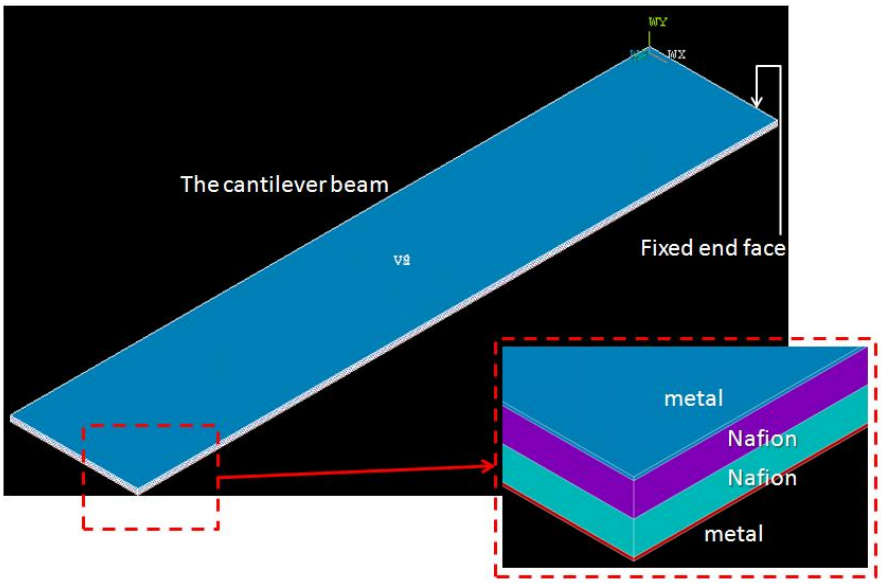

Figure 8-3 ANSYS® structure model of IPMC

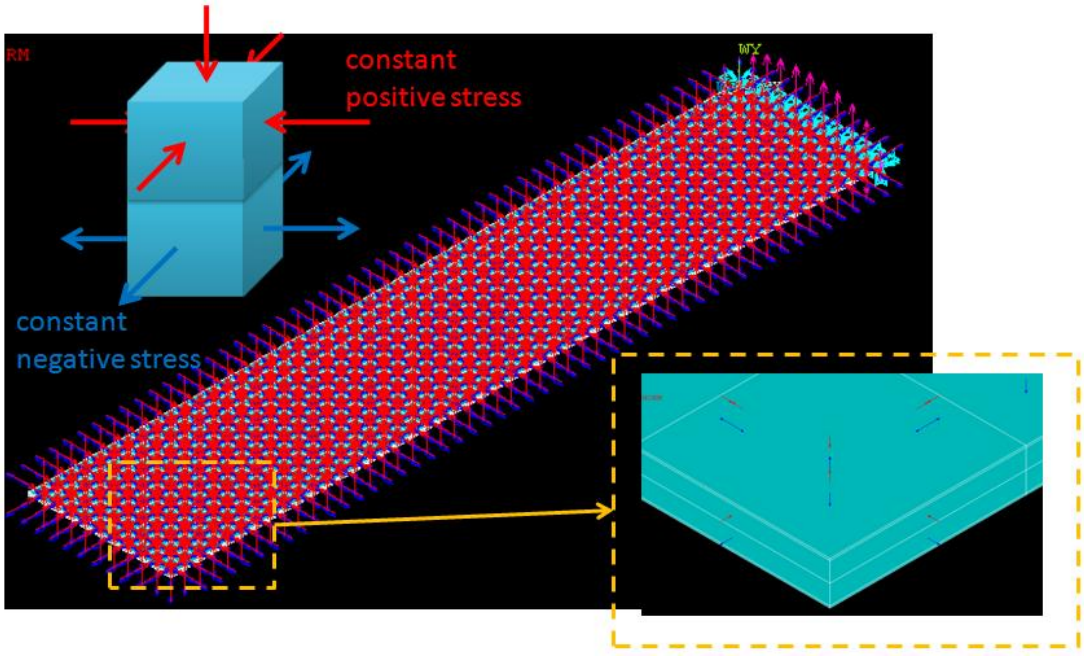

Figure 8-4 ANSYS® element model of IPMC

Table 8-1 Physical parameters of different materials

	Young's modulus	Poisson's ratio
Platinum	168GPa	0.38
Nafion® [7]	275MPa	0.487

From the FEM simulation which varied the length (L) and width (w) of IPMC and the half thickness (h) of Nafion® with constant surface force (P = 100 Pa), as shown in Figure 8-5, we could express the relation of surface force with tip displacement as follows

$$s_{ansys} \cong c_1 L^2 h^{-1} \cdot P \tag{1.13}$$

Where S_{ansys} is the simulated tip displacement, L is length, h is half thickness of Nafion, and P is the surface force, C_1 is a constant number. Then, compare with the result from Sia Nemat-Nasser et al., we could derive the relation of the surface force, which is the assumed virtual constant stress in our simplified FEM model, with small applied voltages.

$$P = {c_2}/{h} \cdot \phi_0 \tag{1.14}$$

Where φ_0 is the applied voltage and C_2 is constant which depends on the characteristic of Nafion® . This reveals that the surface force just depends on the thickness with applied voltage. For different process conditions, the characteristic of Nafion® is different, and then the constant C_2 is different too. According to equation (1.14), we can simulate the deformation profile of arbitrary shaped IPMC with given boundary confinement or given applied voltage.

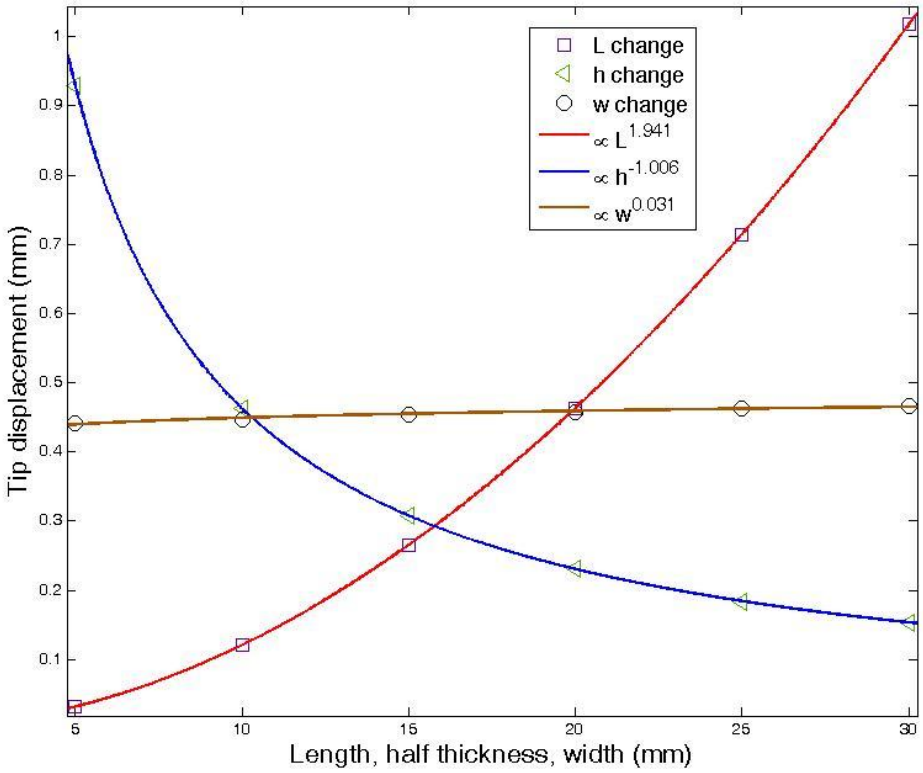

Figure 8-5 FEM simulation which varied the length (L) and width (w) of IPMC and the half thickness (h) of Nafion with constant surface force (P = 100 Pa)

8.4 Simulation model and experimental verification

We first simulate the cantilever beam with two side confinement and compare it with experimental result qualitatively. Figure 8-6(a) is the simulation result and (b) is

the experimental result. It reveals that the deformation shape is almost along sagittal direction rather than along tangential direction, which is very different from one side confinement cantilever. These results suggest that our simplified model can predict the deformation shape of IPMC qualitatively. According to this result, the simplified model is suitable for three dimensional (3-D) deformation profile analysis and prediction.

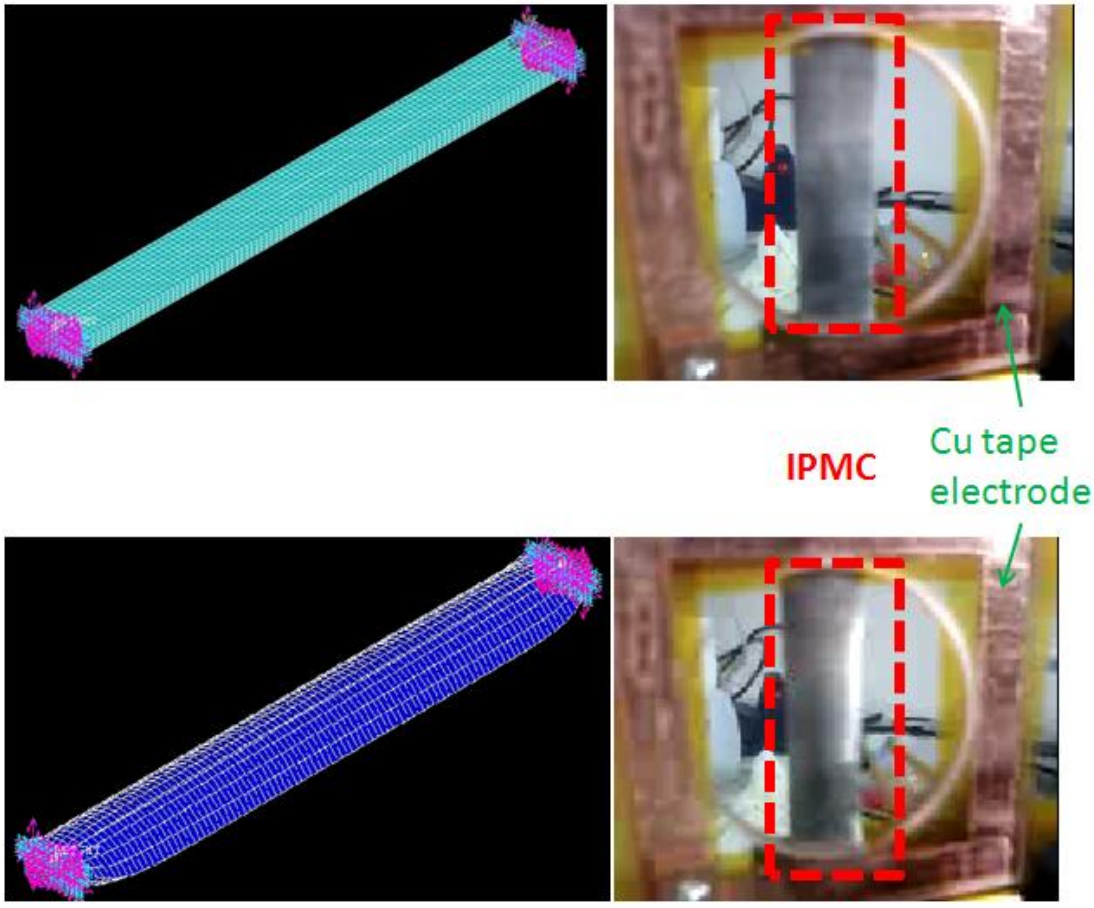

(a) (b)

Figure 8-6 Deformation shape of double side confinement. (a) simulation (b) experiment. (These figures show IPMC with and without applied voltage)

To find out the exact model to predict IPMC deformation quantitatively, we need to find out a tip displacement of a one-side confinement cantilever. In this experiment, we use the result of voltage - tip displacement result to determine the constant, C_2, of

equation (2) by curve fitting. As discussed in the last section, the constant depends on different IPMCs for different process conditions. Figure 8-7 shows the experimental result and simulation result. In this experiment, length and width are 20 mm and 5 mm. Thickness of platinum and Nafion® are 10 μm and 200 μm, respectively. Based on the curve fitting, the constant, C2, is determined to be 60000 (Pa*m/V). This constant would be used for further ANSYS® simulation with arbitrary shape designs.

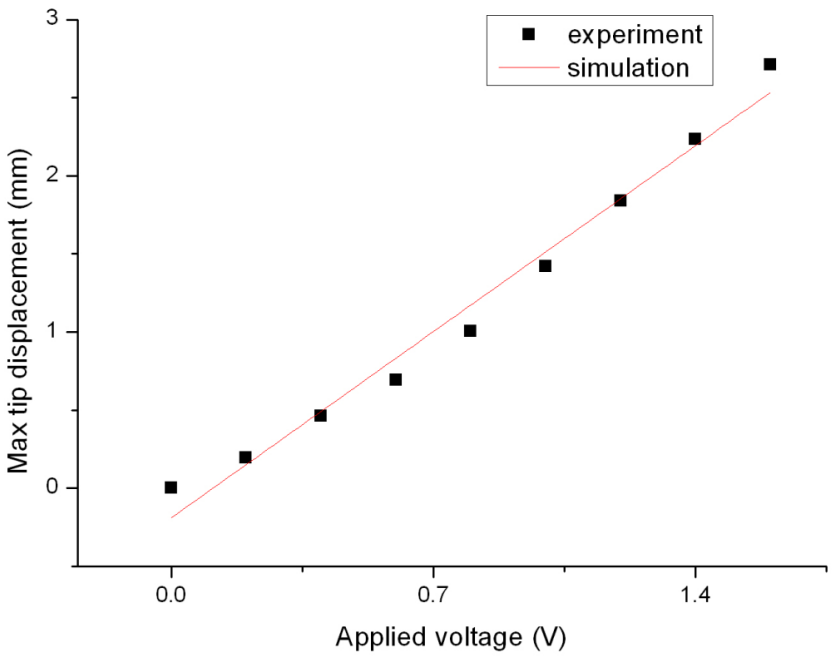

Figure 8-7 The black dots are experimental results of tip displacement vs. applied voltage. And the solid line is simulation result by curve fitting, where C2 is 60000 (Pa*m/V).

8.5 Gear shaped IPMC and experimental result

A new deformable mirror with gear-shape IPMC design was presented in this work, as shown in Figure 8-8. There were three fixed arms and a free mirror at center. The

mirror was 12 mm in radius, the length and the width of the fixed arm was 8 mm and 4 mm, and the thickness of metal and half thickness of Nafion® were 10 μm and 100 μm accordingly. There are four major steps to make IPMC actuators: (a) ion exchange polymer (often called ionomer) formation and pre-process; (b) initial compositing; (c) surface electrode growing; (d) shape cutting. The first step is to make a sheet of ion exchange polymer, which could be found in commercial Nafion® film (DuPont, USA). The pre-process includes acid cleaning, surface roughening, and soaking in the salt solution. The roughening increases the effective area of Nafion® to hold the metal layer. The salt solution is $Pt(NH_3)_4HCl$, which would diffuse platinum-containing positive ions into the inner surface of the ion exchange polymer via ion exchange process. Additionally, the initial compositing processes buries sparsely distributed metallic particles in the inner surface of the ion exchange polymer by electroless-plating method to form a layer of metallic particle foundation for the third step. The primary reaction is

$$NaBH_4 + 4[Pt(NH_3)]^{2+} + 8OH^- \Rightarrow 4Pt^0 + 16NH_3 + NaBO_2 + 6H_2O \quad (2).$$

The highly dispersed metallic particulate layer was buried a few microns deep under the interface boundaries. Typically the reducing agent is $NaBH_4$. Surface electrode grows the metallic particles smoothly on both side surfaces of the IPMC using stronger reducing agent. The surface resistivity becomes greatly reduced. Finally, the IPMC sheet was completed and can be cut to gear shape. We then soaked it in an appropriate salt solution, such as NaOH, to contain counter-ions. Figure 8-9 shows the fabrication process of the gear-shape IPMC deformable mirror.

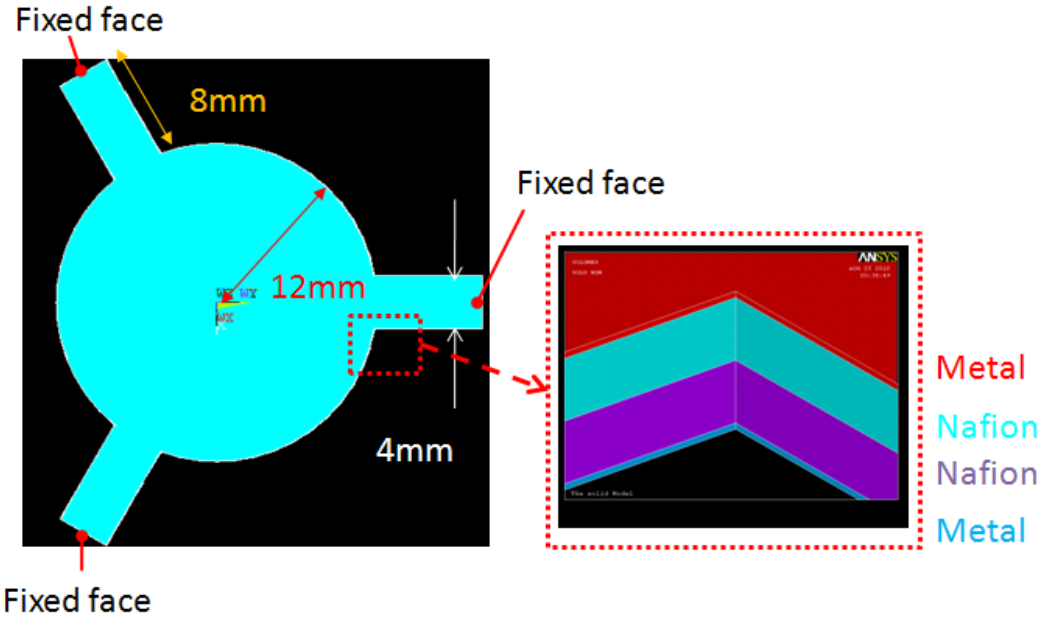

Figure 8-8 The gear shaped IPMC design.

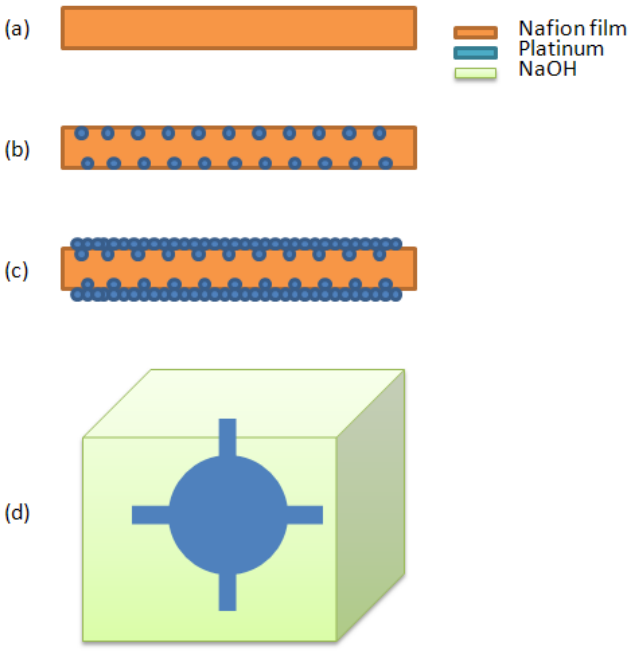

Figure 8-9 The IPMC process flow.(a) ion exchange polymer formation and pre-process; (b) initial compositing; (c) surface electrode growing;(d) shape cutting.

Figure 8-10(a) is the picture of the fabricated IPMC deformable mirror. The central displacement is about 0.6 mm and the corresponding optical power is about 17 diopters (m^{-1}) under two volts. Figure 8-10(b) shows the deformation simulated by ANSYS®. The experimental result of a reflected laser spot by flat and curved IPMC DM is shown in Figure 7. Because of the diffused metal particles caused by surface roughening, the laser spot was somewhat scattered and was focused approximately 6 cm from the DM. The corresponding optical power is approximately 17 diopters. Compared with flat IPMC mirror, the actuated IPMC mirror focus 50% more energy in the 2 mm diameter. In other words, the collimated light was focused successfully. Figure 8-11 illustrates the intensity profile of the laser spot reflected by the non-actuated IPMC (non-focused) and the actuated IPMC (focused). The surface profile using white light interferometer (WLILab, BMT Group) is shown in Figure 8-12. The root-mean-square roughness is 1.37 μm. We believe the surface roughness can be further improved by modifying fabrication processes in future. All these experimental results demonstrated that the gear shaped IPMC DM has suitable optical focusing power and needs much lower voltage than other techniques, such as liquid lens and micromachining electrostatic deformable mirrors. The liquid lens needs 60 volts to achieve ±15 diopters and micromachining electrostatic deformable mirrors require 160 volts for 20 diopters. The comparison of these techniques is shown in table 2.

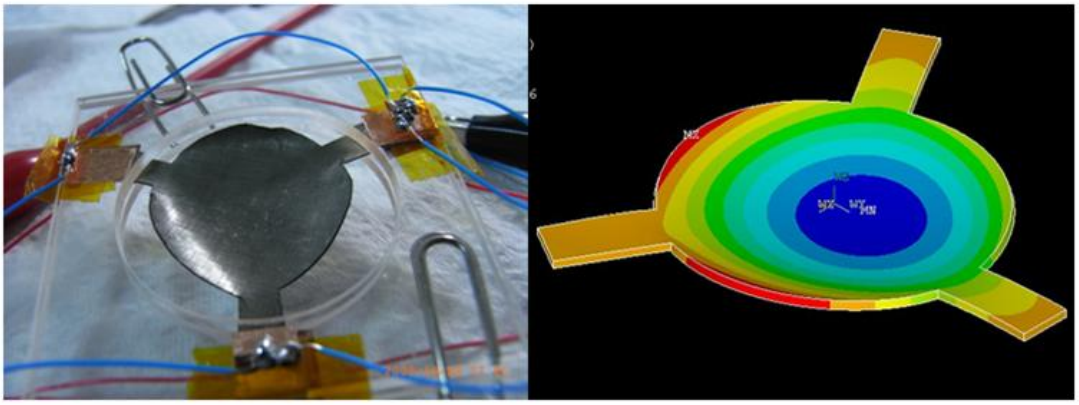

(a) (b)

Figure 8-10 (a) The Picture of experimental demonstration of the new deformable mirror. (b) The deformation simulated by ANSYS® .

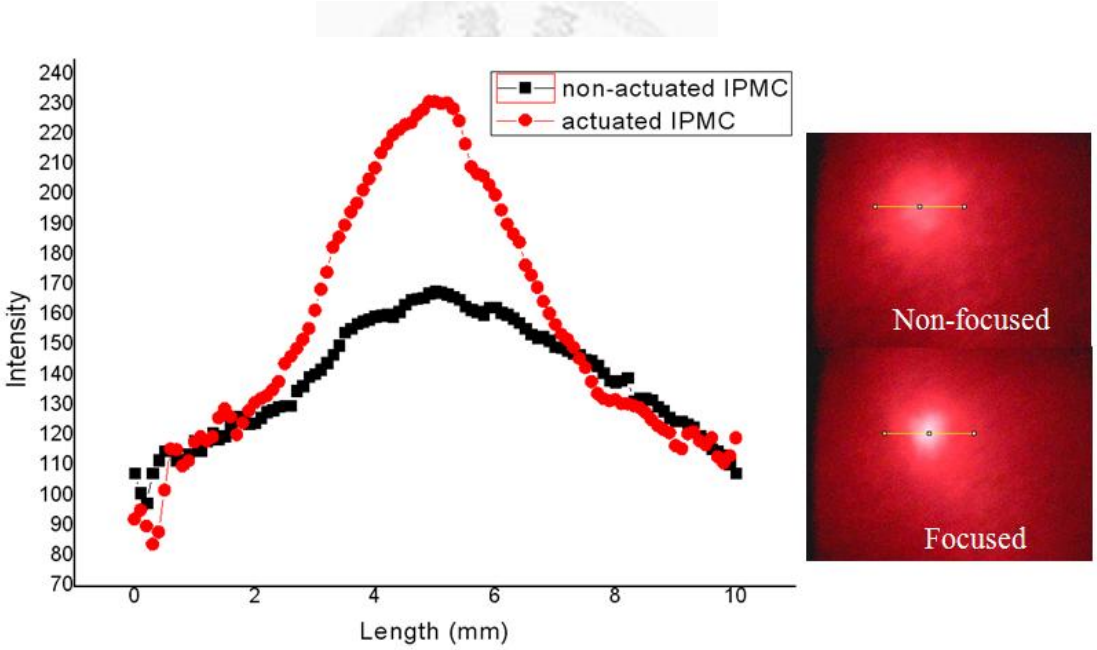

Figure 8-11 The intensity profile of the laser beam spot with non-actuated IPMC (non-focused) and actuated IPMC (focused).

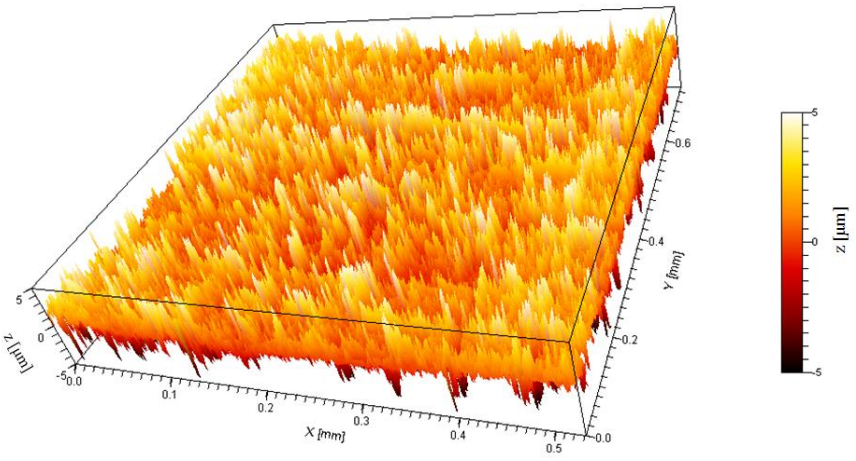

Figure 8-12 The surface profile using white light interferometer.

Table 8-2 The comparison of different technologies.

	Liquid lens [1]	**Liquid crystal lens [2]**	**MEMS deformable mirror [4]**	**IPMC deformable mirror (exp)**
Color dispersion	Yes	Yes	No	No
Applied voltage	60 V	5 V	160 V	2 V (lowest)
Max optical power	±15 diopter	± 5diopter	20 diopter	±17 diopter
Other issues	• Gravity problem; • Temperature	• Additional AC circuit ; • temperature; • polarizer needed	• High applied voltage	

8.6 SUMMARY

In this work, we used a convenient box model based on the finite element method to simulate the deformation of the gear shaped IPMC. The gear shaped IPMC provides a surface pull down motion which was different from the conventional cantilever bending motion. The simulation model considers the mechanical properties of Nafion® and

metal, including Young's Modulus and Poisson's ratio. There is a constant which depends on the process of IPMC. Therefore, a cantilever beam shaped IPMC should be manufactured and measured first to determine the constant by the experiment of tip displacement versus applied voltage. The three-dimensional deformation of the IPMC actuator can be predicted much more easily. Because of the diffused metal particles caused by surface roughening, the laser spot is somewhat scattered. The focused light spot was approximately 6 cm from the DM. The corresponding optical power is about 17 diopter with two volts applied.

References

[1] B. Berge, "Liquid lens technology: Principle of electrowetting based lenses and applications to imaging," in *Proc. IEEE Int. Conf. Micro Electro Mech. Syst. MEMS*, Miami Beach, FL, United states, 2005, pp. 227-230.

[2] T. Bifano, *et al.*, "Micromachined deformable mirrors for adaptive optics," in *Proc SPIE Int Soc Opt Eng*, Seattle, WA, United states, 2002, pp. 10-13.

[3] G. Vdovin and P. M. Sarro, "Flexible mirror micromachined in silicon," *Appl Opt*, vol. 34, pp. 2968-2968, 1995.

[4] K. Oguro, *et al.*, "Polymer film actuator driven by a low voltage," in *Proceedings of 4th International Symposium on Micro Machine and Human Science at Nagoya*, 1993, pp. 39-40.

[5] P. De Gennes, *et al.*, "Mechanoelectric effects in ionic gels," *Europhysics Letters*, vol. 50, pp. 513-518, 2000.

[6] R. Kanno, *et al.*, "Linear approximate dynamic model of ICPF (ionic conducting polymer gel film) actuator," in *Proceedings of the 1996 13th IEEE International Conference on Robotics and Automation. Part 1 (of 4), April 22, 1996 - April 28, 1996*, Minneapolis, MN, USA, 1996, pp. 219-225.

[7] J. Li and S. Nemat-Nasser, "Micromechanical analysis of ionic clustering in Nafion perfluorinated membrane," *Mechanics of materials*, vol. 32, pp. 303-314, 2000.

[8] H.-T. Hsieh, *et al.*, "Thin autofocus camera module by a large-stroke micromachined deformable mirror," *Opt. Express*, vol. 18, pp. 11097-11104, 2010.

Chapter 9 Conclusions and Future Work

In the previous chapters, we showed the design, fabrication, and applications of microlens array (MLA) and deformable mirror (DM). There were two methods involved to fabricate MLA, self-assembled by using hydrophilic effect and double layer of long focal length by using thermal reflow method. According to the advantages of the different techniques, the applications of light emitting diode (LED) improvement and Shack-Hartmann wavefront sensor were demonstrated successfully. Regarding to the DM, we built an autofocus camera module including optical system design and autofocus algorithm. We also design a low voltage DM by using IPMC.

9.1 Dissertation conclusions

9.1.1 Microlens arrays

A transparent and self-assembled MLAs fabricated by use of the hydrophilic effect under UV/ozone treatment was presented and demonstrated experimentally. The MLA was made of negative photoresist SU-8 (n=1.63 @ 530 nm) on a glass substrate. The focal length of MLA is controllable by changing UV/ozone treatment time. A larger shadow mask opening and a longer UV/ozone treatment time produced MLA with longer focal length. MLAs of 50 μm, 100 μm, 200 μm diameters for one, two, three, and four minutes UV/ozone treatment time has been fabricated successfully. The numerical apertures of microlens were from 0.06 to 0.19. The focal lengths were from 0.06 mm to 2.78 mm. The surface roughness was less than 0.07 μm and the shape was nearly spherical. The yield rate was higher than 96 %. The corresponding PV and RMS values of wavefront were lower than 0.949 λ and 0.143 λ. MLA of 100 μm via electric field of

1.7 V/μm and 3.4 V/μm has been fabricated successfully. The external electric field not only increases the optical power but also makes the surface roughness smaller. The focal lengths of microlens were varied from 0.09 mm to 2.91 mm. The surface roughness was less than 70 nm and became better under larger electric field pulling. The shape of a microlens was nearly spherical. We verify that this method provides a fast, low cost, no etch-transfer and room temperature fabrication process.

A transparent and self-assembled microlens on the top of LED fabricated by using hydrophilic effect under UV/ozone treatment was presented. The LED chips were encapsulated by a layer of thick PDMS (n = 1.44). The high refractive index material of PDMS and SU-8 photoresist and the microlens on the top of LED improved the extraction efficiency of 15 % and 28% in maximum and total accordingly, and increased the viewing angle of 17 degree.

The fabricated double layer MLAs were compatible with a CMOS image sensor in constructing wavefront sensors. The wavefront measurement accuracy of our wavefront sensor was evaluated by a comparative measurement using a commercial wavefront sensor, which was less than λ/25 in RMS difference. The wavefront measurement result verifies that the long focal length MLA has higher accuracy and sensitivity and its RMS is λ/20 better than that of the shorter focal length MLA.

9.1.2 Deformable mirrors

An auto-focusing camera system with a MEMS deformable mirror was demonstrated to adjust the optical power of the whole system. The deformable mirror can provide 20 diopters of focusing capability, which is one order of magnitude higher than current commercial products. In order to optimize the optical performance of the MEMS deformable mirror and control it accurately, the optical properties of the

deformable mirror were taken into consideration. The auto-focusing method was explained, and it includes the Tenengrad method and a percentage-drop searching algorithm. Accuracy and time issues were also discussed. Finally, we demonstrated the experimental setup and the experimental results of this auto-focusing system. A searching time 45% faster than a global search was achieved. As a result, an innovative auto-focusing camera system has been successfully demonstrated.

We used a convenient grey box model based on the finite element method (FEM) to simulate the deformation of the gear shaped IPMC. The gear shaped IPMC provides a surface pull down motion which was different from the conventional cantilever bending motion. The three-dimensional deformation of the IPMC actuator can be predicted much more easily by the simplified grey box model and FEM software, ANSYS®. Because of the diffused metal particles caused by surface roughening, the laser spot is somewhat scattered. The focused light spot was approximately 6 cm from the DM. The corresponding optical power is about 17 diopter with two volts applied.

9.2 Suggestions for future work

The suggestions for future work are listed below:

1. The focus microlens on LED by using thicker PDMS.
2. The microlens application on concentrated solar cell.
3. The improvement of surface roughness for IPMC DM by the use of PDMS buffered layer.

9.2.1 The focus microlens on LED by using thicker PDMS.

The thickness of PDMS encapsulant can be used to define the distance between the microlens and the LED chip. If the distance is shorter than focal length of microlens, the

light beam from LED ship point source diverge. On the other hand, if the distance is longer than focal length of microlens, the light beam from LED ship point source converge. The principle is shown in Figure 9-1.

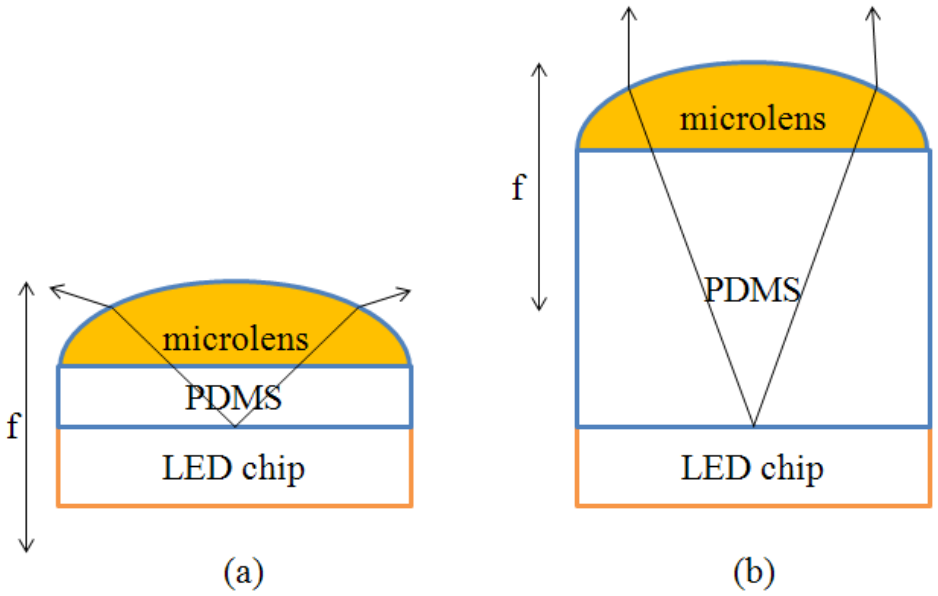

Figure 9-1 The principle of the LED light beam manipulation by using PDMS thickness.

9.2.2 The microlens application on concentrated solar cell.

The large amount of solar cell is expensive. By adding the optical system to concentrate sunlight to the solar cell, the need for solar cell reduces to a small area now. It saves the cost because optical system is much cheaper than solar cell. We could apply the self-assembled microlens array to the high concentrated photovoltaic (HCPV) fabrication as shown in Figure 9-2.

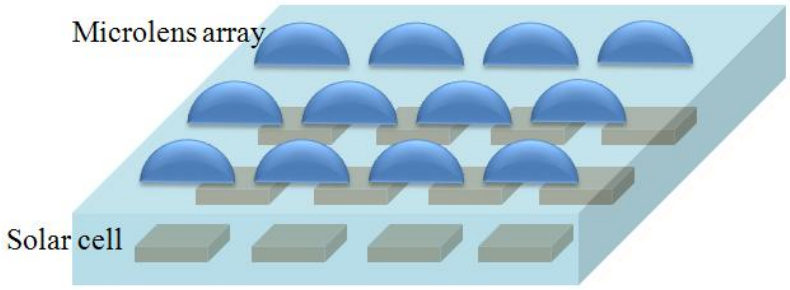

Figure 9-2 The small lens array with triangular prism model

9.2.3 The improvement of surface roughness for IPMC DM by the use of PDMS buffered layer

The surface roughness of IPMC is a serious concern of the application of DM. There have been many methods to reduce the surface resistance, which also lead to smoother surface, such as electroplating and physical metal evaporation. However, these methods cannot reach the need for optical application. The PDMS has the potential to be served as a buffered layer to improve the surface roughness as shown in Figure 9-3 and Figure 9-4.

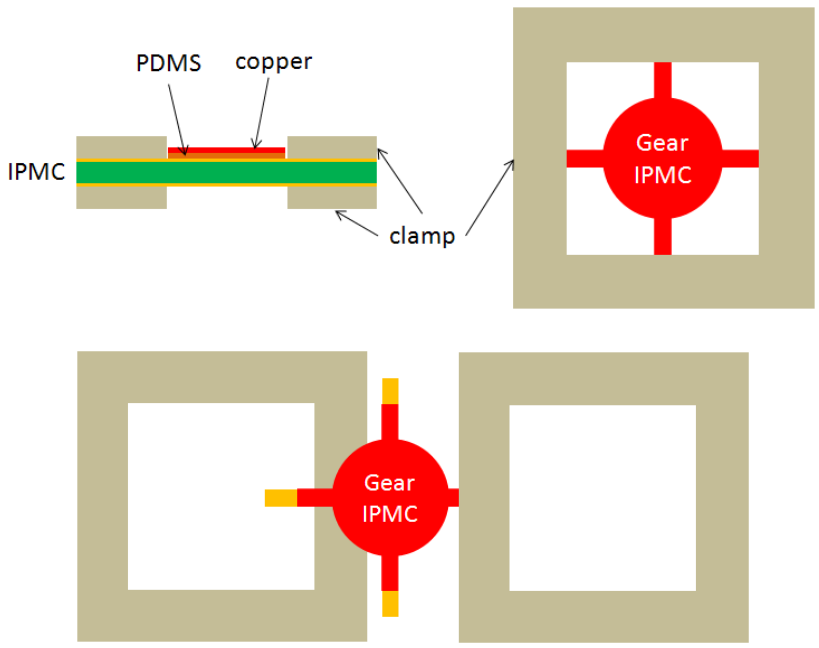

Figure 9-3 IPMC DM with PDMS buffered layer.

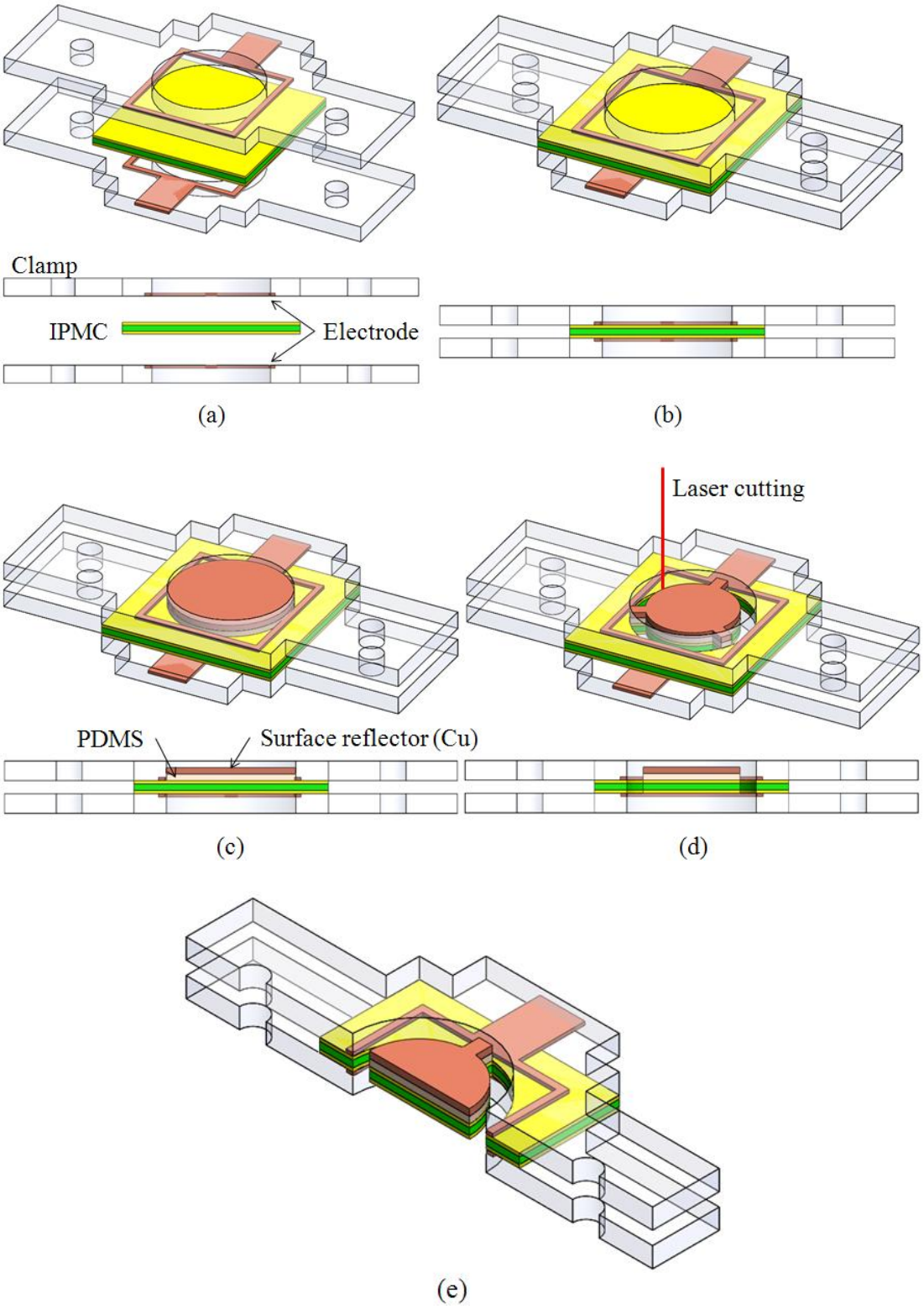

Figure 9-4 Fabrication principle of IPMC DM with PDMS buffered layer. (a) IPMC sheet(b) clamped by frames (c) spin PDMS and coat copper reflector (d) laser cutting (e) the section of PDMS modified gear shaped IPMC DM.

Publication List

Journal Papers:

1. **H. C. Wei** and G. D. J. Su, " Self-assembled Microlens on Top of Light Emitting Diodes using Hydrophilic Effect for Improving Extraction Efficiency and Increasing Viewing Angle," *Journal of Display Technology (submitted 2011,12,)*
2. **H. C. Wei** and G. D. J. Su, "Fabrication of transparent and self-assembled microlens array using hydrophilic effect and electric fielding pulling," *Journal of Micromechanics and Microengineering. (accepted* 2011, 11, 25)
3. **H. Wei** and G. Su, "Using Hydrophilic Effect to Fabricate Self-Assembled Microlens Array by UV/ozone Modification," *Photonics Technology Letters, IEEE,* vol. PP, pp. 1-1, 2011.
4. **H. C. Wei**, Y. H. Chien, W. Y. Hsu, Y. C. Cheng, and G. D. J. Su, "Controlling a MEMS Deformable Mirror in a Miniature Auto-Focusing Imaging System," , *IEEE Transactions on Control Systems Technology,* vol. PP, pp. 1-5, 2011.
5. V. Lin, **H.-C. Wei**, H.-T. Hsieh, and G.-D. J. Su, "An Optical Wavefront Sensor Based on a Double Layer Microlens Array," *Sensors,* vol. 11, pp. 10293-10307, 2011.
6. V. Lin, **H. C. Wei**, H. T. Hsieh, J. L. Hsieh, and G. D. Su, "Design and fabrication of long-focal-length microlens arrays for Shack-Hartmann wavefront sensors," *Micro & Nano Letters, IET,* vol. 6, pp. 523-526, 2011.
7. H.-T. Hsieh, **H.-C. Wei**, M.-H. Lin, W.-Y. Hsu, Y.-C. Cheng, and G.-D. J. Su, "Thin autofocus camera module by a large-stroke micromachined deformable mirror," Opt. Express, vol. 18, pp. 11097-11104, 2010.

Conference Papers:

1. **H.-C. Wei**, C.-H. Liu, and G.-D. J. Su, "Fabrication of Transparent and Self-Assembled Microlens Array using Hydrophilic Effect by UV/ozone Modification," presented at the International Photonics Conference (IPC2011), Tainan, Taiwan, 2011.
2. C.-H. Liu, **H.-C. Wei**, and G.-D. J. Su, "Application of Ionic-Polymer-Metallic Composite in Flexible Antenna," presented at the International Photonics Conference (IPC2011), Tainan, Taiwan, 2011.

3. W. Cheng, F.-D. Wang, **H.-C. Wei**, and G.-D. J. Su, "The Fabrication of Deformable Mirror by Patterned Ionic-Polymer-Metal Composite," presented at the International Photonics Conference (IPC2011), Tainan, Taiwan, 2011.
4. **H.-C. Wei** and G.-D. J. Su, "Self-assembled microlens on light emitting diodes using hydrophilic effect," in *Proc. SPIE, Eleventh International Conference on Solid State Lighting*, Sandiego, USA, 2011, p. 81231N.
5. **H.-C. Wei** and G.-D. J. Su, "A Large-Stroke Deformable Mirror by Gear Shaped IPMC Design," presented at the The 6th Annual IEEE International Conference on Nano/Micro Engineered and Molecular Systems, Kaohsiung, Taiwan, 2011.
6. V. Lin, **H.-C. Wei**, and G.-D. J. Su, "Shack-Hartmann wavefront sensor with high sensitivity by using long focal length microlens array," in *Proc. SPIE, Unconventional Imaging, Wavefront Sensing, and Adaptive Coded Aperture Imaging and Non-Imaging Sensor Systems*, Sandiego, USA, 2011, p. 81650V.
7. **H.-C. Wei** and G.-D. J. Su, "A low voltage deformable mirror using ionic-polymer metal composite," in *Proc. SPIE, Polymer Optics Design, Fabrication, and Materials*, Sandiego, USA, 2010, p. 77880C.
8. Y.-W. Wang, Y.-C. Lee, M.-H. Lin, **H.-C. Wei**, W.-Y. Hsu, Y.-C. Cheng, and G.-D. J. Su, "A miniature projecting system for portable devices," in *Proc. SPIE, Novel Optical Systems Design and Optimization XIII*, Sandiego, USA, 2010, p. 77870M.
9. **H.-C. Wei** and G.-D. J. Su, "Nafion actuator simulations," presented at the 2010 14th nano, Kaohsiung, 2010.
10. **H.-C. Wei** and G.-D. J. Su, "A Low Voltage Deformable Mirror Using Gear Shaped Ionic Polymer-Metal Composite," presented at the 2010 International Conference on Optics and Photonics in Taiwan, Tainan, Taiwan, 2010.
11. **H.-C. Wei**, M.-H. Lin, Y.-W. Wang, H.-T. Hsieh, W.-Y. Hsu, Y.-C. Cheng, and G.-D. J. Su, "A Compact Auto-focus Imaging System using MEMS Deformable Mirror," presented at the 2009 Optics and Photonics Taiwan (OPT), Taipei, Taiwan, 2009.
12. Y.-W. Wang, Y.-C. Lee, M.-H. Lin, **H.-C. Wei**, W.-Y. Hsu, Y.-C. Cheng, and G.-D. J. Su, "A Miniature Projector for Portable Device Applications," presented at the 2009 Optics and Photonics Taiwan (OPT), Taipei, Taiwan, 2009.

13. H.-T. Hsieh, P.-Y. Lin, M. H. Lin, **H. C. Wei**, Y. W. Wang, W.-Y. Hsu, and G.-D. J. Su, "Design and fabrication of MEMS Deformable Mirror in Compact Auto-Focus Imaging Systems," presented at the 2009 Optics and Photonics Taiwan (OPT), Taipei, Taiwan, 2009.

Awards:

1. IPC 2011 Student Paper Award (2011 年 IPC 學生論文獎得獎)

   Oral
   E-TH-V 1-2
   Fabrication of Transparent and Self-Assembled Microlens Array using Hydrophilic Effect by UV/ozone Modification
   Hsiang-Chun Wei, Chin-Heng Liu, and Guo-Dung J. Su / National Taiwan University, Taiwan

2. OPT 2009 Student Paper Award (2009 年 OPT 學生論文獎得獎)

   Oral
   EO108
   A Compact Auto-focus Imaging System using MEMS Deformable Mirror
   H.-C. Wei, M.-H. Lin, Y.-W. Wang, H.-T. Hsieh, W.-Y. Hsu, Y.-C. Cheng, and G.-D. J. Su / National Taiwan University, Taiwan